ALTERNATING-CURRENT THIN-FILM ELECTROLUMINESCENCE

By

JOHN SOUTH LEWIS III

A DISSERTATION PRESENTED TO THE GRADUATE SCHOOL
OF THE UNIVERSITY OF FLORIDA IN PARTIAL FULFILLMENT
OF THE REQUIREMENTS FOR THE DEGREE OF
DOCTOR OF PHILOSOPHY

UNIVERSITY OF FLORIDA

2000

ACKNOWLEDGMENTS

Trying to thank all of the people who have helped me both personally and with this work is really impossible. However there are a few people to whom I owe a tremendous amount of gratitude.

Much of what I have learned the last four years, not just academically but as a person, I owe to Dr. Holloway and I thank him for it. His degree of dedication to his work and his students, and his knowledge of science and people is truly unique. I am lucky to have had him as a mentor.

Of course special thanks also goes to Ludie. The show just wouldn't go on without her. I have seen a lot of people come and go through the Holloway group. I especially thank Dr. Mark Davidson. He has taught me more things that have nothing to do with materials science than anyone, and was always willing to answer my stupid questions and talk about my stupid ideas. I also thank Philip Rack, who taught me the ropes and got me started as a grad student. There are so many others that were a pleasure to work with. Caroline, Billie, Loren, Joe, Dave… the list really doesn't seem to end, but I thank all of them.

I would have never made it to graduate school without the group at Georgia Tech, especially Dr. Jack Lackey and Dr. Tom Moss. They helped me to realize that I not only enjoy working on this stuff, but that it's important to enjoy not working on this stuff, too.

And speaking of not working, there are a lot of people to whom I probably owe not graduating a lot sooner and I thank them for it. Especially Jamie, Rich, Wayne, Mike, Brent… again there seems to be no end to this list, and I hope I can stay in touch with them.

Of course I owe my happiness and sanity the last year and a half to Ellen Robertson. I hope this is just the beginning.

Finally and most importantly, I thank Mom, Dad, Anne, and Ellen. I love them and owe them more than they know. There is nobody I can thank (or blame) more for making me the person that I am. I couldn't pick a better family.

TABLE OF CONTENTS

page

ACKNOWLEDGMENTS ii

LIST OF TABLES viii

LIST OF FIGURES ix

ABSTRACT xiv

CHAPTERS

1 INTRODUCTION 1

2 LITERATURE REVIEW 3

- 2.1 Introduction 3
- 2.2 History of Electronic Displays 4
- 2.3 History of EL Technology 6
- 2.4 EL Device Structures 8
  - 2.4.1 Test and Monochrome Structures 8
  - 2.4.2 Multi-Color and Full-Color Structures 12
- 2.5 Optical and Electrical Characteristics of ACTFEL Devices 14
  - 2.5.1 Optical Performance 14
    - 2.5.1.1 Brightness and efficiency 14
    - 2.5.1.2 Chromaticity 17
  - 2.5.2 Electrical Behavior–Ideal Circuit Model 19
- 2.6 Device Physics 23
  - 2.6.1 Tunnel Injection of Electrons 24
  - 2.6.2 Charge Transport 27
  - 2.6.3 Impact excitation and ionization 29
  - 2.6.4 Radiative decay 31
  - 2.6.5 Optical outcoupling 33
- 2.7 ACTFEL Materials 34
  - 2.7.1 Substrates 34
  - 2.7.2 Transparent Electrodes 35
  - 2.7.3 Opaque Electrodes 36
  - 2.7.4 Insulators 37
  - 2.7.5 Phosphor Layer 39
    - 2.7.5.1 Host material 40

        2.7.5.2 Luminescent centers 42
        2.7.5.3 Host-center systems 44
- 2.8 Electrical and Optical Device Characterization 45
- 2.9 ZnS:Mn as an ACTFEL Phosphor 57
    - 2.9.1 Physical Properties 57
    - 2.9.2 Optical Properties 59
    - 2.9.3 Electrical Properties 60
    - 2.9.4 Point Defects in ZnS 61
        - 2.9.4.1 Intrinsic point defects 61
        - 2.9.4.2 Extrinsic point defects 63
    - 2.9.5 Alkali Halide Doping of ZnS:Mn ACTFEL Devices 64
- 2.10 Oxide Phosphors for ACTFEL Displays 66
    - 2.10.1 General Considerations 66
    - 2.10.2 Oxide Phosphors in ACTFEL Devices 68
    - 2.10.3 Zn_2GeO_4:Mn ACTFEL Devices 69

3 ALKALI HALIDE CO-DOPING OF ACTFEL DEVICES 72

- 3.1 Introduction 72
- 3.2 Experimental Procedure 72
    - 3.2.1 Substrates 74
    - 3.2.2 Phosphor Layer Processing 74
    - 3.2.3 Device Fabrication 76
    - 3.2.4 Measuring EL Performance 76
    - 3.2.5 Electrical and Optical Characterization 77
- 3.3 Results 78
    - 3.3.1 EL Performance 78
    - 3.3.2 Optical Properties 83
    - 3.3.3 Electrical Measurements 88
    - 3.3.4 Aging Measurements 98
- 3.4 Discussion 98
    - 3.4.1 Effects of Conduction Charge on Device Performance 100
    - 3.4.2 ACTFEL Device Efficiency 102
        - 3.4.2.1 Outcoupling efficiency 103
        - 3.4.2.2 Radiative efficiency 104
        - 3.4.2.3 Excitation efficiency 107
    - 3.4.3 Modified Interface Microstructure 110
    - 3.4.4 Space Charge Effects 111
        - 3.4.4.1 Definitions and characterization 112
        - 3.4.4.2 Origin and modeling of space charge 115
    - 3.4.5 The Role of KCl in ZnS 117
        - 3.4.5.1 Point Defect Structure 117
        - 3.4.5.2 Effect of KCl doping on space charge and excitation efficiency.. 120
        - 3.4.5.3 Effects of KCl on conduction charge 124

4 Zn_2GeO_4:Mn ACTFEL DEVICES 127

4.1 Introduction 127
4.2 Experimental Procedure 128
4.2.1 Substrate Preparation 128
4.2.2 Sputter Target Preparation 130
4.2.3 Device Fabrication 131
4.2.3.1 Planar samples 131
4.2.3.2 University of Florida samples 132
4.2.4 Device Characterization 133
4.2.4.1 Microstructural and chemical characterization 133
4.2.4.2 Optical characterization 133
4.3 Results 135
4.3.1 Planar Samples 135
4.3.1.1 Device properties 135
4.3.1.2 Parameter study 135
4.3.2 UF Experiments 141
4.3.2.1 Target preparation 141
4.3.2.2 Sputtered Zn_2GeO_4 microstructural and chemical 142
4.3.2.3 Optical characterization 146
4.3.2.4 Electroluminescence behavior 148
4.3.2.5 Transient electrical measurements 150
4.3.2.6 Transient optical measurements 162
4.4 Discussion 172
4.4.1 Planar Parameter Study 172
4.4.2 UF Study 173
4.4.2.1 Structural, morphological, and chemical analysis 173
4.4.2.2 Optical characterization 176
4.4.2.3 Electroluminescence characterization 177
4.4.3 Electroluminescent Behavior of Zn_2GeO_4:Mn Devices 177
4.4.3.1 Electrical behavior 178
4.4.3.2 Optical behavior 182
4.4.3.3 Device process model 186

5 CONCLUSIONS 194

5.1 Co-Doping of ZnS:Mn with K and Cl 194
5.2 Zn_2GeO_4:Mn devices 195

6 FUTURE WORK 196

6.1 Co-Doping of ZnS:Mn with K and Cl 196
6.2 Zn_2GeO_4:Mn devices 197

LIST OF REFERENCES 200

APPENDIX A EFFECTS OF VARIOUS ALKALI HALIDES ON 210

APPENDIX B EL PERFORMANCE DATA FOR Zn_2GeO_4:Mn DEVICES................212

BIOGRAPHICAL SKETCH 217

LIST OF TABLES

Table Page

2-1. Major milestones in the development of color EL displays. 8

2-2. Fraction of electrons beyond 2.12 eV in ZnS at 300K for F=1 or 2 MV/cm. 29

2-3. List of insulators used in ACTFEL devices with values for the properties..................40

2-4. Properties of some common ACTFEL host compounds. 41

2-5. List of valence and ionic radius for cations commonly used in ACTFEL 46

2-6. ACTFEL phosphor systems and device performance. 46

2-7. Physical properties of ZnS 58

2-8. Bulk electrical properties of ZnS..61

2-9. Performance of ACTFEL devices using oxide phosphor materials. 70

3-1. Relative luminous efficiencies for KCl codoped and undoped devices 87

4-1. Range and best value of processing parameters used for the phosphor 131

4-2. Standard processing conditions used for the phosphor layer in the UF 132

4-3. Zn/Ge ratio for a range of RTA temperatures. 146

4-4. B_{40} and V_{th} values for the RTA series shown in Figure 4-16. 148

4-5. Maximum calculated phosphor field values using the measured DC 158

4-6. Gaussian fit parameters used for the curves in Figure 4-44 and 4-45. 169

A-1. Performance data for ZnS:Mn ACTFEL devices co-doped with various. 211

LIST OF FIGURES

Figure Page

2-1. Schematic diagram of (a) standard device structure, (b) inverted 11

2-2. Device structures used in full- and multi-color displays, including 13

2-3. B-V and E-V plots showing typical behavior for ZnS:Mn ACTFEL...........................16

2-4. Red (*x*), green (*y*), and blue (*z*) tristimulus curves...18

2-5. 1931 Commision de L'Eclariage chromaticity diagram...20

2-6. Equivalent circuit for an ACTFEL device showing the current..................................21

2-7. Schematic energy band diagram of the MISIM type EL structure and 24

2-8. Emission mechanisms for an electron trap..25

2-9. Schematic representation of internal reflection in a ZnS:Mn ACTFEL device. 34

2-10. Schematic diagram of circuit used to measure conduction current by 48

2-11. Schematic diagram of circuit used to measure conduction current 49

2-12. Schematic diagram of the voltage waveform used in ACTFEL.................................50

2-13. External charge-voltage (Q-V) characteristics of the ideal circuit shown...................52

2-14. Schematic diagram of the Q-V characteristics of an ACTFEL device........................52

2-15. Schematic diagram of a ZnS:Mn type Q-F_p plot. Letters refer to the 54

2-17. Schematic diagram of Q_{max}-V_{max} plot for an ideal device...57

2-18. (a) Unit cell for the zincblende structure, and (b) metal-centered 58

2-19. Simplified Tanabe-Sugano diagram for the energy levels of the $3d^5$ 60

2-20. Energy band structures for cubic ZnS, GaN, and SrS calculated using 62

2-21. Energy band diagram with deep defect levels in ZnS:Cl 65

3-1. Schematic process flow diagram for ZnS:Mn,K,Cl device fabrication....73

3-2. Brightness and efficiency vs. voltage for ZnS:Mn devices with and 79

3-3. Comparison of B_{40} brightness values for as deposited, annealed, and 79

3-4. (a) Brightness (b) and efficiency vs. voltage curves for samples from 81

3-5. (a) Brightness (b) and efficiency vs. voltage curves for different ZnS:. 82

3-6. EL emission spectra for ZnS:Mn samples with and without KCl doping. 83

3-7. PL decay curves for as-deposited, 700°C annealed, and 700°C....84

3-8. EL emission decay at 40V above threshold, 60Hz, for KCl doped and 85

3-9. EL emission decay at 40V above threshold (high drive), 60Hz, for KCl....86

3-10. EL emission decay at 40V above threshold, 60Hz, for both polarities of....87

3-11. Diffuse reflectance values for KCl doped and undoped ZnS:Mn samples....88

3-12. External charge-applied voltage (Q-V) plots for as-deposited, annealed,....90

3-13. Internal charge-phosphor field (Q_{int}-F_p) plots for as-deposited, annealed,....91

3-14. Capacitance vs. voltage curves for (a) KCl codoped and (b) undoped 93

3-15. Determination of internal charge from Q_{ext} vs. t analysis. 94

3-16. Determination of B_{max} from L(t) data. Note the necessary extrapolation....94

3-17. B_{max}/Q_{int} vs. applied voltage for both polarities of KCl codoped and 95

3-18. B_{max}/Q_{int} vs. Q_{int} for both polarities of KCl codoped and undoped. 96

3-19. Q_{max} vs. V_{max} for KCl codoped and undoped ZnS:Mn samples. 97

3-20. Q_{max} vs. V_{max} for an evaporated ZnS:Mn device 97

3-21. Brightness vs. voltage curves after 10 hour aging intervals for (a)....99

3-22. ACTFEL device equivalent circuit used for state-space analysis 116

3-23. Schematic diagram showing the point defect and charge....119

3-24. Schematic diagram showing two possible incorporation sites and 120

3-25. Schematic band diagrams showing the effect of positive space 124

4-1. Process flow diagram for the preparation of Zn_2GeO_4:Mn ACTFEL devices. 129

4-2. B-V and E-V characteristics of a Planar Zn_2GeO_4:Mn sample. 136

4-3. B_{40} versus phosphor thickness. The values are approximately linear up to. 137

4-4. B_{40} versus O_2 partial pressure for samples (a) without and (b) with tin added. 138

4-5. B_{40} and E_{40} versus applied RF sputter power for both no-tin and tin added. 139

4-6. B_{40} and E_{40} at two different sputter pressures 140

4-7. B_{40} and E_{40} values for various substrate temperatures during phosphor 141

4-8. B_{40} values as a function of RTA temperature. All RTA conditions were for 142

4-9. X-ray diffraction spectra for unfired target powder and Zn_2GeO_4:Mn, ...143

4-10. PL spectrum from Zn_2GeO_4:Mn target excited by a handheld UV lamp. 143

4-11. X-ray diffraction spectra for Zn_2GeO_4:Mn thin films annealed at a 144

4-12. Variation of FWHM of the (006) diffraction peak with RTA temperature. 144

4-13. SEM micrographs of the surface morphology of samples annealed at 145

4-14. PL (dashed line) and PLE (solid line) spectra for a Zn_2GeO_4:Mn thin 147

4-15. PLE spectrum for Zn_2GeO_4:Mn plotted as excitation^2 versus energy 147

4-16. Brightness-voltage (B-V) curves for Zn_2GeO_4:Mn samples annealed at a 149

4-17. EL emission spectrum from a Zn_2GeO_4:Mn sample. 149

4-18. Q-V data for the fresh 200 nm Zn_2GeO_4:Mn device at various applied 151

4-19. Q-V data for the 200 nm Zn_2GeO_4:Mn device at various applied 151

4-20. Q-V data for the fresh 480 nm Zn_2GeO_4:Mn device at various applied 152

4-21. Q-V data for the 480 nm Zn_2GeO_4:Mn device at various applied 152

4-22. Q-V data for the fresh 700 nm Zn_2GeO_4:Mn device at various applied 153

4-23. Q-V data for the 700 nm Zn_2GeO_4:Mn device at various applied 153

4-24. Q-F_p data for the fresh 480 nm sample using the measured DC 155

4-25. Q-F_p data for the fresh 200 nm sample using the idealized capacitance 155

4-26. Q-F_p data for the 200 nm sample using the idealized capacitance 156

4-27. Q-F_p data for the fresh 480 nm sample using the idealized capacitance 156

4-28. Q-F_p data for the 480 nm sample using the idealized capacitance 157

4-29. Q-F_p data for the fresh 700 nm sample using the idealized capacitance 157

4-30. Q-F_p data for the 700 nm sample using the idealized capacitance 158

4-31. Q-F_p data for fresh samples with different phosphor layer thickness..........................159

4-32. Q-F_p data for aged samples with different phosphor layer thickness. 160

4-33. Comparison of the fresh and aged Q-F_p behavior for the 200 nm sample. 160

4-34. Comparison of the fresh and aged Q-F_p behavior for the 480 nm sample. 161

4-35. Comparison of the fresh and aged Q-F_p behavior for the 700 nm sample. 161

4-36. EL decay behavior at various wavelengths for the Al(+) polarity. 162

4-37. EL decay behavior at various wavelengths for the Al(-) polarity. 163

4-38. EL emission spectrum measured 6 μs after the Al(+) voltage pulse is 164

4-39. EL emission spectrum measured 6 μs after the Al(-) voltage pulse is 164

4-40. EL decay behavior for 390 nm emission for each polarity relative.............................165

4-41. Normalized EL emission spectra for the Al(+) polarity measured.............................167

4-42. EL emission spectra for the Al(+) voltage pulse measured 10, 40,.............................167

4-43. EL emission spectra for the Al(-) voltage pulse measured 10, 40,...............................168

4-44. EL emission spectra for the Al(+) voltage pulse measured 40 and. 168

4-45. EL emission spectra for the Al(+) voltage pulse measured 40 and. 169

4-46. 540 nm EL emission from the fresh 700 nm sample and the applied 170

4-47. 520 nm EL emission, conduction current, and applied voltage vs. time.....................171

4-48. 520 nm EL emission, conduction current, and applied voltage vs. time.....................171

4-49. Schematic energy band diagram showing the smaller average 188

4-50. Schematic diagram showing EL processes for the Al(-) polarity in............................189

4-51. Schematic diagram showing the EL processes which occur during............................191

A-1. B-V data for ZnS:Mn ACTFEL devices co-doped with various alkali........................210

Abstract of Dissertation Presented to the Graduate School
of the University of Florida in Partial Fulfillment of the
Requirements for the Degree of Doctor of Philosophy

ALTERNATING-CURRENT THIN-FILM ELECTROLUMINESCENCE

By

John South Lewis III

December, 2000

Chairman: Dr. Paul H. Holloway
Major Department: Materials Science and Engineering

Alternating-current thin-film electroluminescent (ACTFEL) phosphors have been studied and improved with respect to brightness, color and efficiency. It is shown that ex-situ co-doping of the sputter deposited ZnS:Mn active layer with K and Cl results in 53% improvement in brightness, 62 % improvement in efficiency, and better 100-hour accelerated aging stability. This improvement was demonstrated to result from a 75% increase in excitation efficiency for conduction electrons, combined with a small decrease in both light outcoupling and non-radiative recombination. By studying the electrical behavior of the co-doped devices as compared to the undoped devices, it was determined that there is a reduced amount of static space charge in the films, resulting in a larger average field, increased excitation efficiency, and increased charge multiplication. The reduced space charge is attributed to the addition of charge compensating zinc vacancy-chlorine complexes and isolated chlorine point defects, which are acceptor and donor defects, respectively, and the reduction of zinc vacancy deep hole traps. It is postulated that there is sufficient electron multiplication or donor ionization to create a situation in which the current limit is set by the phosphor resistance rather than a capacitance or density of states.

Thin film Zn_2GeO_4:Mn phosphor layers were evaluated as green-emitting ACTFEL devices. Devices with Zn_2GeO_4:Mn magnetron sputter deposited films exhibited brightness and efficiency values of 74 cd/m^2 and 0.19 lm/W, respectively at 40 V above threshold and 60 Hz. Poor outcoupling efficiency suggests an internal efficiency that is much higher. Optical spectroscopy reveals efficient charge transfer from the lattice and a 615 meV sub-band gap defect state to the Mn^{2+} ion. Unique transient optical and electrical behavior under EL excitation is observed. A phenomenological model is presented to explain the behavior. The unique aspects of the model include a resistance-capacitance limit on charge injection, efficient charge injection for only one polarity, abnormally large space charge density for one polarity that allows efficient electron-hole pair recombination in low electric field regions, and near-resonant energy transfer to and from the Mn^{2+} excited state.

CHAPTER 1
INTRODUCTION

Emissive flat panel technologies have long been sought after, initially for the purposes of distributed lighting and "TV-on-a-wall" applications. While neither of these applications has been realized to an appreciable extent, the flat panel display industry now accounts for 45% of the total display market. This percentage is expected to increase to 63% of a >$100 billion market by the year 2005 [1]. Enabling technologies such as portable electronics and communications have made flat panels pervasive in the everyday lives of people in developed nations. For many people the thought of flat panel displays brings to mind the notebook computer, which is a market dominated by the liquid crystal display, but for comparison this market is projected to be ~$10 billion by the year 2002 [2]. It is clear that there are numerous markets that could allow competition from developing flat panel technologies.

The alternating-current thin-film electroluminescent (ACTFEL) display has found niche market applications which rely on the thermal and mechanical robustness of the displays, as well as their wide viewing angle and excellent contrast ratio. The power consumption of these displays is higher than desired for portable electronics. However the single largest limitation for the technology is the lack of a full-color, red-green-blue (RGB) product. Recent developments in blue-emitting ACTFEL phosphors have brought the technology closer than ever to overcoming this limitation. However there is still a need for improved performance in terms of both efficiency and stability for the red- and green-emitting components.

Chapter 2 will present a background of ACTFEL devices as well as a general overview of the current understanding of their operation. In Chapter 3, results will be presented which show a dramatic improvement in the performance of planar RF magnetron sputter deposited ZnS:Mn ACTFEL devices by ex-situ doping with KCl. Evidence will be presented in this chapter which shows that this improvement results from a modified space charge distribution in the phosphor layer which leads to improved excitation efficiency. In Chapter 4 an investigation into the potential of green-emitting Zn_2GeO_4:Mn as the active layer in ACTFEL devices. Zn_2GeO_4:Mn will be shown to exhibit poorer performance than the best green-emitting phosphors, but research suggested in future work could dramatically improve such devices. In addition, some insight is given to the unique electro-optic properties of Zn_2GeO_4:Mn based devices. In chapter 5 conclusions will be presented and in Chapter 6 suggestions for future work will be discussed.

CHAPTER 2
LITERATURE REVIEW

2.1 Introduction

Electroluminescence is by definition, the nonthermal generation of light resulting from the application of an electric field to a substance [3], usually a semiconductor. There are two predominant and distinct methods by which this is achieved, both of which are technologically important and both of which are referred to as electroluminescence. One involves the excitation of a luminescent center by ballistic electrons transported through an inorganic host. Following the practice of the display community [4], this is the process referred to as electroluminescence throughout this dissertation. The other involves forward biasing of a p-n junction resulting in recombination of electron-hole pairs, or the excitation of a luminescent center by energy transfer from an electron-hole pair recombination. This technique is used in both inorganic semiconductor-based light-emitting diodes (LED's) and diode lasers, as well as organic devices known as either organic LED's (OLED's) or as organic electroluminescence (OEL). These devices are not discussed in this dissertation.

A brief discussion of the historical development of electronic displays is given as well as an overview of flat-panel display technology. An introduction to the development of electroluminescence (EL) technology and alternating-current thin film EL (ACTFEL) devices also is given. This is followed by a review of the device structures used for EL devices and the physical processes involved in their operation. The materials selection criteria and critical processing issues also are covered. The electrical and optical techniques used to characterize ACTFEL devices are discussed. A background on the current understanding of ZnS-based devices is presented, and the use of co-dopants (those other than the activator dopant) to enhance device performance will be discussed. Finally a review of the use of oxide-based phosphors is given.

While a review is given here of electroluminescent materials and processes, several excellent reviews of electroluminescent technology are also available, and the reader is referred to them as well [3-5].

2.2 History of Electronic Displays

A display is "an electronic component or subsystem used to convert electrical signals into visual imagery in real time suitable for direct interpretation by a human observer" [4]. The fundamental technologies involved in displays date back as far as the 17th century, when Casciorolo of Bologna, Italy observed the first phosphor, or luminescent solid, in 1603, and gas discharge emission was observed by Jean Picard in Paris, France in 1675. In 1869 John William Hittorf in Munster, Germany first observed cathode-based emission from the wall of a glow lamp, and the first observable cathode ray was seen in the "Crookes Tube" by Sir William Crookes in London, some time between 1875 and 1879 [4, 6].

The use of electronic displays for information content began with the development of the cathode-ray tube (CRT). The invention of the CRT itself is attributed to Karl Ferdinand Braun, as early as 1896 or 1897 [4, 6]. The "Braun tube" used both deflection of the electron beam and excitation of a phosphor screen. This is thought to be the first application of a device for display purposes, since Braun used the tube to monitor the output of an electrical generator. Although the first demonstration of a working television took place in 1927 by Philo T. Farnsworth, the development of the CRT and its application to display was a rather slow process. A good review of the development of the CRT is given by Lyons [7]. The market pull for developing the manufacturing technology needed for widespread application of the CRT was radar, initially used primarily for military applications in World War II. It was not until the 1950s and 60s that mass production techniques were developed for the color CRT [4]. Since that time the CRT has become the leading display technology both economically and in terms of image quality. The CRT dominates the display market because of its cost and familiarity, and its performance excels because of the simplicity of scanning and good chromaticity, resolution, brightness, and contrast. However the CRT suffers from its requirement for high voltages, poor power efficiency, and is inherently restricted by size and weight factors [8]. For the purpose of strength, large CRTs must use a thick glass tube making the scaling of CRTs beyond ~35" very difficult. In addition there is an inherent depth to the CRT due to the required scanning of the high energy electron beam (or a cluster of three beams) across the phosphor screen.

The widespread use of the CRT for the display of images as well as the advent of portable electronics led to interest in the development of flat-panel displays. There are a number of economically important flat panel display technologies, and several others still under development. Among these are the liquid crystal display (LCD), the plasma display panel (PDP), the inorganic light-emitting diode (LED), the organic LED (OLED) also known as organic electroluminescent (OEL) display, the field-emission display

(FED), the laser diode-based display (LD), and the electroluminescent (EL) display. The operation of all but the EL displays are not covered here, and the reader is referred to several other publications that discuss them [4, 6, 8, 9].

Since research into flat panel technologies began, a primary objective for much of the display community has been the development of a "TV-on-a-wall." Today billions of dollars of annual revenue are generated by systems using flat panel technologies, and yet the wall-hanging TV remains elusive. Two of the technologies, PDPs and LCDs are just reaching the market as mass produced products for this application, though it is clear that neither currently meets the demanding economic and performance requirements for this application, leaving the market open to still-developing technologies.

2.3 History of EL Technology

The first reports of electroluminescence are often attributed to a well known paper by Destriau in 1936. However the first observations of the effect of electric fields on luminescence were reported by Gudden and Pohl in 1920 [10]. They discovered that when a ZnS:Cu phoshor is insulated from the electrodes, an applied electric field of several kV/cm that is either constant or alternating temporarily increases the luminescent intensity. Soon after that, electroluminescence was first reported by Lossev in 1923, who observed luminescence from near the electrodes on a silicon carbide crystal detector [11]. The first observation of electroluminescence using a device that resembles modern powder EL cells was reported by Destriau in 1936. He observed light emission when an electric field on the order of 30 kV/cm is applied to a suspension of ZnS:Cu particles in oil [12-14]. Because of delays caused by World War II, skepticism about the pure electroluminescent nature of his results remained as late as 1950 [4]. Heinisch gives a good review of this early work on electroluminescence [15].

Interest in the phenomenon remained low until the 1950s when GTE Sylvania received a patent for an EL powder lamp. At this time the devices were limited to powder phosphors embedded in a dielectric matrix. Improved EL efficiencies achieved in the 1950s and 1960s created much enthusiasm over the potential to reach and even improve on the 15 lm/W efficiency of the incandescent bulb. However these early devices were plagued by low light output and short operating lifetime, in addition to the high voltage control circuitry and a rapid deterioration when operated above room temperature [16]. Even though AC powder EL instrument panels were used in seven different functions on Apollo and LM vehicles for NASA [4], most research in the field stopped by the late 1960s [6, 16]. However progress was made during this time in thin film devices. In 1961, Soxman et al. successfully used a ZnS:Mn phosphor with a dielectric to demonstrate AC thin film electroluminescence. They produced test panels that achieved 1700 cd/m^2 at 5 kHz, were the first to show that a black matrix behind the phosphor layer could produce a sunlight readable display with a brightness of just 85 cd/m^2, and demonstrated lifetimes of several thousand hours [4]. Interest was renewed in EL information displays with the ground-breaking presentation of high brightness, stable electroluminescence in a matrix-addressed display using improved dielectrics with ZnS:Mn phosphor by researchers from Sharp in 1974 [17, 18]. In 1980 Tektronix built a prototype computer display based on this phosphor, and the display portion of the company later became Planar Systems, Inc [19]. In 1983 Sharp began industrial production of monochrome amber panels, and was followed by production at Planar Systems one year later [16].

Since the entry to commercial markets, interest has been maintained in the research of thin film EL phosphors. The primary objectives were to understand the device physics and processes; to improve device brightness, stability, and efficiency; and to develop primary red-, green-, and blue-emitting phosphors for full-color displays. A summary of progress in color phosphors since the commercialization of EL displays is shown in Table 2-1.

Table 2-1. Major milestones in the development of color EL displays[3].

1981	Color thin-film EL devices based on rare-earth doped ZnS(Okamoto)
1984	Blue emission from SrS:Ce thin-film EL device (Barrow *et al.*)
1985	Multicolor emission from CaS and SrS based thin-film EL (Tanaka *et al.*)
1986	Luminance improvement of SrS:Ce (Tanaka *et al.*)
1986	Prototype multicolor thin-film EL display (Barrow *et al.*)
1987	Luminance improvement of ZnS:Tb,F by sputtering (Ohnishi *et al.*)
1988	White emission from SrS:Ce,Eu (Tanaka *et al.*)
1988	Prototype full-color thin-film EL display (Barrow *et al.*)
1991	Multicolor thin-film EL display using an inverted, patterned-color-filter device structure based on ZnS:Mn (Okibayashi *et al.*)
1992	Red/Green/Yellow multicolor EL display in the an inverted, patterned-color-filter device structure with ZnS:Mn phosphor (Haaranen *et al.*)
1993	First commercial multicolor (Red/Green/Yellow) thin-film EL display panel in EGA format (Cramer *et al.*)
1993	Bright blue emission from $CaGa_2S_4$:Ce and prototype full-color thin-film EL display (Barrow *et al.*)
1994	First commercial full-color thin-film EL display monitor (Barrow *et al.*)

2.4 EL Device Structures

2.4.1 Test and Monochrome Structures

There are several frequently used device structures in ACTFEL technology. However the most common structures have several important characteristics in common.

First, there is a thin film phosphor layer sandwiched between two electrodes capable of providing a high electric field across the phosphor layer. Second, there is one (or two) insulating, or dielectric, layer(s) that prevent DC current from flowing through the device. Thus the EL stack is primarily capacitive in nature. And third, at least one of the two electrodes is transparent to allow light to escape the device in the direction of the viewer. (This last condition is not true for specialized edge-emitting devices, which are not intended for display applications [3].)

The most common structure used for ACTFEL devices is known as the "standard," MISIM (metal-insulator-semiconductor-insulator-metal), or "full stack" structure, shown schematically in Figure 2-1a. This device uses a transparent substrate, normally glass, and a transparent bottom electrode that is deposited onto the glass. This is followed by deposition of a transparent insulator, the phosphor layer, a second insulating insulator, and finally an opaque electrode. Light is transmitted through the glass in the direction of the viewer. The rear electrode can be made reflective to increase the brightness of the device, and a dark layer can be used behind the phosphor to enhance contrast. This type of structure has several advantages. It allows the use of glass substrates, which are inexpensive and widely available in any size. It also allows for "self-healing" of pinhole defects when aluminum is used with a proper top insulator. "Self healing" means that when microscopic shorts occur in the phosphor they do not propagate and lead to a catastrophic breakdown. Instead, the breakdown failure is limited to a very localized region due to the rapid fusing of the aluminum electrode film by the sudden current flow to a short circuit.

Another common type of device structure is known as the “inverted” structure, because in this case the substrate is normally (but not necessarily) opaque and the top insulator transparent [3]. The light leaves the top of the device toward the viewer. There are two variations on such a structure. In one case (Figure 2-1b) the substrate acts as both the support structure and the dielectric layer [20]. In this case the substrate is normally a high dielectric constant material such as $BaTiO_3$. Sometimes a thin-film dielectric is deposited on top of the substrate for planarization before deposition of the phosphor layer. The bottom electrode is deposited on the opposite side of the substrate as the phosphor, and thus the substrate is part of the device. In the second case, shown in Figure 2-1c, the bottom electrode is deposited on top of the substrate, followed by a thick or thin film dielectric and then the phosphor layer [21].

The inverted structure has several advantages relative to the standard structure shown in Figure 2-1a. Without the requirement for a transparent substrate, a substrate material such as a ceramic may be chosen that allows higher temperature processing than does a glass substrate. This is often beneficial in optimizing the microstructure and subsequent performance of the phosphor layer. Another benefit of the inverted structure involves full- or multi-color display applications when filters are used. Simple organic filters may be added after any high temperature processing steps, as opposed to the standard structure which requires that the filters be deposited before the phosphor layer. One of the drawbacks of the inverted structure is the loss of the self-healing failure mechanism exhibited by Al contacts, since a transparent conductor must be used as the top electrode rather than a metal.

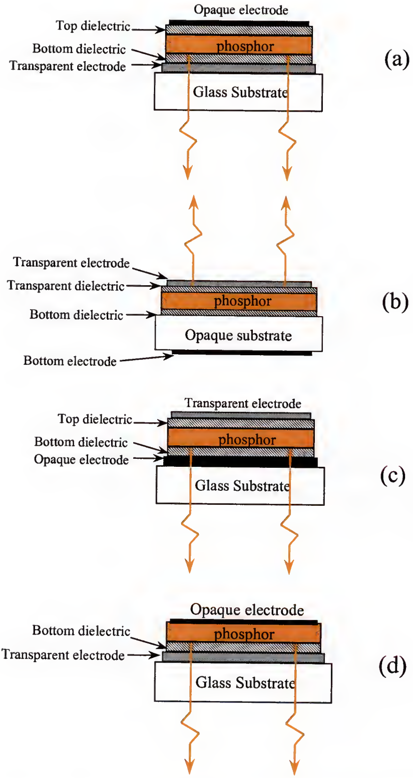

Figure 2-1. Schematic diagram of (a) standard device structure, (b) inverted structure – dielectric substrate, (c) inverted structure – thin film dielectric, and (d) half-cell structure.

The final type of device, shown in Figure 2-1d, is normally used only for device testing. This device is known as the "one insulator" or "half stack" structure. This type of device can be similar to either the standard or the inverted structure, but lacks one of the two insulating layers. Normally it lacks the top insulator, which saves an additional processing step. This type of structure has the advantage of ease of processing and therefore more rapid results. However it normally has poorer performance in terms of brightness and stability than the dual insulating structures, and is primarily used for research purposes.

2.4.2 Multi-Color and Full-Color Structures

The ultimate goal for video display is full color and grayscale capabilities. There are four main approaches to the development of full color EL displays [3]. These are

1. Stacked-phosphor structure (Figure 2-2a)
2. Patterned-phosphor structure (Figure 2-2b)
3. "Color-by-white" filtered structure (Figure 2-2c)
4. Dual-substrate structure

A comprehensive discussion of these structures and list of references is given by Ono [3].

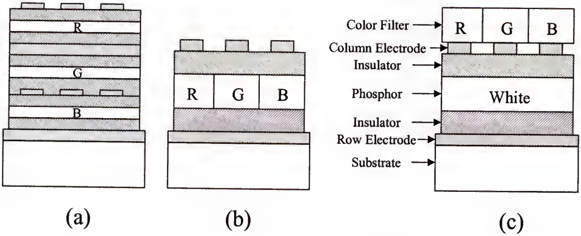

Figure 2-2. Device structures used in full- and multi-color displays, including the (a) stacked-phosphor structure, (b) patterned-phosphor structure, and (c) broad band phosphor with color filters, or "color by white" [3].

The first of these to be investigated was the stacked-phosphor structure. This type of device has the advantage of high resolution, because there is no spatial separation of the three subpixels. In addition, the only lithographic processes required are similar to the electrode patterning steps required for monochrome devices. The primary disadvantages are the loss of self-healing breakdown due to the use of the intermediate ITO electrode and the added processing steps.

The patterned phosphor approach has the advantages of a simpler drive structure, being identical to that of a monochrome panel, and the use of aluminum electrodes for self-healing breakdown. The primary disadvantages are more complicated processing because of the required masking and etching steps, and a lower areal luminance due to the reduced fill factor.

The color-by-white approach uses a broad band phosphor that can be filtered to obtain red, green, and blue pixels. This approach has the advantages of simple processing as only one phosphor layer is used, and a simple drive structure. In addition, if an inverted structure is used, then inexpensive organic filters similar to those used in LCDs may be used. The primary disadvantages are the inherent loss in efficiency due to the filtering of the broad band phosphor, and the use of an ITO top electrode which eliminates the self-healing breakdown process.

The dual substrate approach uses independent substrates that have a two- and one-color device on each, which are then sealed together. This approach combines the processing simplicity of a monochrome panel and the ability to use independent threshold voltages for each substrate. In addition each half can be tested as a complete device, improving manufacturing yield. However, the display requires two complete sets of substrates and drivers, therefore increasing costs and negating the general advantage of manufacturing simplicity.

2.5 Optical and Electrical Characteristics of ACTFEL Devices

2.5.1 Optical Performance

2.5.1.1 Brightness and efficiency

An ACTFEL device is operated by applying high voltage pulses of alternating polarity. Any waveform of alternating polarity may be used, including sine waves, triangle waves, square pulses, and trapezoidal pulses, and the applied voltage is specified as the maximum voltage per pulse, rather than the RMS value [22]. Generally there is a voltage threshold above which a significant amount of light is produced. The brightness as a function of voltage is known as a B-V curve. Devices often are compared by the value of brightness at 40 V above this threshold, and this value is called the B_{40} value. Similarly, efficiency at 40 V above threshold is known as E_{40}. The data are plotted either on a linear or a semi-log scale, depending on the information of interest. Typical data from a sputter deposited ZnS:Mn device are shown in Figure 2-3. These data were collected using a 40 μs trapezoidal waveform at 60 Hz.

There are three common methods for determining the threshold voltage, and each has advantages and disadvantages versus the others. The first two are shown in Figure 2-3. One common definition for threshold voltage is that voltage at which the light output reaches a luminance of 1 cd/m^2 (Figure 2-3b). This method has the advantage of simplicity, but suffers from the fact that the luminance values are scaled according to the spectral sensitivity of the standard observer. This means that in general, green phosphors reach this threshold at a lower proportion of their normal output than do red or blue phosphors. If phosphors emitting the three primary colors are held at this threshold voltage the color balance would not be neutral (white). In addition, the variation of turn-on characteristics for different samples can mean that the large slope portion of the B-V curve could occur at varying voltages above the 1 cd/m^2 threshold. A second method involves finding the highest slope of the B-V curve, then extrapolating this slope back to the voltage axis. This has the advantage of defining the portion of the B-V curve relative to the voltage at which rapid turn-on occurs. However, very different behaviors can take place below this threshold that are not accounted for by this definition. Finally, electrical characteristics are often used to define threshold. This is done most often with Q-V and C-V curves, which are discussed in Section 2.8 [23]. The electrical turn-on often corresponds closely with the optical turn-on, but again suffers from not being able to compare devices with different turn-on characteristics adequately. This last definition of V_{th} is seldom used, and is not of as much interest for practical display applications because it is not defined by optical characteristics.

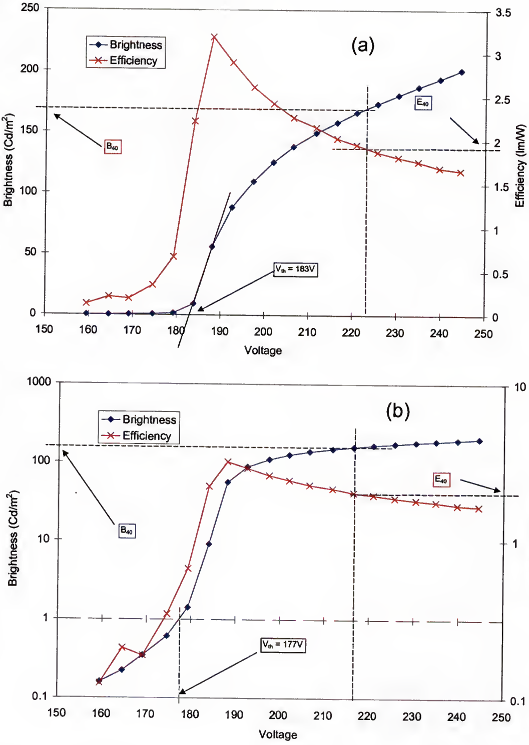

Figure 2-3. B-V and E-V plots showing typical behavior for ZnS:Mn ACTFEL devices. The same data are shown using (a) a linear scale and the extrapolation method for determining V_{th}, and (b) a log scale and the 1 cd/m^2 threshold value for determining V_{th}.

2.5.1.2 Chromaticity

Quantitative methods for evaluating chromaticity, colorimetrics, were developed that are standard to the entire display community. These methods involve relating the spectral distribution of the phosphor to values that correspond to the color seen by an observer. The most commonly used standard is that established by the 1931 Commission Internationale de l'Eclairage (CIE) which defines chromaticity using three values (x, y and z CIE coordinates) that can be plotted on a two-dimensional graph (CIE diagram, since $z = 1 - x - y$). These plots offer a convenient quantitative comparison of the color of different phosphors [9]. Under the additive mixing rule, any color can be reproduced by adding the three primary colors (tristimulus values). The 1931 CIE system uses monochromatic sources as the primary colors for blue ($\lambda = 435.8$ nm), green ($\lambda = 546.1$ nm), and red ($\lambda = 700$ nm). The R,G, and B tristimulus curves are denoted as x, y, and z, and are shown in Figure 2-4. The color is determined by calculating X,Y, and Z values such that

$$X = K_m \int_{380}^{780} \Phi_{e\lambda} x(\lambda) d\lambda$$

$$Y = K_m \int_{380}^{780} \Phi_{e\lambda} y(\lambda) d\lambda$$

$$Z = K_m \int_{380}^{780} \Phi_{e\lambda} z(\lambda) d\lambda$$

where $\Phi_{e\lambda}$ is the spectral output of the source, λ is the wavelength and $K_m = 680$ lm/W. The chromatic coordinates are found from

$$x = \frac{X}{X + Y + Z}$$

$$y = \frac{Y}{X+Y+Z}$$

$$z = \frac{Z}{X+Y+Z}$$

Because x + y + z = 1, and because the tristimulus function for $y(\lambda)$ is equal to the spectral response of the standard observer, then the colorimetric evaluation can be expressed as a brightness, Y, and two chromaticity values which are traditionally x and y.

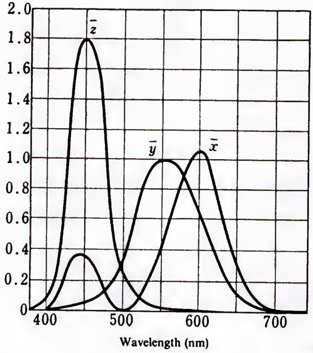

Figure 2-4. Red (*x*), green (*y*), and blue (*z*) tristimulus curves [9].

The x and y values are plotted on the CIE diagram, shown in Figure 2-5. The curved perimeter of the CIE diagram, which spans from blue to red, is defined by single wavelengths and represent completely saturated colors. Any broadening of the emission spectrum results in coordinates inside these boundaries and towards the center or "white" region of the diagram.

When two phosphors are plotted on this diagram any chromaticity on the line connecting them can be produced by a linear combination of the two phosphors. Similarly, any three phosphors may be used to produce any color contained within the area defined by the CIE coordinates of the phosphors. Therefore the fullest gamut of colors can be produced by using red, green, and blue phosphors that are as saturated as possible.

2.5.2 Electrical Behavior–Ideal Circuit Model

Interpretation of the electrical characteristics of an ACTFEL device is aided by considering an equivalent circuit model. This helps to explain the operation of the device and the roles of the various components, which are discussed later. Circuit models are discussed in more detail later, but for now a very simple equivalent circuit is used.

Below threshold, the device can be modeled accurately by considering the insulators and the phosphor layer as series capacitors. The two insulators can be combined numerically by treating them as series capacitors and can be considered as a single ideal capacitor. At a certain threshold voltage, rapid turn-on occurs where a real current flows through the phosphor layer, sometimes called the conduction or dissipative current (as opposed to the charging current which charges the capacitors and is discharged on removal of the applied voltage). In an ideal device, the dissipative current is stored until an opposing pulse is applied and the current flows in the opposite direction. Following the procedure used by Ono [3], the device can be modeled as a circuit (Figure 2-6) where the phosphor layer is modeled as a parallel capacitor and nonlinear resistor. The nonlinear resistor has the characteristics shown below the circuit in Figure 2-6. The nonlinear resistor often is modeled as a set of back-to-back Zener diodes.

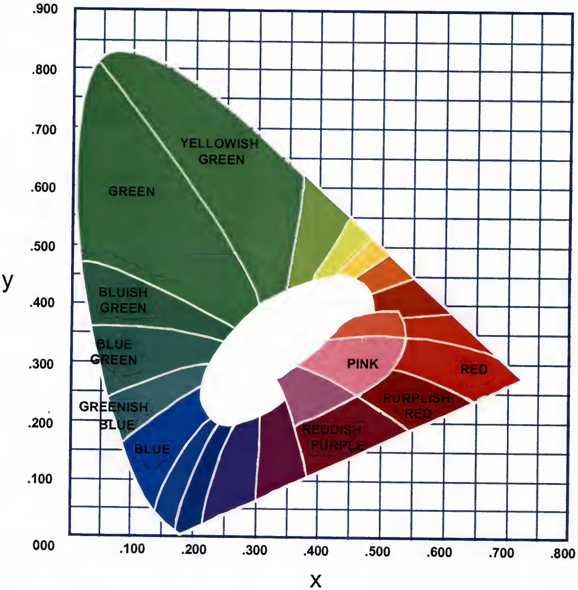

Figure 2-5. 1931 Commision de L'Eclariage chromaticity diagram.

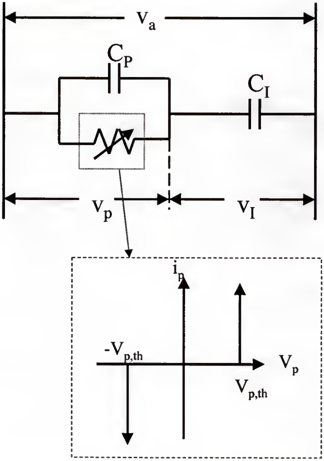

Figure 2-6. Equivalent circuit for an ACTFEL device showing the current-voltage characteristics of the non-linear resistor [3].

The derivation of the following characteristics is given in more detail by Ono [3], but results of the circuit analysis are presented here. Below threshold, the applied voltage is capacitively divided by the phosphor and the insulators giving

$$V_P = \frac{C_I}{C_I + C_P} V_a \qquad \textbf{(2-1)}$$

$$V_I = \frac{C_P}{C_I + C_P} V_a \qquad (2\text{-}2)$$

where V_a is the applied voltage and V_I and V_P are the voltages across the insulators and the phosphor layer, respectively. C_I and C_P are the insulator and phosphor capacitance, respectively.

Above threshold, the resistive portion of the phosphor circuit allows current to flow (condcution current) until the voltage across the phosphor returns to threshold. At the same time the conduction current must be balanced by capacitive current which will charge the insulating capacitors to maintain the overall voltage across the device. So the final voltages above threshold are

$$V_{P,f} = V_{P,th} = \frac{C_I}{C_I + C_P} V_{th} \qquad \textbf{(2-3)}$$

$$V_{I,f} = V_a - V_{P,f} = \frac{C_P}{C_I + C_P} V_{th} . \qquad (2\text{-}4)$$

Here the concept of field clamping is apparent. The phosphor layer in this simple equivalent circuit model is maintained at the threshold voltage regardless of the applied voltage. The amount of dissipative charge through the phosphor required to maintain the applied external voltage is

$$Q^{ext} = 2C_I (V_a - V_{th}) \qquad (2\text{-}5)$$

and the interface charge density at the end of a pulse is half this value. (The circuit model represents a perfectly symmetric device. The other half of the transferred charge neutralized the previous interface charge.) Using this value for transferred charge along with the voltage transferred from the phosphor to the insulators, the power consumption density is found to be

$$P_{in} = 4fC_I (V_a - V_{th}) V_{P,th} \qquad (2\text{-}6)$$

where f is the drive frequency.

2.6 Device Physics

A basic requirement for electroluminescence to occur is that an electric field be applied to a luminescent material with sufficient strength to generate charge carriers which can impact excite or impact ionize a luminescent center. Impact excitation and impact ionization are differentiated by the valence state of the impurity after impact [24]. Impact excitation does not change the valence of the impurity but rather rearranges the electrons to a higher energy configuration. Impact ionization of defects results from delocalization of a valence electron into a continuum state, such as the conduction band, and leaves an ionized center. This center is then free to recombine with a free electron. For example, in ZnS a Mn^{2+} ion is typically excited by direct impact, while in CaS a Eu^{2+} ion is thought to be ionized and then later brought back to its ground state after a radiative recombination with a free electron [24]. Impact ionization of the lattice can also occur resulting in generation of an electron-hole pair.

The physical processes of electroluminescence can be broken down into several steps, namely: (1) injection of electrons into the conduction band, (2) acceleration of a fraction of the electrons to ballistic energies due to the applied field, (3) impact excitation of the luminescent centers by electrons with sufficient energy, (4) radiative relaxation of the centers (in competition with non-radiative relaxation), and (5) outcoupling of the generated photons. An additional process which can occur is (3b) impact ionization of the lattice or of defects by electrons. These processes are shown in their simplest form in Figure 2-7. In the following sections, these processes will be discussed individually in more detail.

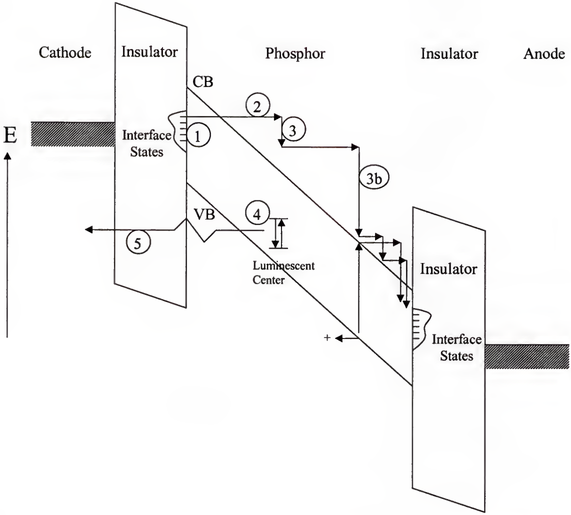

Figure 2-7. Schematic energy band diagram of the MISIM type EL structure and the mechanisms leading to electroluminescence. Numbered processes refer to those described in the text.

2.6.1 Tunnel Injection of Electrons

The source for charge carriers under steady state operation is generally accepted as being primarily from interface states for ZnS:Mn devices, even though it has been shown that a sufficient amount of native defect traps exist throughout the ZnS film to explain the conduction current [24]. The most convincing evidence for dominance by interface states comes from the significant variation in device performance depending on the type of dielectric that is used, even if the layer capacitance is not changed. The depth and concentration of available interface states has been shown to change significantly when the dielectric was changed [25]. When the local electric field at the cathode reaches a threshold level, charge injection takes place. This threshold field, however, is not necessarily the average field that is measured externally, as will be discussed later. Among the possible mechanisms responsible for injection of electrons into the conduction band are thermionic emission, pure tunneling, and phonon-assisted tunneling [26]. These mechanisms are shown in Figure 2-8. Thermionic emission occurs when the electron obtains sufficient thermal energy to surmount the potential barrier. Pure tunneling results when the potential barrier width decreases due to the electric field to the extent that efficient quantum tunneling can occur. Phonon-assisted tunneling is a combination of the two, where phonon interactions allows efficient tunneling.

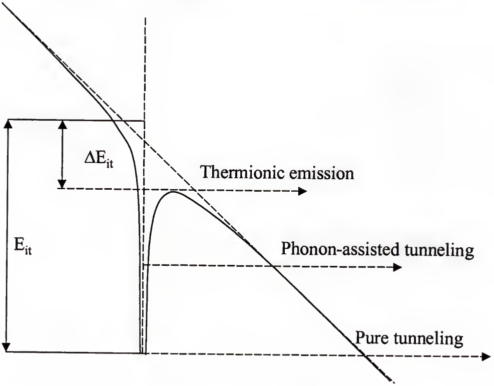

Figure 2-8. Emission mechanisms for an electron trap [26].

Analytical expressions for these mechanisms are given in the literature [26-29]. The rate of thermionic emission from a discrete state is given by the expression:

$$e_n^{thermal} = \sigma v_{th} N_c \exp\left(-\frac{E_{it} - \Delta E_{it}}{kT}\right)$$

where σ is the capture cross section, v_{th} is the thermal velocity, N_c is the conduction band density of states, k is Boltzmann's constant, T is the absolute temperature, and E_{it} is the interface trap depth. ΔE_{it} is the coulombic barrier lowering, given by:

$$\Delta E_{it} = q\sqrt{\frac{qf_p}{\pi \varepsilon_p}}$$

where q is the electronic charge, and f_p is the electric field in the phosphor. The expression for the emission rate from pure tunneling is

$$e_n^{PT} = \frac{qf_p}{4(2m^* E_{it})^{\frac{1}{2}}} \exp\left[\left(-\frac{4}{3}\frac{(2m^*)^{\frac{1}{2}} E_{it}^{\frac{3}{2}}}{q\hbar f_p}\right)\left(1-\left(\frac{\Delta E_{it}}{E_{it}}\right)^{\frac{5}{3}}\right)\right]$$

where m^* refers to the electron effective mass and $\hbar$ is Planck's constant. The emission rate due to phonon-assisted tunneling is given by:

$$e_n^{PAT} = e_n^{thermal} \int_{\frac{\Delta E_{it}}{kT}}^{\frac{E_{it}}{kT}} \exp\left[z - z^{\frac{3}{2}}\left(\frac{4}{3}\frac{(2m^*)^{\frac{1}{2}} kT^{\frac{3}{2}}}{q\hbar f_p}\right)\left(1-\left(\frac{\Delta E_{it}}{zkT}\right)^{\frac{5}{3}}\right)\right] dz .$$

For trap depths of 1.5 eV and room temperature, the dominant injection mechanism is pure tunneling [26]. It has been suggested that since the device current has a temperature dependence, the mechanism must be thermally assisted [30]. However it has been shown recently that other factors, such as the temperature dependence of the trapping efficiency of deep hole traps, can also influence device current [26].

2.6.2 Charge Transport

The characteristics of high field transport in ACTFEL devices have been the subject of considerable debate. Most of the attention has been paid to ZnS as the phosphor host material. A critical issue is the efficiency with which charge carriers are able to gain sufficient energy to impact excite the luminescent centers without loss to mechanisms such as optical phonon or intervalley scattering. To date it seems that there is no consensus that accurate results have been obtained. Band structure calculations on ZnS and SrS have shown that impact ionization due to holes should be a weak process in ZnS and nonexistent in SrS and therefore most attention has been paid to electron processes [31].

Two methods have been used to calculate the characteristics of high field electronic transport in ZnS. The goal of the calculations is to determine the fraction of electrons that are able to excite luminescent centers. One involves the use of band structure calculations and Monte Carlo simulations, in which independent probabilities for scattering events are used to determine the fate of a large number of carriers. The second technique is the lucky-drift transport model. This is an analytical model in which the mean free path for electrons is analyzed with respect to scattering events.

A study by Mach and Mueller [32] employed a Monte Carlo simulation approach that assumed a parabolic conduction band and a primary loss mechanism of longitudinal-optical (LO) phonon emission. The result was that at a field of ~1 MV/cm ballistic, or nearly loss-free, acceleration was predicted. This was said to explain the avalanche breakdown observed in ZnS ACTFEL devices. It was also the basis for the assumption that "all electrons are hot," which was used in some of the other theories related to device efficiency that are discussed in Chapter 3.

Very different results were found in a study by Dür et al. [33] that employed an ensemble Monte Carlo method including a nonlocal band structure, full-band impact ionization rates, and a simplified model for impact excitation of Mn^{2+} impuritues adapted from Bringuier [34]. The results showed that the onset of impact excitation in ZnS:Mn occurs at a field of about 1 MV/cm, consistent with the experimental threshold [35]. Above this threshold the impact excitation rate was found to increase nearly linearly with electric field. The impact excitation threshold was about the same as that for impact ionization of the ZnS host. The quantitative value of the mean free path for impact excitation was found to depend strongly on the electron-phonon coupling constants, and these are not well known. The quantitative impact ionization rates calculated using this model were found to agree fairly well with the experimental values measured by Thompson and Allen [31, 36].

A simpler approach was taken by Bringuier [37], who employed a lucky-drift approach. He made that argument that the full-band Monte Carlo approach may be more accurate, but given the lack of certainty in some physical parameters of II-VI compounds and the poor crystallinity in ACTFEL devices, the lucky-drift approach should suffice to highlight the important factors in device operation. The lucky-drift approach is an extension of the original theory given by Baraff [38]. In this theory two transport modes are considered. One is ballistic transport, which is collision-free. The other is the drift mode, which occurs after the electron has had one collision, which increases the probability of subsequent collisions.

Bringuier has compared the results of the lucky-drift approach to two different band structure approaches. The fraction of electrons beyond 2.12 eV, the energy needed to impact excite Mn^{2+}, at fields of 1 MV/cm and 2 MV/cm for each of the models is shown in Table 2-2 [24].

Hot electron luminescence experiments using undoped ZnS devices by Douglas et al. [39] showed that a significant number of electrons achieve energies of at least 3.7 eV. The results are not quantitative, but qualitatively support the modeling efforts discussed above.

Table 2-2. Fraction of electrons beyond 2.12 eV in ZnS at 300K for F=1 or 2 MV/cm, according to different models [24].

	Brennan [40]	Bringuier [37]	Bhattacharyya [41]
Calculation Parameters	Numerical Empirical pseudopotential band structure	Analytical Mean-free path	Numerical Nonparabolic multivalley band structure
P(2.21 eV) at F=1 MV/cm	~1%	27%	26%
P(2.21 eV) at F=2 MV/cm	~50%	72%	65%

2.6.3 Impact excitation and ionization

Once the conduction electrons reach sufficient energy, there are several excitation mechanisms that are possible in ACTFEL devices. The mechanism discussed most often in reference to ACTFEL devices is direct impact excitation. This is believed to be the primary process involved in excitation in ZnS:Mn devices [24]. The energy threshold for this process is essentially the transition energy for the luminescent center [37]. The probability for this process is determined by the impact cross section of the luminescent center. The average impact length for an electron is found from $l_I=(\sigma N)^{-1}$ where σ is the impact cross section in cm^2 and N is the concentration of centers in cm^{-3}. This has been estimated experimentally by Mach and Mueller to be 4.0 x 10^{-16} cm^2 (±20%) for Mn^{2+} in ZnS, which is near the value of the ionic cross section [42]. Efforts to calculate this value considering both direct and exchange paths (only the latter being appropriate for Mn^{2+} in ZnS) had a very different result of ~10^{-18} cm^2, but in this case the authors note that the effort was only a preliminary one [34].

Another excitation process is impact ionization followed by electron recapture and radiative relaxation. This is believed to be the dominant process involved in excitation of Eu^{2+} in CaS. The theory is that the excited state is too close to the conduction band and under high fields the center is ionized. At a later time an electron is recaptured by Coulombic attraction to the ionized center and radiative relaxation may take place. Two implications of this process are that ionization of the luminescent center results in an additional conduction electron and a modification of the electric field because of the fixed positive charge left in the lattice. This has been shown to have significant effects in the operation of SrS:Ce devices, in which impact ionization of Ce^{3+} ions takes place [26].

There may be other indirect excitation mechanisms, such as energy transfer from electron-hole pairs to luminescent centers [24]. This has been suggested to account for excitation of Tb^{3+}. However, Bringuier has suggested that the experimental approaches often used to make this assignment require significant care be taken, and the results may not be as straightforward as they seem.

Direct impact ionization of the lattice can occur if electrons reach sufficient energy. The energy threshold is normally thought to be either the bandgap of the host material [33, 40] or 1.5x this value [43]. Dür et al. found that impact ionization was required to achieve realistic results for modeling of electron transport in ZnS, and they were able to get reasonable agreement with the ionization rates found experimentally by Thompson and Allen [31, 33, 36]. The ionization function is generally written

$$\alpha_n(F) = \left(\frac{qF}{E_i}\right)\exp\left(-\left(\frac{F_0}{F}\right)^n\right)$$

where α_n is the ionization rate in cm^{-1}, F is the electric field, F_0 is a characteristic field scale, E_I is an effective ionization energy, and n=1,2,...[43].

2.6.4 Radiative decay

When an impurity center is in an excited state, that energy will eventually be dissipated. The relaxation process can occur by either a) emission of a photon, b) non-radiative relaxation, which can be in the form of emission of one or more phonons to the lattice, Auger processes, etc., or c) energy transfer to another center. For application to displays, it is desirable to maximize the first process and to minimize the second. The third case in different situations can be useful or harmful [44].

For a simple two-level system, the rate of return from an excited state to the ground state is given by

$$\frac{dN_e}{dt} = -N_e P_{eg}$$

where N_e is the number of luminescent ions in the excited state, t is the time, and P_{eg} is the probability for spontaneous emission from the excited to the ground state. Integration yields

$$N_e(t) = N_e(0)\exp\left(\frac{-t}{\tau_R}\right)$$

where τ_R ($=P_{eg}^{-1}$) is the radiative decay time, and exponential decay of intensity results [44].

An excited ion in a solid is not only coupled to electromagnetic vibrations, but also to lattice vibrations and can therefore relax through the emission of phonons. The probability of this process, P'_{eg}, leads to the two-level rate equation

$$\frac{dN_e}{dt} = -N_eP_{eg} - N_eP'_{eg}$$

and the fraction of excited ions decaying radiatively is

$$f = \frac{P_{eg}}{P_{eg} + P'_{eg}} < 1.$$

Because P'_{eg} often has an Arrhenius dependence on temperature, the decrease of f with temperature is known as thermal quenching [24].

The assessment of radiative decay becomes more complicated when considering energy transfer from an excited ion to another site such as an unexcited similar ion. It has been shown that in ZnS:Mn devices where the concentration of Mn is >0.1 mol%, as is the case for practical ZnS:Mn ACTFEL devices, the decay behavior becomes non-exponential [45]. The most common way of explaining the decay behavior is by replacing the constant relaxation probability in the two-level differential equation such that

$$\frac{dN_e}{dt} = -N_e k(t)$$

where *k*(t) is a decreasing function of time representing nonradiative decay channels associated with neighboring unexcited Mn^{2+} [24]. The situation is further complicated at high excitation levels where "bimolecular" relaxation processes can occur. Now the differential equation is no longer a linear one and takes the form

$$\frac{dN_e}{dt} = -N_e k_1(t) - N_e^2 k_2(t) .$$

This equation describes a situation in which interaction between neighboring excited Mn^{2+} ions results in less than two photons being emitted, referred to as excited state interaction [24].

2.6.5 Optical outcoupling

For a useful device generated photons must escape the device in the direction of the viewer, so the concept of internal reflection must be considered. The standard device consists of a stack of dielectric layers with the light generated inside the phosphor layer. Typically the phosphor layer has the highest index of refraction in the stack, and all layers have a higher index of refraction than air. Assuming a smooth film, some portion of the light is internally reflected. Figure 2-9 shows some of the scattering processes that can take place inside the device [3]. This can be seen empirically when observing such a device by the significant portion of light that escapes from the edges of the glass. The extent of internal reflection can be estimated [3, 42] by assuming just the phosphor layer (for ZnS n=2.4), and that light is reflected from the metal electrode by

$$\eta_{\text{opt}} = \int_0^{\arcsin\left(\frac{1}{2.4}\right)} \sin\theta d\theta = 1 - \left(1 - \left(\frac{1}{2.4}\right)^2\right)^{0.5} \approx 0.1 .$$

The optical outcoupling efficiency can be improved by increasing the surface roughness and thereby reducing internal reflection. It has been shown that a rough surface can increase outcoupling by more than an order of magnitude [46]. However, too rough a surface can reduce contrast because of increased diffuse scattering [3].

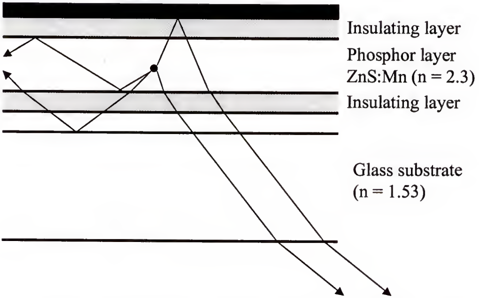

Figure 2-9. Schematic representation of internal reflection in a ZnS:Mn ACTFEL device[3].

2.7 ACTFEL Materials

The requirements and critical characteristics for the materials used in ACTFEL devices are discussed below.

2.7.1 Substrates

For the standard device structure, the primary requirements for the substrate are transparency, smooth surface, and the ability to withstand thermal treatments required by subsequent layers. It is also desirable that the material be inexpensive. For these reasons the most common substrate material is Corning 7059 soda-lime-silicate glass. This is an alkali-free, barium borosilicate glass often used as LCD substrates [47]. It has a softening temperature of ~600°C and large panels can undergo rapid thermal anneals (RTAs) of up to 650°C without significant damage or warping [48]. For research purposes small samples of ~2" x 2" in size may be subjected to RTAs up to ~850°C without significant damage. In addition Corning 7059 is alkali-free to prevent migration of such species into the device. Soda lime glass has been used with a diffusion barrier to alkali metals [3]. For higher temperatures glass-ceramics are available which meet the substrate requirements, but these materials are expensive and not economically viable substrate materials for commercial applications.

The requirements for the inverted structure devices are a smooth surface and the ability to meet the thermal considerations for processing of subsequent layers. For the inverted structure in Figure 2-1b the substrate acts as part of the device, comprising the bottom insulator, and electrical properties must be considered. These are discussed in the following section. For devices with the structure in Figure 2-1(c), in which the bottom electrode is deposited on top of the substrate, alumina substrates have been used [21]. For active matrix applications, the on/off state of the pixels are controlled by transistors located underneath each pixel, and the silicon-based IC array is used as the substrate [3].

2.7.2 Transparent Electrodes

For the standard device structure the first layer deposited onto the glass substrate is the transparent conductor. This layer has three critical materials requirements. First it must be sufficiently conductive to not affect the RC time constant of the device. Second, it must be as transparent as possible in the spectral region of the emission from the device to minimize absorption and/or color perturbation. Finally it must withstand the thermal processing of subsequent layers. The material most commonly used for this application is indium-tin-oxide (ITO) [3]. This is normally an alloy of 90 wt% In_2O_3 and 5-10 wt% SnO_2 sometimes doped with F. It has been deposited by pulsed-laser deposition, e-beam evaporation, DC magnetron sputtering, RF magnetron sputtering, plasma ion-assisted deposition, spray pyrolysis, chemical vapor deposition, and atomic layer deposition [3, 49-58]. ITO thicknesses of 200 nm are typical, and good transparency (>90%) can be obtained with a resistivity of $\sim 1 \times 10^{-4}$ Ω-cm, providing a sheet resistance of ~ 5 Ω/□. In addition, ITO is easily patterned with standard photolithography and wet or dry etching.

Care must be taken when using ITO as an electrode. The primary cause for high conductivity in ITO is oxygen deficiencies, since oxygen vacancies act as shallow donors which are efficiently ionized at room temperature [57]. The concentration of oxygen vacancies can be affected by annealing at high temperatures. It is important to choose neighboring layers (substrate and bottom insulator) that do not interact significantly with the ITO layer during subsequent thermal processing.

Another transparent conductor commonly used in inverted structure devices is ZnO:Al [20], but $CdSnO_3$ and undoped ZnO have been used as well [3].

2.7.3 Opaque Electrodes

For the standard structure, the requirements for the opaque electrode are not stringent because it is the last layer deposited. The layer must have sufficient conductivity, which for most common metals is far better than that of the transparent electrode, and good adhesion to the top insulator is also critical. The most common material for several reasons is aluminum. First, it is inexpensive and easily deposited by evaporation or sputtering. Second, it has a low melting temperature. Third, it exhibits desirable wetting characteristics to many common insulator materials, and this provides the possibility for self-healing breakdown by fusing of the metal surrounding a short. The typical thickness for this layer is 100-200 nm. One tradeoff to be considered for Al as an electrode is its high reflectivity, which enhances brightness but reduces the contrast in a display. The problem has been effectively dealt with by adding either a dark layer above the phosphor or by adding a circular polarizer, which eliminates specular reflection [3]. Both of these techniques reduce the brightness of the device.

For inverted structures in which the electrode is deposited on the bottom of the substrate, again aluminum is commonly used since conductivity, cost, and ease of processing are the major concerns. However for the other type of inverted structure in which the opaque electrode is deposited below the rest of the EL device, the additional requirement for thermal stability is added. Au, Mo, Ta, and W are candidates for this type of structure.

2.7.4 Insulators

The insulating layers of an ACTFEL device are an integral part of the capacitive nature of the device, as seen in the equivalent circuit model in section 2.5.2. The bottom insulator undergoes the same thermal processing as the phosphor layer and therefore must have thermal stability and chemical compatibility with the bottom electrode and phosphor layer in addition to good adhesion. The most important electrical requirements are that the insulators prevent current flow through the device and withstand electrical breakdown under fields used in the device, usually up to 2 MV/cm. In addition the characteristics of the phosphor-insulator interface have been shown to affect the depth and concentration of interface states [25] and therefore significantly influences the device performance. The critical properties for reliable, efficient performance are as follows [3]:

1. High dielectric constant, $\varepsilon_o\varepsilon_r$
2. High dielectric breakdown electric field, F_{BD}
3. Small number of pinholes and defects
4. Good adhesion
5. Small loss factor, $\tan\delta$

ε_o and ε_r are the dielectric constant of vacuum and the relative dielectric constant of the layer, respectively. $\tan\delta$ is a measure of the dissipative characteristics of the capacitor and is equal to $1/(2\pi fCR)$, where f is the frequency, C is the capacitance, and R is the resistance of the insulating layer.

In order to optimize the insulating layers for device efficiency, it is useful to revisit the electrical behavior using the relationships presented in section 2.5.2. First, equations 2-1 and 2-2 show that the proportion of the voltage which is across the phosphor rather than the insulators is governed by the relative capacitance of the phosphor and insulating layers. To maximize the portion of the applied voltage dropped across the phosphor layer, the capacitance of the insulators should be maximized while that of the phosphor is minimized. The insulator and phosphor capacitances are determined by the equation

$$C = \frac{\varepsilon_r \varepsilon_o}{t} \qquad \text{2-6}$$

where t is the layer thickness. It is apparent that to optimize the insulator capacitance, either the dielectric constant should be maximized as noted in the above list of attributes, or the layer thickness should decrease. Indeed it is useful to minimize the insulator thickness in a device. However a lower limit on thickness is set by two factors. The first is the third attribute in the list of characteristics, namely a small number of defects and pinholes. The thinner the insulating layer the larger the probability of having defects and pinholes in the film. This is primarily a processing issue and careful process control can minimize the problem. The second limitation is the breakdown electric field strength, also noted in the above list. It was shown in Equations 2-3 and 2-4 that the voltage across the insulating layers increases more rapidly above threshold in devices which exhibit field clamping in the phosphor layer. Different materials may be used to maximize the dielectric constant, and a figure of merit has been used which is the product of the dielectric constant and the electric field breakdown strength. Generally speaking it has been observed that materials with a higher dielectric constant have a small breakdown strength, and vice versa. In addition, the high dielectric constant materials tend to have a propagating breakdown characteristic, meaning that small defects lead to catastrophic failure. Table 2-3 gives a list of critical properties for materials that have been used as dielectric layers in ACTFEL devices.

2.7.5 Phosphor Layer

The phosphor layer materials consists of a host material and a luminescent center, each discussed below.

Table 2-3. List of insulators used in ACTFEL devices with values for the properties of interest [3].

Insulator	Deposition Method*	ε_r	F_{BD} [MV/cm]	$\varepsilon_0\varepsilon_r F_{BD}$ [μC/cm^2]	Breakdown Mode**
SiO_2	Sputtering	4	6	2	SHB
SiO_xN_y	Sputtering	6	7	4	SHB
SiO_xN_y	PCVD	6	7	4	SHB
Si_3N_4	Sputtering	8	6-8	4-6	SHB
Al_2O_3	Sputtering	8	5	3.5	SHB
Al_2O_3	ALE	8	8	6	SHB
SiAlON	Sputtering	8	8-9	4-6	SHB
Y_2O_3	Sputtering	12	3-5	3-5	SHB
Y_2O_3	EBE	12	3-5	3-5	SHB
$BaTiO_3$	Sputtering	14	3.3	4	SHB
Sm_2O_3	EBE	15	2-4	3-5	SHB
HfO_2	Sputtering	16	0.17-4	0.3-6	SHB
Ta_2O_5-TiO_2	ALE	20	7	12	SHB
$BaTa_2O_6$	Sputtering	22	3.5	7	SHB
Ta_2O_5	Sputtering	23-25	1.5-3	3-7	SHB
$PbNb_2O_6$	Sputtering	41	1.5	5	SHB
TiO_2	ALE	60	0.2	1	PB
$Sr(Zr,Ti)O_3$	Sputtering	100	3	26	PB
$SrTiO_3$	Sputtering	140	1.5-2	19-25	PB
$PBTiO_3$	Sputtering	150	0.5	7	PB
$BaTiO_3$****	Press/sinter	5000	?	?	?
Westaim proprietary***	Press/sinter	1700	?	?	?

*PCVD - plasma-assisted chemical vapor deposition; ALE – atomic layer epitaxy; EBE – electron-beam evaporation
**SHB – self-healing breakdown mode; PB – propagating breakdown mode
***ceramic substrate, inverted structure
****Ref.[20]

2.7.5.1 Host material

Among the critical properties for the host materials are the following [3]:

1. Band gap must be sufficiently large to allow emission from the luminescent center without significant absorption. For complete visible transmission this requires a band gap of at least ~3.1 eV.

2. Host must be non-conducting below threshold. This is required for a voltage drop and subsequent electric field across the phosphor layer, leading to the sub-threshold capacitive nature of the phosphor.
3. Host must allow for efficient acceleration of electrons. This requires that the breakdown field of the phosphor must be at least 1 MV/cm. In addition, the host should have good crystallinity and a low phonon coupling coefficient (Frolich's constant) to minimize electron scattering. A more detailed discussion of the high field transport properties was given in Section 2.6.2.
4. Host must provide a suitable substitutional lattice site for the luminescent center. This will be discussed in more detail in Section 2.7.5.3.

These requirements have historically been met best by sulfur-based compounds, especially ZnS, SrS, CaS, $SrGa_2S_4$, and $CaGa_2S_4$ [5, 19, 59, 60]. The ZnS system and investigations of oxide-based phosphors will be treated in more detail in Sections 2.9 and 2.10, respectively. A summary of the properties of the sulfides is given in Table 2-4.

Table 2-4. Properties of some common ACTFEL host compounds [3].

Property	IIb-VIb	IIa-VIb		Thiogallate		
Compound	ZnS	CaS	SrS	$CaGa_2S_4$	$SrGa_2S_4$	$BaGa_2S_4$
Melting Pt. (°C)	180-1900	2400	>2000	1150	1200	1200
Band Gap (eV)	3.6	4.4	4.3	4.2	4.4	4.1
Transition Type	Direct	Indirect	Indirect			
Crystal Structure*	ZB,W	Rock salt	Rock salt	Orth.	Orth.	Cubic
Lattice constant (Å)	5.409	5.697	6.019	a=20.09 b=20.09 c=12.11	a=20.84 b=20.49 c=12.21	12.66
Dielectric const.	8.3	9.3	9.4	15	14	15
Ionicity	0.623	>0.785	>0.785			

*ZB = zinc blende; W = wurtzite; Orth. = orthorhombic

2.7.5.2 Luminescent centers

The spectral properties, and to a large extent the temporal properties, of optical emission are primarily influenced by the activator impurity in the phosphor. There are two types of luminescent centers commonly used in phosphor applications. In many lamp and CRT phosphors, luminescence results from recombination of electrons and holes trapped in deep donor and deep acceptor levels, respectively. The most common examples of this type of phosphor are based on a ZnS host, with some combination of Ag, Cu, Au, Al, and Cl added as the acceptor and donor impurities to tailor the spectral properties and efficiency. The maximum recombination energy is determined by the band gap energy of the host, the trap depths, and the exciton binding energy. This class of luminescent center is not used in ACTFEL devices because the electron-hole pairs are unstable under high fields and the luminescence is effectively quenched [3, 4].

The second type of center is a localized transition between electronic states of an isolated dopant ion. This dopant ion is typically either a transition metal such as Mn^{2+}, Cr^{2+}, Ti^{4+}, Cu^{+}, Ag^{+}, a rare earth ion such as Eu^{3+}, Eu^{2+}, Ce^{3+}, Tb^{3+}, or Tm^{3+}, or an s^2 configuration ion such as Pb^{2+}, or Bi^{3+}[3, 44].

Without going into a detailed discussion of the underlying physics, the general emission characteristics of these ions can be separated into several categories based on the electronic configuration of the ground and excited states. One characteristic of importance in terms of both understanding the luminescent process and for application to displays is the radiative decay time. The mathematical description of decay behavior for a two-level system was described in Section 2.6.4. The decay time is determined primarily by two selection rules related to the electronic configuration of the ground and excited states, as well as the surroundings of the ion [44]. One of these selection rules is referred to as the parity selection rule, which forbids transitions between levels of the same parity, i.e. transitions within the *d* shell, within the *f* shell, or between the *d* shell and *s* shell are forbidden. The other selection rule is the spin selection rule, which forbids transitions between configurations with different spin states. Forbidden transitions have longer decay times [44].

The transition metal ions mentioned above all have a d^n valence configuration, and emission spectra are all characteristic of intra-shell *d-d* transitions. They are therefore all forbidden by the parity selection rule [44], and their emission is usually broad band (although Cr^{3+} can exhibit line emission in some instances). Therefore decay times for the transition metals can be in the range of 100 μs to several ms, depending on the spin selection rule and symmetry. Another general characteristic of the transition metal activators is that because the transitions originate in the valence *d*-shell, they are strongly influenced by the crystal field and ligand fields of the host.

There are two very different types of transitions observed for rare earth ions. The first is observed in Ce^{3+} and Eu^{2+} in which the ground state configurations have a 4*f* valence. The excited states have one or more electrons promoted to the 5*d* orbital. Therefore the parity selection rule is not in effect. This means that the decay times can range from tens of ns for Ce^{3+}, which is spin allowed, to several μs for Eu^{2+}, which is spin forbidden [44, 61]. The 5*d* excited state is strongly affected by the surroundings and symmetry of the ion, such that Ce^{3+} emission can range from near-UV to green [44], while that of Eu^{2+} can range from near-UV [44] to red [59] depending on the host.

The second type of rare earth transition is an intra-shell *4f*-*4f* transition [44, 61]. This type of transition is seen in Eu^{3+}, Tb^{3+}, and most other trivalent rare earths. The transitions are all parity forbidden and have decay times typically of several ms. The spectra are characterized by line transitions, and are insensitive to the surroundings and symmetry of the ion since the 4f electrons are shielded by the 6s orbital.

The excitation cross-section of the luminescent center, σ, is discussed frequently in the literature [3, 5, 16, 24, 37, 42, 62, 63]. This value relates the concentration of the centers to the mean free path for excitation through the simple relation

$$l_i^{-1} = \sigma N$$

where N is the concentration of centers and l_i is the impact length. Some groups have directly measured the value for σ of Mn^{2+} in ZnS by measuring the efficiency and calculating the value from other known parameters [42]. The resulting value was similar to the physical ionic cross section. However, other efforts to predict impact cross sections for Mn^{2+} and other ions have shown that this is an extremely difficult task and accurate values are elusive [34], thereby impeding the ability to predict device efficiency. It is reported in the literature that it is desirable to have a large luminescent center impact cross section for good device efficiency, however there is not much practical value to this statement as the cross section has only been determined by measuring efficiency, and it is an intrinsic property of the atom.

2.7.5.3 Host-center systems

In addition to considering the electrical properties and processing conditions of the host and the luminescent properties of the center, one must consider the compatibility and interrelationships between the two. The size mismatch of the activator on the cation site is important, as is the valence match (or mismatch). Listed in Table 2-5 are the valence and ionic radius of common ACTFEL host cations and dopants. Minimizing the size and valence mismatch allows the incorporation of the dopant with the least concentration of induced defects.

The most commonly used and best performing EL phosphor system is Mn-doped ZnS. This system will be discussed in more detail in Section 2.9. This phosphor can be filtered to obtain both green and red emission. To complete a full color display, there has been a tremendous amount of effort devoted to the development of a sufficiently bright and stable, saturated blue phosphor. Promising results were obtained for SrS:Ce. However the blue-green chromaticity and low luminance when filters are used were the primary limitations for this phosphor [5]. Nevertheless full color displays were developed based on this material. Promising results were also obtained for (Sr,Ca)Ga_2S_4:Ce, which had superior chromaticity, but lower brightness and greater difficulty in deposition and processing [5]. Recently excellent performance has been demonstrated for blue-emitting SrS:Cu,Ag [64, 65]. A list of results obtained for sulfide-based phosphors is given in Table 2-6. More details regarding these phosphor systems are available in the literature [5]. Results for oxide-based phosphors are discussed in Section 2.10.

2.8 Electrical and Optical Device Characterization

Since characterization of the electrical and optical properties of EL materials and devices are unique and not widely practiced, they will be discussed in this review of the literature.

Table 2-5. List of valence and ionic radius for cations commonly used in ACTFEL hosts, a well as common dopant ions [66].

Ion	Radius [Å](CN)	Ion	Radius (Å) (CN)	Ion	Radius (Å) (CN)
Zn^{2+}	0.60 (4)	Mn^{2+}	0.66 (4)	Tm^{3+}	0.88 (6)
Ca^{2+}	1.00 (6)	Ce^{3+}	1.01 (6)	Eu^{3+}	0.95 (6)
Sr^{2+}	1.18 (6)	Cu^{+}	0.77 (6)	Eu^{2+}	1.17 (6)
		Ag^{+}	1.15 (6)	Cr^{3+}	0.62 (6)
		Tb^{3+}	0.92 (6)		

CN = Coordination number

Table 2-6. ACTFEL phosphor systems and device performance [3, 48].

Phosphor	Color	CIE coordinates		B_{40} (cd/m^2)		E_{40} (lm/W) 1 kHz
		X	Y	60 Hz	1 kHz	
ZnS:Mn	Amber	0.50	0.50	585*	5000	2-4
ZnS:Sm,F	Red-orange	0.60	0.38	8	120	0.05
ZnS:Sm,Cl	Red	0.64	0.35	12	200	0.08
CaS:Eu	Red	0.68	0.31	12	200	0.05
ZnS:Mn/filter	Red	0.65	0.35	75	1250	0.8
SrS:Eu	Red	0.60	0.39	31		0.18**
SrS:Eu,Cu	Red	0.60	0.39	91		0.5**
CaSSe:Eu	Red	0.66	0.33	25		0.25**
ZnS:Tb,O,F	Green	0.30	0.60	100		1.0**
ZnS:Tb,F	Green	0.30	0.60	125	2100	0.5-1.0
ZnS:Mn/filter	Yellow-green	0.47	0.53	160		1.0**
ZnS:Tb	Green	0.30	0.60	90		0.6
CaS:Ce	Green	0.27	0.52	10	150	0.1
SrS:Cu,Ag	Blue	0.15	0.13	20		0.15**
SrS:Cu,Ag	Blue	0.15	0.21	35		0.23**
SrS:Cu	Blue	0.16	0.28	52		0.13**
SrS:Ce/filter	Green-blue	0.13	0.18	26		0.15**
SrS:Ce	Green-blue	0.19	0.38	65	900	0.44
ZnS/SrS:Ce	Green-blue	0.26	0.47	96	1500	1.3
ZnS/SrS:Ce/filter	Green-blue	0.10	0.26	14	220	0.2
(Sr,Ca)Ga_2S_4:Ce	Blue	0.15	0.15	7		0.02**
CaGa_2S_4:Ce	Blue	0.15	0.19	13	210	

*This work

**60 Hz

The electrical characterization of an ACTFEL device typically involves measurement of instantaneous external current or charge and applied voltage. Various characteristics of the device are then obtained by manipulation of this data. One of the experimental difficulties is the separation of capacitive current and conduction current. There are two common approaches to measurement of the underlying data with this in mind. One important assumption common to all three approaches is that the device capacitance does not change significantly above threshold.

The first approach for separating capacitive and conduction current involves the use of a variable capacitor bridge [16]. The capacitor is balanced below threshold, where there is a negligible amount of conduction current, to match the total device capacitance. Above threshold this effectively subtracts the equivalent capacitive current of the device and only conduction current is measured. This circuit is shown schematically in Figure 2-10. The applied voltage is found by

$$V_{ap} = V_1 - V_2$$

and the conduction current is

$$i_{cond} = \frac{V_2 - V_3}{R}.$$

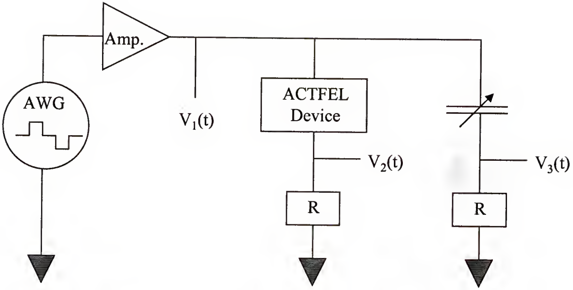

Figure 2-10. Schematic diagram of circuit used to measure conduction current by balancing the bridge below threshold [16].

The second technique employs a Sawyer-Tower circuit that uses either a sense resistor or a sense capacitor [23, 67] to measure the external current or charge, respectively. This circuit is shown in Figure 2-11. There are two ways in which this type of circuit has been used to measure conduction current. The simplest is to use a triangular waveform or a trapeziodal waveform with a slow voltage slew rate [68-73]. Since the slew rate of applied voltage is small, the capacitive current is also small. When threshold is reached the conduction current is large and the capacitive current, being constant, can be easily subtracted out by zeroing the pre-threshold baseline. This technique is simple and very useful in studying device physics, but has the disadvantage of using a waveform different from that used in commercial devices. Since ACTFEL properties can change with waveform, it is often desirable to study them under conditions used in commercial displays.

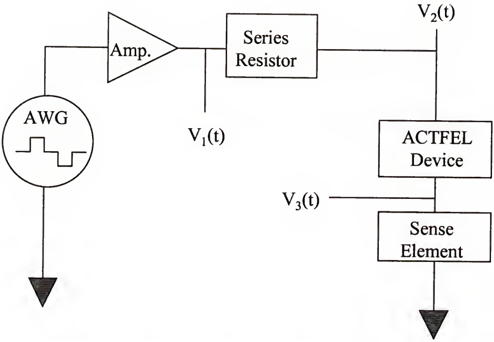

Figure 2-11. Schematic diagram of circuit used to measure conduction current using a Sawyer-Tower bridge [23].

A technique which has been extensively developed to calculate conduction current from the Sawyer-Tower circuit using standard trapezoidal waveforms (as well as other arbitrary waveforms) has been developed by Wager et al., and a more extensive review of this approach can be found elsewhere [23]. This technique uses the instantaneous values for external voltage and current or charge and, assuming the phosphor and insulator to be ideal electrical components, uses simple circuit equations to calculate the conduction current and the conduction charge. Some of the basic relationships are given below.

The applied waveform is presented in Figure 2-12 using a labeling scheme common in the literature [23]. The waveform is trapezoidal, typically with a 5 μs rise, 30 μs dwell, and 5 μs fall. The importance of all labeled points in Figure 2-12 are selfexplanatory, with the exception of points B and G, which correspond to the voltage at which conduction charge becomes significant.

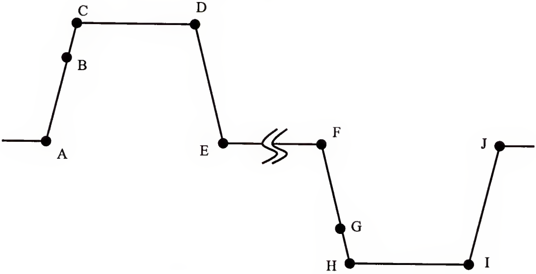

Figure 2-12. Schematic diagram of the voltage waveform used in ACTFEL device operation and characterization. Important features are labeled and discussed in the text.

The applied voltage is found by

$$V_{ap}(t) = V_2(t) - V_3(t).$$

When using a sense resistor, the external charge is simply the time integrated current, such that

$$i(t) = \frac{V_1(t) - V_2(t)}{\mathrm{R}_{\mathrm{series}}}$$

$$q_{ext}(t) = \int_0^t i(t)dt$$

where $\mathrm{R}_{\mathrm{series}}$ is the series resistance.

If using a sense capacitor, these values are determined by

$$q_{ext}(t) = \mathrm{C}_s V_3(t)$$

$$i(t) = \frac{dq_{ext}(t)}{dt}$$

where C_s is the sense capacitance. Both $V_{ap}(t)$ and either $i(t)$ or $q_{ext}(t)$ data are normally centered around the y-axis before further analysis. The procedure and significance of this adjustment is discussed in the literature [74, 75].

One of the common analytical techniques for the characterization of ACTFEL devices which uses the above information is known as external charge-applied voltage, or Q-V, analysis. The Q-V behavior of the simple equivalent circuit discussed in Section 2.5.2 (and shown in Figure 2-6) is shown in Figure 2-13. However, in actual devices using a trapezoidal waveform, two additional features are observed. Figure 2-14 shows schematically the behavior typical of a ZnS:Mn device, sometimes referred to as an "ideal" device. The A-J labeling scheme from Figure 2-12 is included in Figure 2-14. The conduction charge and polarization charge, discussed for the simplified device, are still seen in Figure 2-12. The two new features are the relaxation charge and leakage charge. Relaxation charge occurs when the applied voltage reaches its maximum value (or near maximum value in a real case) and reflects current which flows during the dwell, or C-D portion of the waveform. The name refers to the fact that at a constant applied voltage, conduction charge creates an opposing electric field that relaxes the field across the phosphor layer. The leakage charge occurs once the applied voltage reaches zero and refers to current that flows in the opposite direction as the previous pulse due to the polarization field present at the end of the pulse.

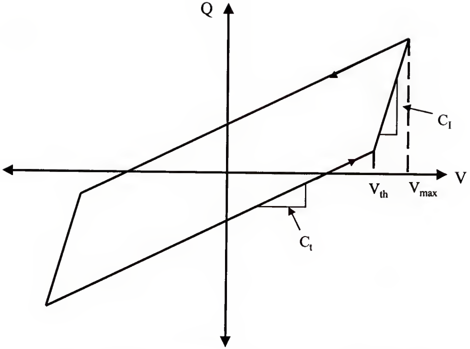

Figure 2-13. External charge-voltage (Q-V) characteristics of the ideal circuit shown in Figure 2-2.

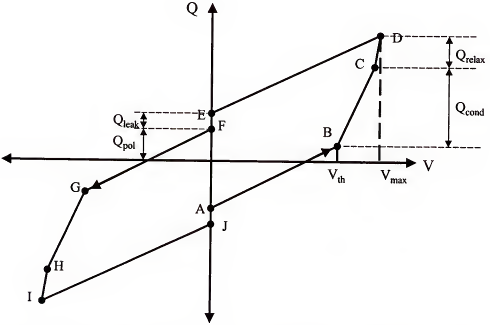

Figure 2-14. Schematic diagram of the Q-V characteristics of an ACTFEL device. Letters refer to the labeling scheme in Figure 2-12.

As mentioned previously, the value of interest is often the internal or conduction charge and/or current. This value is denoted $q_{int}(t)$, or just $q(t)$, and is found from

$$q(t) = \frac{(\mathrm{C_i} + \mathrm{C_p})}{\mathrm{C_i}} \mathrm{C_s} v_3(t) - \mathrm{C_p}\left[v_2(t) - v_3(t)\right]$$

where $\mathrm{C_i}$ and $\mathrm{C_p}$ are the phosphor and insulator capacitances, respectively. It is important to note that (1) this assumes accurate values for $\mathrm{C_i}$ and $\mathrm{C_p}$ are known, and (2) this analysis (as well as data obtained using the balanced bridge circuit) assumes that the device capacitance does not change above threshold.

Another value of interest is the phosphor field, f_p, rather than just the applied voltage. This is also found using the transferred charge and applied voltage data by the relation

$$f_{\mathrm{p}}(t) = \frac{1}{d_{\mathrm{p}}} \left\{ \frac{\mathrm{C_s} v_3(t)}{\mathrm{C_i}} - \left[v_2(t) - v_3(t)\right] \right\}$$

where d_{p} is the phosphor thickness. Note that the determination of this value requires the knowledge of accurate values for the phosphor thickness and insulator capacitance.

The internal charge plotted against phosphor field , or Q-$\mathrm{F_p}$, can be used to examine various properties of the device such as extent of field clamping and field relaxation. A schematic Q-$\mathrm{F_p}$ diagram is given in Figure 2-15, which shows some of the values that can be obtained from this type of plot. Note that unlike a Q-V plot, the Q-$\mathrm{F_p}$ plot occurs in a counterclockwise fashion. Also, the values of the insulator and phosphor capacitance are often used as parameters to obtain the most “ideal” shape, meaning vertical slopes for the B-C and G-H portions of the curve and horizontal slopes for the D-E and I-J portions of the curve. One interpretation of the capacitance adjustment has been that a larger capacitance value used for the Q-$\mathrm{F_p}$ plot compared to the physical value, which is calculated from the layer thickness and dielectric constant, refers to a larger amount of space charge [76].

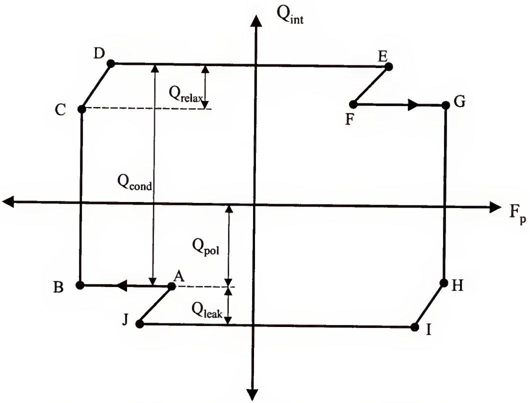

Figure 2-15. Schematic diagram of a ZnS:Mn type Q-F_p plot. Letters refer to the labeling scheme in Figure 2-12.

Another type of electrical analysis commonly used to characterize ACTFEL devices is called a dynamic capacitance-voltage, or C-V plot. Using the same $q^{ext}(t)$ or $i^{ext}(t)$ data and V_{ap}(t) data collected under steady state excitation, the dynamic capacitance is found from the charge or current data by

$$c(v) = \frac{dq_{ext}(t)}{dv(t)}$$

or

$$c(v) = \frac{i(t)}{\left(\frac{dv(t)}{dt}\right)}.$$

A schematic set of C-V curves is shown if Figure 2-16 representing 3 different values of V_{max}. Below threshold the capacitance value represents the total device capacitance and there is usually good agreement with the physical value calculated from the layer thicknesses and dielectric constants [23]. In the simple device model discussed in Section 2.5.2 and shown in Figure 2-6, the above threshold capacitance would equal that of the insulators, while in reality there are three possible cases. If there is insufficient charge to shunt the phosphor capacitance, then the above threshold capacitance value will be below that of the insulator capacitance. If there is sufficient charge available and no dynamic space charge, then the dynamic capacitance will be approximately equal to the insulator capacitance. However, if there is dynamic space charge, the above threshold C-V behavior will saturate to a value above the insulator capacitance. This is sometimes seen by a rapid increase in capacitance to a large value followed by a decrease to a value greater than the insulator capacitance.

Another useful tool to characterize the electrical properties of an ACTFEL device is a maximum charge-maximum voltage analysis, also known as a Q_{max}-V_{max} or transferred charge capacitance plot. The last name alludes to the fact that the units for the slope of a Q_{max}-V_{max} plot are Farads, and therefore can be analyzed in the context of the capacitive nature of the device. This type of plot is obtained by measuring the transferred charge in a device for a range of applied maximum voltages. The internal charge is then determined from the external values by any of the means discussed previously and plotted vs. maximum voltage. The behavior of the ideal circuit in Section 2.5.2 is shown schematically in Figure 2-17. The critical issues in a Q_{max}-V_{max} plot are similar to the C-V plot in that the above threshold capacitance should equal the insulator capacitance for an ideal device. For a case in which there is insufficient conduction charge, the slope is less than the insulator capacitance. More often there is an above threshold capacitance overshoot. In evaporated ZnS:Mn there is a higher slope just above threshold, which then saturates to the approximately the insulator capacitance. On the other hand in SrS:Ce the above threshold slope is consistently larger than the insulator capacitance, as demonstrated by Wager [23].

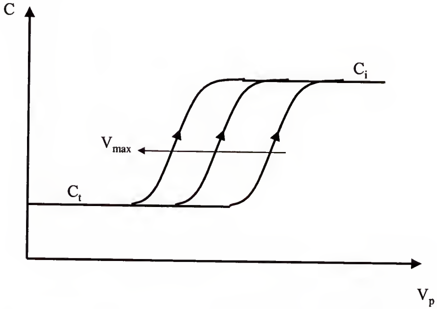

Figure 2-16. Schematic diagram of a C-V plot for three different values of V_{max}.

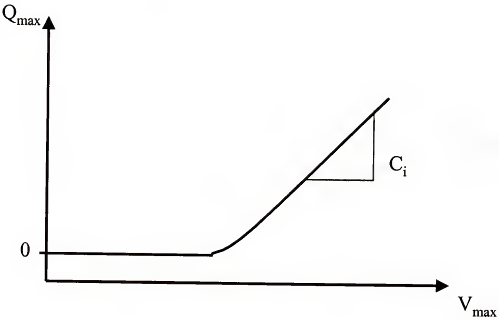

Figure 2-17. Schematic diagram of Q_{max}-V_{max} plot for an ideal device.

2.9 ZnS:Mn as an ACTFEL Phosphor

As discussed in Section 2.3, the ZnS:Mn system has a long history in ACTFEL devices, and is still the most efficient ACTFEL phosphor known. A review is given regarding the physical nature of the system as well as the electrical and optical properties of the phosphor system. A discussion on the nature of intrinsic and extrinsic point defects in ZnS is also given.

2.9.1 Physical Properties

A brief review of the physical nature of the ZnS system is given here, and has been given in more detail by Zhai [77]. The general properties of the compound are given in Table 2-7. The compound exists at room temperature in two different crystal structures, a stable cubic phase (sphalerite) and a metastable hexagonal phase (wurtzite). A ball and stick model for (a) a unit cell of the cubic phase is shown in Figure 2-18, along with (b) a metal-centered model of the cubic phase showing the symmetry of the cation site doped with Mn. The two phases have similar properties and, importantly, similar symmetry for both the cation and anion sites.

Table 2-7. Physical properties of ZnS [66].

Parameter	Value	
	Zincblende	Wurtzite
Lattice constant (Å)	5.409	a = 3.814; c = 6.258
Mass density (g/cm^3)	4.08	4.1
Melting Point (K)	2100	2100
Heat of Formation (kJ/mol(300K))	477	-206
Specific Heat (J/kg-K(300K))	472	
Debye Temperature (K)	530	

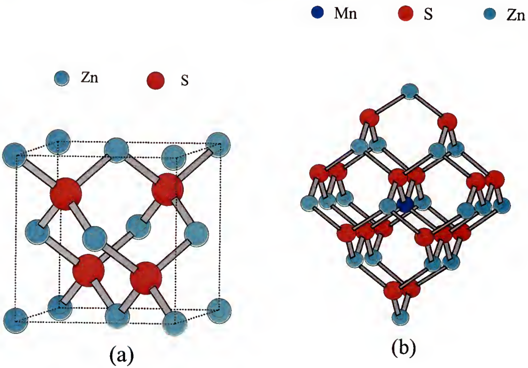

Figure 2-18. (a) Unit cell for the zincblende structure, and (b) metal-centered cluster showing symmetry of activator for ZnS:Mn.

The phosphor layer in ZnS:Mn ACTFEL devices has been deposited using a variety of physical- and chemical-vapor deposition methods including electron beam evaporation, co-evaporation, thermal evaporation, sputtering, atomic layer deposition (ALD-often referred to in the literature as ALE, or atomic layer epitaxy), chemical vapor deposition (CVD), and metal-organic chemical vapor deposition (MOCVD) [77].

2.9.2 Optical Properties

Pure cubic ZnS has a bandgap of 3.6-3.7 eV (see Table 2-7), is therefore transparent throughout the visible range, and has an index of refraction of 2.4 [62, 66].

The dominant radiative transition seen for the Mn^{2+} ion is the $^4T_1 \rightarrow {}^6A_1$ transition, which is a $d \rightarrow d$ transition and is both spin and parity forbidden [44]. Both the zincblende and wurtzite cation sites have tetrahedral symmetry and therefore lack inversion symmetry. This somewhat relaxes the selection rules, and the resulting characteristic exponential decay time for luminescence from Mn^{2+} in cubic ZnS is reported to be 1.77 ms [78] while that of hexagonal symmetry is 1.3 ms [45]. While this is the characteristic time for radiative decay, the actual decay behavior of useful devices is quite different as is discussed below in Section 3.4.2.2. Figure 2-19 shows the Tanabe-Sugano diagram for the energy levels of the d^5 configuration for octahedral symmetry. This diagram shows the various energy levels as a function of crystal field, Δ, and explains some of the optical characteristics of the Mn^{2+} transitions. The $^4T_1$ and $^6A_1$ levels are non-parallel and the transition energy is therefore strongly affected by the crystal field. The emission wavelength in ZnS is 585 nm, while in less covalent oxide compounds such as Zn_2GeO_4 the emission wavelength is just 540 nm, consistent with the Tanabe-Sugano diagram.

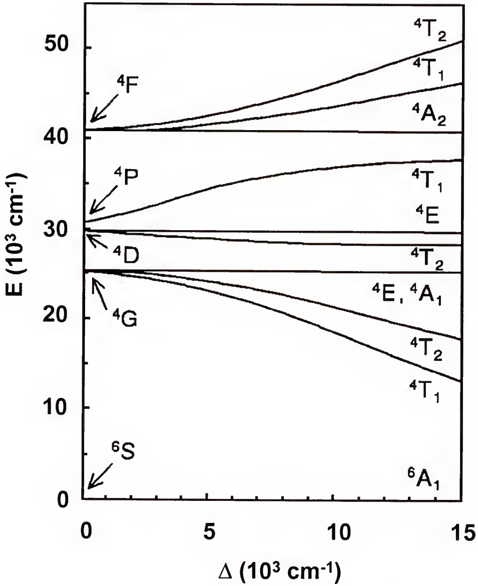

Figure 2-19. Simplified Tanabe-Sugano diagram for the energy levels of the $3d^5$ configuration in divalent manganese. Some energy levels are omitted for clarity [44].

2.9.3 Electrical Properties

The interest in zinc sulfide as a phosphor host is partly due to its interesting combination of electrical properties. It has a moderately large direct band gap, a small electron effective mass, the electron-optical phonon coupling is not large [36], and it can be doped n-type with a resistivity as low as 0.2 Ω-cm [79]. Some of the bulk electrical properties of ZnS are given in Table 2-8. The calculated band structure for cubic ZnS is shown in Figure 2-20 along with that of GaN and SrS [31].

Table 2-8. Bulk electrical properties of ZnS [36, 40, 41, 66].

Parameter	Value
Energy band gap (eV)	3.6-3.7
Impact ionization threshold energy (eV)	3.60*
Polar optical-phonon energy (eV)	0.044
Sound velocity (cm/s)	5.20×10^5
Low-frequency dielectric constant	8.32
High-frequency dielectric constant	3.60
Electron effective mass, m^*	$0.27m$
Electron mobility (cm^2/V-s)	180
Hole mobility (cm^2/V-s)	5
Fröhlich's constant, α (electron-optical phonon coupling)	0.6

* This value, given by Brennan [40], is close to that given by Dür [33]. Other sources approximate this value as $(3/2)^*E_g$, or ~5.4 eV [26, 43].

2.9.4 Point Defects in ZnS

2.9.4.1 Intrinsic point defects

The nature and concentration of intrinsic defects in ZnS has been a topic of much interest because of the influence these defects can have on the optical and electrical properties of semiconductors. One complication is that data regarding equilibrium intrinsic defects are generally not valid for films deposited by different techniques, under different conditions, or onto different substrates. In addition, identification of defects and association with particular electronic levels is often difficult [80]. As a binary compound, the types of intrinsic defects include vacancies and interstitials on both the cation and anion sublattices. Antisite defects are expected to be much less important than in III-V compounds because of the larger chemical differences between the constituents [81], and neither antisites nor interstitials have been definitively observed under "normal" conditions [80]. Point defects play an important role in II-VI semiconductors in terms of processing and diffusion mechanisms. They can also play a critical role in determining the electrical properties of these compounds. Self-compensation, such as the role of cation vacancy pairing with donors, is common throughout the II-VI compounds [81].

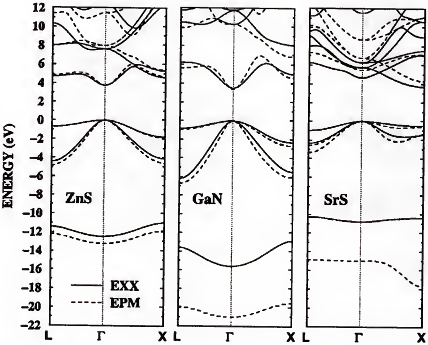

Figure 2-20. Energy band structures for cubic ZnS, GaN, and SrS calculated using exact exchange (solid curves) and empirical pseudopotential (dashed curves) methods [31].

The most well-characterized intrinsic point defect in ZnS and the other II-VI compounds is the cation vacancy. The doubly ionized Zn vacancy (V_{Zn}^{2+}) is reported to create a defect level ~1.0-1.1 eV above the valence band in ZnS [82-84]. This value for V_{Zn}^{2+} is close to the hole trap depth of 1.2 eV used by Hitt et al. [26] for accurate simulation of ZnS devices. A singly ionized V_{Zn}^{+} is reported to create a defect depth in the range of 0.2-0.6 eV above the valence band, depending on the author [83, 84]. Electrical characterization of ZnS:Mn ACTFEL devices has revealed an estimated concentration of hole traps of 7 x 10^{16} cm^{-3}, tentatively attributed to V_{Zn} [85]. Positron lifetime spectroscopy has revealed that for ZnS there is a concentration of low to mid 10^{16} cm^{-3} for divacancy defects, or pairs of compensating cation and anion defects [86].

There is less information regarding the electrical nature of anion vacancies in II-VI compounds [82, 87]. This is known as the F-center in ZnS [80]. Impurity electro-absorption and photoconductivity measurements of Cl-doped ZnS by Georgobiani revealed acceptor levels 0.515, 0.615, and 1.08 eV below the conduction band, but these were not assigned to any particular defect levels [83]. A diagram of deep levels measured by Georgobiani is shown in Figure 2-21.

2.9.4.2 Extrinsic point defects

Much of the interest in defect levels in ZnS is related to interest in II-VI compounds for optoelectronic devices. Many of these efforts were attempts to increase the n- and p-type conductivity of extrinsically doped ZnS and other II-VI compounds [79, 81, 88-91]. Chlorine as an anion substitute in ZnS has been shown using photoconductivity to create a donor level 0.25 eV below the conduction band [92], which is significantly larger than the Cl donor level in ZnSe of 26 meV [89].

During ZnS:Cl single crystal growth, in addition to the Cl_S donor defect, ionized acceptor defects appear from a self compensation mechanism [83]. The induced compensating defects are normally V_{Zn} and it is thought that besides the isolated vacancies, V_{Zn}-Cl_S complexes exist [82-84]. This type of complex is known as an A-center, and was first postulated for ZnS in 1956 by Prener and Williams [80]. There is some disagreement in the literature as to the energy levels of these complexes. Vlasenko et al. observed a mid-gap defect 1.8 eV below the conduction band, which they attributed to a V_{Zn}-Cl_S complex [84]. A value of 0.95 eV is given by Neumark [80]. To the contrary, Georgobiani et al. attributed an acceptor level just 0.44 eV above the valence band to the V_{Zn}-Cl_S complex [83]. The interpretation by Georgobiani et al. seems more reasonable for several reasons. First, there is general agreement that the doubly ionized V_{Zn}^{2+} lies ~1.0-1.1 eV above the valence band. A defect level 0.55-0.6 eV above the valence band was assigned by Vlasenko to singly ionized V_{Zn}^{+}. It was assigned to an observed level 0.2 above the valence band by Georgobiani in agreement with the known relation that $E_{VZn}^{2+} = 5E_{VZn}^{+}$. In either case it would be surprising that a singly ionized V_{Zn}-Cl_S complex would lie deeper than the doubly ionized V_{Zn}^{2+}. To support this idea, the compensation mechanism for ZnSe:N has been attributed to a singly ionized V_{Se}-Zn-N_{Se} complex with a shallow donor level of 44 meV [88]. Another piece of evidence supporting the results of Georgobiani is that the V_{Zn}-Cl_S complex in ZnSe is assigned to be just 0.35 eV above the valence band [80]. One possible explanation for the discrepancy is that the defect level ~0.3 eV above the valence band found by Vlasenko and attributed to Mn_{Zn}^{0} is actually the singly ionized V_{Zn}^{+}, while the level 0.55 eV from the valence band and assigned to singly ionized V_{Zn}^{+} is actually the V_{Zn}-Cl_S complex.

Little has been reported regarding the defect levels of extrinsic acceptors in ZnS, as this material has been found experimentally to be not p-dopable [90].

2.9.5 Alkali Halide Doping of ZnS:Mn ACTFEL Devices

Combining ZnS phosphors with alkali metals and/or halide cations has been known for some time, primarily for the fluxing action of the low melting primary and secondary phases that can form [93, 94]. Reports on the electrical and optical impact of defect levels in ZnS due to alkali halide dopants is primarily with regard to optoelectronic diodes, as discussed in the previous section. Little work has been done in an effort to include alkali halide dopants in ZnS:Mn ACTFEL devices. This is primarily due to the belief that inclusion of Cl from the ALE precursors has a negative impact on device stability [76].

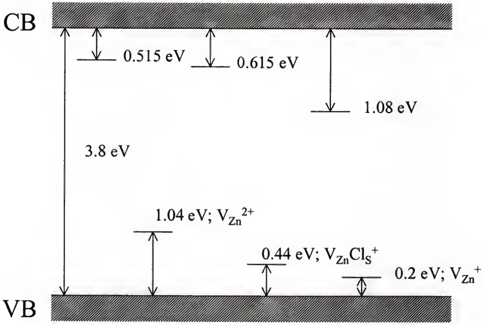

Figure 2-21. Energy band diagram with deep defect levels in ZnS:Cl [83].

One early study by Kun et al. reports a dramatic improvement of ZnS:Mn ACTFEL device brightness and efficiency with the incorporation of Cl into the films [95]. The films are deposited by e-beam evaporation. With as much as 8.4 at.% Cl added to the starting material as NH_4Cl none was detected in the evaporation pellets after firing or in the deposited films, indicating <0.01 at.% Cl present. After deposition of the phosphor layer the films were vacuum annealed at 500°C for two hours. The brightness and efficiency of the devices were shown to improve by as much as a factor of 3 with the inclusion of Cl, but the best device efficiency was just 0.6 lm/W. The improvement is attributed to improved crystallinity, measured by x-ray diffraction.

Codoping of sputter deposited ZnS:Mn ACTFEL devices with KCl was studied by Zhai and Waldrip [77, 96]. The procedure for codoping the phosphor layer will not be discussed here because it is the same procedure used in this work and described in detail in Section 3.2. The results of the codoping study are summarized here. With KCl codoping, the grain size increased from 132 to 187 nm after annealing at 700°C for 5 minutes as compared to undoped samples with the same annealing conditions. With grain growth there was no significant reduction in defect density. One significant change in the microstructure was observed. The small, equiaxed, highly defective grains at the nucleation surface were consumed by the columnar grains, which extended from the bulk to the nucleation surface with KCl codoping and 700°C annealing. It was shown that there is no preferential segregation of K to grain boundaries, and that the diffusion rate for K is much higher than that of Cl. The incorporation of KCl also was shown to stabilize the cubic phase, particularly with a (200) texture. These observations were used to conclude that K was incorporated at least partially as an interstitial in the cubic ZnS lattice. EL performance was dramatically improved with KCl codoping/annealing, and the stability of the devices were improved. The details of this improvement are discussed in detail in Chapter 3.

2.10 Oxide Phosphors for ACTFEL Displays

2.10.1 General Considerations

The most widely used phosphor host materials in ACTFEL devices are sulfur-based compounds [3, 5]. The requirements for the phosphor layer in ACTFEL devices were discussed in Section 2.7.5. Among these requirements, the need for efficient transport of high energy electrons and the need for good crystallinity have limited the interest in oxides as potential EL phosphors [3]. Empirically, oxides have larger band gaps than sulfides and are not as capable of transporting significant current densities of hot electrons [3]. Efficient host materials for ACTFEL phosphors are generally limited to those materials with band gap energies in the range of 3.5-4.5 eV. Oxides tend to be more refractory than sulfides and achieving good crystallinity at processing temperatures compatible with glass substrates (~550°C) is difficult or impossible with many oxide phosphors. For example, oxide-based CRT phosphors are usually processed above 1000°C [3, 93].

Renewed interest in oxide ACTFEL phosphors has stemmed from progress made in alleviating both of these limitations. In terms of the current transport, much recent work in oxide phosphors has been focused on materials with moderate band gaps such as Ga_2O_3 (4.52-4.84 eV [97, 98]), $ZnGa_2O_4$ (~4.3 eV [99]), and Zn_2GeO_4:Mn (4.68 eV, reported in this work). However information regarding the electrical behavior of these materials in ACTFEL devices is very limited.

With regard to the temperatures required to achieve good crystallinity, the approach taken by Minami and Kitai has been to use a refractory substrate material that allows high temperature annealing of the oxide phosphor layer to achieve good crystallinity [20, 100]. The device structure is the inverted structure shown in Figure 2-1b, and the substrate material is usually a $BaTiO_3$ sheet. This sheet is usually ~0.2 mm thick, and can be made by a cold press or doctor blade method [20]. The $BaTiO_3$ sheet serves as both mechanical substrate and bottom dielectric. One implication of the thick dielectric is that despite the large dielectric constant of $BaTiO_3$ (ε_r~5000) the thickness of the dielectric results in a capacitance that is ~4x smaller than that of a 200 nm $BaTa_2O_6$

film (ε_r~22). As discussed in Section 2.8 the smaller insulator capacitance results in a larger portion of the voltage being dropped across the dielectric layer rather than the phosphor. This requires a higher operating voltage and applies a larger strain on the breakdown strength of the dielectric layer. Further effects of the thick dielectric on the electrical behavior of the devices are not known because little has been reported on the subject.

2.10.2 Oxide Phosphors in ACTFEL Devices

Numerous oxide-based phosphor materials have been investigated, and a summary of some of the results is given in Table 2-9. In particular, more extensive reports have been given regarding Ga_2O_3:Mn,Cr,Eu, $ZnGa_2O_4$:Mn,Cr, $CaGa_2O_4$:Mn, $MgGa_2O_4$:Mn, Zn_2SiO_4:Mn,Ti,Tm, $Zn_2Si_xGe_{1-x}O_4$:Mn, and Y_2SiO_5:Ce [20, 21, 101-117]. One difficulty in searching for useful device values in the literature comes from the different device structure and reporting standards often used for the oxide phosphor based devices as compared to the standard structure devices. While the brightness and efficiency 40 V above threshold (B_{40}, E_{40}) with a 60Hz drive frequency is a standard way of reporting device performance for standard devices, maximum brightness and efficien7cy (B_{max} or L_{max}, E_{max}) are often reported for the oxide devices, often with a drive frequency of 1 kHz. The maximum brightness and luminance values are often achieved several hundred volts above threshold.

As seen in Table 2-9, many investigations of oxide-based ACTFEL devices have found poor performance, presumably from the large band gaps of the phosphor materials, such as 5.4 eV for Zn_2SiO_4:Mn and 5.6 eV for Y_2SiO_5 [48]. Another interpretation is inefficient charge injection. For example in one study no emission was observed from

Y2O2S:Tm, YF_3:Tm, or CaF_2:Eu devices without a barrier layer of ZnS or ZnF_2 [118]. But several phosphor materials including Ga_2O_3:Mn, Ga_2O_3:Eu, $ZnGa_2O_4$:Mn, $CaGa_2O_4$:Mn, Zn_2SiO_4:Mn, and $Zn_2Si_xGe_{1-x}O_4$:Mn exhibited good brightness values in the thick-film dielectric arrangement.

2.10.3 Zn_2GeO_4:Mn ACTFEL Devices

Several studies have been performed regarding Zn_2GeO_4:Mn or $Zn_2Si_{1-x}Ge_xO_4$:Mn as an ACTFEL phosphor [21, 48, 100, 101, 119, 120]. Zn_2GeO_4:Mn has been known for a long time as an efficient green-emitting phosphor [93], and was investigated for TFEL devices more recently due to the lower processing temperature required relative to Zn_2SiO_4:Mn [21, 101]. The crystallization temperature for Zn_2SiO_4:Mn is reported to be 900-1000°C whereas that for Zn_2GeO_4:Mn is 650-700°C [21]. An alloy between Zn_2SiO_4:Mn and Zn_2GeO_4:Mn has been found to provide the best combination of high brightness and low processing temperatures [100]. Brightness and effienciency of 480 cd/m^2 and 0.75 lm/W were measured at 60 Hz for sputter deposited $Zn_2Si_{0.5}Ge_{0.5}O_4$:Mn(2%) annealed in vacuum at 720°C for 1 hour [21]. Brightness and efficiency of 2000 cd/m^2 and ~0.7 lm/W were found at 1kHz for $Zn_2Si_{0.75}Ge_{0.25}O_4$:Mn(1%) annealed in Ar for 0.5-1 hour at 910°C [101]. Both of these studies were performed using thick $BaTiO_3$ substrates in the inverted structure. A study by Keir showed lower values of brightness and efficiency using lower annealing temperatures and standard device structure. Keir also reported an extensive study

Table 2-9. Performance of ACTFEL devices using oxide phosphor materials [20].

Phosphor Material	V_{th}	L_{max} 1 kHz (60 Hz)	η_{max}	Color	CIE x	CIE y
$Zn_2Si_{0.75}Ge_{0.25}O_4$:Mn	170	4220(809)	0.75	Green	0.272	0.662
$Zn_2Si_{0.7}Ge_{0.3}O_4$:Mn	110	1751(206)	2.53	Green	0.271	0.671
Zn_2SiO_4:Mn	160	3020(230)	0.78	Green	0.251	0.697
$CaGa_2O_4$:Mn	150	2790(592)	0.25	Yellow	0.479	0.518
Ga_2O_3:Mn	110	1018(227)	1.7	Green	0.198	0.654
$ZnGa_2O_4$:Mn	155	758(235)	1.2	Green	0.082	0.676
Zn_2GeO_4:Mn	130	341(39)	0.25	Green	0.331	0.645
$BeGa_2O_4$:Mn	70	162	0.091	Green	0.121	0.720
$ZnGeO_3$:Mn	110	27	0.026	Green	0.263	0.683
$ZnAl_2O_4$:Mn	130	21	0.006	Green	0.150	0.708
$SrAl_2O_4$:Mn	100	18	0.001	Green	0.180	0.709
$MgGa_2O_4$:Mn	160	14	0.001	Green	0.109	0.612
$BaAl_2O_4$:Mn	80	12	0.006	Green	0.158	0.707
$SrGa_2O_4$:Mn	125	8.7	0.003	Green	0.127	0.542
Mg_2GeO_4:Mn	200	5.5	0.001	Red	0.516	0.463
$MgGeO_3$:Mn	260	14.6	0.004	Red	0.667	0.300
$CaGeO_3$:Mn	300	20.8	0.004	Red	0.514	0.377
$Ga_2Ge_2O_7$:Mn	200	135	0.03	Red	0.593	0.407
CaO:Mn	390	55	0.016	Red	0.603	0.391
GeO_2:Mn	180	7	0.018	Red	0.521	0.413
$ZnGa_2O_4$:Cr	250	196(6)	0.02	Red	0.584	0.398
Ga_2O_3:Cr	240	375(34)	0.04	Red	0.654	0.293
Zn_2SiO_4:Ti	280	15.8	0.017	Blue	0.142	0.115
CaO:Pb	470	5.5	0.001	Blue	0.166	0.113
$CaGa_2O_4$:Eu	225	215(19)	0.026	Red	0.687	0.311
Y_2O_3:Eu	130	144(27)	0.14	Red	0.573	0.393
$ZnGa_2O_4$:Eu	175	62	0.009	Red	0.584	0.398
Ga_2O_3:Eu*	100	(580)	0.37	Red	0.587	0.385
Zn_2SiO_4:Eu	210	5.5	0.001	Blue	0.208	0.236
$Sr_2P_2O_7$:Eu	145	5.6	0.005	White	0.334	0.270
$ZnGa_2O_4$:Tb	230	16	0.004	Green	0.296	0.669
$CaGa_2O_4$:Tb	230	16	0.002	Green	0.361	0.542
$CaGa_2O_4$:Dy	215	30	0.005	Yellow	0.479	0.518
$ZnGa_2O_4$:Tm	260	5.7	0.01	Green	0.125	0.585
Y_2SiO_5:Ce	235	13.2	0.054	Blue	0.176	0.138
Zn_2SiO_5:Ce	200	6.3	0.007	Blue	0.149	0.113

*[98]

attempting to incorporate various materials as fluxing agents. The conditions for each co-dopant were not optimized. The most promising flux agents from this study were determined to be NaF, KF, RbF, and NaCl. However it should be noted that one effect of these co-dopants was often a shift in the emission spectrum, and how much of the improved performance can be accounted for by this effect alone is not certain. Electrical measurements did show altered electrical properties due to the incorporation of co-dopants, so there are certainly changes other than just the spectrum [48]. The phosphor layer thickness is not reported, and phosphor fields measured using a Q-F_p analysis were in the range of 5 MV/cm. These devices were borderline field clamped, and showed a sluggish turn-on in the B-V characteristics.

Most recently Bondar et al. have reported a brightness of 48 cd/m^2 using the standard device structure[119]. Clark et al. reported a brightness value over 100 cd/m^2 at V_{40} and 60 Hz using the standard device structure. They also claim new method for obtaining crystalline Zn_2SiO_4 and Zn_2GeO_4 powders at temperatures as low as 125°C [120].

CHAPTER 3
ALKALI HALIDE CO-DOPING OF ACTFEL DEVICES

3.1 Introduction

This chapter describes the effects of alkali halide codoping of the ZnS:Mn phosphor layer on the electrical and optical properties of the RF magnetron sputtered ACTFEL devices. First, a description of the experimental procedure used in this study is given. This is followed by a summary of the results of electro-optical characterization of the devices. The results will show that the codoping procedure dramatically improves the brightness, efficiency, and stability of the devices compared to the best sputtered, undoped devices. The observed effects are then discussed in the context of the efficiencies of the various processes during device operation. It is shown that improved performance is due to increased excitation efficiency. The electrical behavior of the co-doped devices combined with previous microstructural analysis is used to attribute the improvement to less band bending, which is caused by a reduction in the traping efficiency of hole traps in the phosphor layer. Further arguments are given that the electron multiplication process becomes so efficient that the conduction current is limited by the internal phosphor resistance rather than a capacitance or density of states, as is normally seen.

3.2 Experimental Procedure

For the experiments described in this chapter traditional ZnS:Mn ACTFEL devices were fabricated by RF magnetron sputtering and an alkali halide co-dopant, usually KCl, was introduced via *ex-situ* diffusion during a post-deposition anneal. The device fabrication process flow is shown schematically in Figure 3-1, and the details are described in this section.

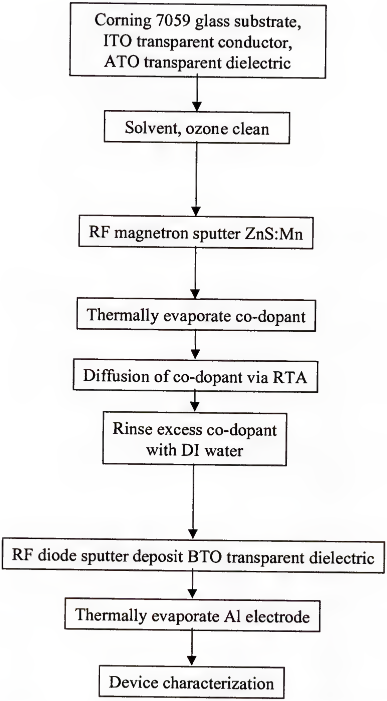
Corning 7059 glass substrate,
ITO transparent conductor,
ATO transparent dielectric
Solvent, ozone clean
RF magnetron sputter ZnS:Mn
Thermally evaporate co-dopant
Diffusion of co-dopant via RTA
Rinse excess co-dopant
with DI water
RF diode sputter deposit BTO transparent dielectric
Thermally evaporate Al electrode
Device characterization

Figure 3-1. Schematic process flow diagram for ZnS:Mn,K,Cl device fabrication.

3.2.1 Substrates

Alkali halide codoping experiments were performed using the standard ACTFEL device structure (Figure 2-1a). Codoping was achieved by *ex-situ*, or post-deposition diffusion of the alkali halide into the phosphor layer. The substrates were Corning 7059 glass coated with ITO. Unless otherwise noted, the bottom dielectric was Al_2O_3/TiO_2 (ATO) deposited using ALD by Planar Systems, Inc. For a small number of samples SiO_xN_y was used as the bottom insulator. Before phosphor layer deposition the substrates were cleaned with methanol followed by a 6 minute ozone clean.

3.2.2 Phosphor Layer Processing

The ZnS:Mn layer was deposited by RF magnetron sputtering using independent ZnS and Mn sources. The ZnS target was bulk polycrystalline ZnS purchased from Morton Thiokol, Inc., and the Mn was sputtered from a metallic Mn target purchased from Target Materials, Inc. Multiple substrates were placed on a rotating stage, which resulted in sequential sputtering of ZnS and Mn layers using a rotation rate of 4 revolutions/minute. The sputter chamber typically had a base pressure of 1×10^{-6} Torr.

Conditions for phosphor deposition were evaluated and optimized by measuring the brightness at 20V or 40V over threshold (B_{20} or B_{40}) of half-cell devices (as defined in section 2.4.1, these are devices with no top insulator). The processing conditions for the samples used in this study are as follows. The substrate temperature during sputter deposition of the phosphor layer was 160°C. The power applied to the 2" target was 150 W for ZnS and 15 W, 12% duty cycle for Mn. The sputter gas was Ar at 20 mTorr pressure. The resulting growth rate was typically ~ 0.52 nm/s. The sputter system allowed as many as seven 1"x2" substrates to be processed simultaneously, allowing various post-deposition processing conditions to be compared directly using identical phosphor films. One bare glass substrate was included in each run to calculate the film thickness by measuring the optical interference spectrum.

The alkali halide was subsequently deposited onto the ZnS:Mn phosphor by thermal evaporation. Typical base pressures for evaporation were 5×10^{-7} Torr, and a deposition rate of ~1.5 nm/s was typical. The KCl layer thicknesses were over the range 10-1000 nm, but the standard thickness was 100 nm. A control sample from the same sputter run without codopant, referred to here as "undoped", was always processed with the codoped sample.

The devices were then annealed under flowing Ar or N_2 in a custom quartz lamp-heated rapid thermal anneal (RTA) chamber. The sample was placed on a graphite susceptor that also had a graphite cover not in contact with the sample. A thermocouple was placed immediately adjacent to the sample to control temperature. A piece of polished Si wafer was placed polished side down on the sample during heating to help prevent contamination of/from the RTA chamber. In addition, different graphite susceptors were used for RTA of codoped and undoped samples, and the evaporation chamber was cleaned between different conditions to reduce cross-contamination by KCl. The standard processing conditions employed a 5 minute anneal at 700°C with a 2 minute ramp to temperature, and complete shutoff of the furnace during cooling, which allowed the sample to cool to < 500 °C in < 30 seconds.

Unless otherwise noted, most experiments used KCl as the co-dopant, however experiments using KBr, NaCl, and KI as the co-doping agent were performed. A brief summary of the results of these experiments are included in Appendix A. Unless otherwise noted, the standard processing conditions for other alkali halides employed a 5 minute anneal at 700°C.

After heat treatment, excess residual alkali halide was removed using deionized water. To ensure there were no deleterious effects from the deionized water rinse, unco-doped samples were also rinsed and tested.

3.2.3 Device Fabrication

The top insulator material on full stack devices was $BaTa_2O_6$ (BTO). This layer was 250 nm thick and was deposited on the phosphor layer by RF diode sputter deposition in a mixed Ar/O_2 (77%/23%) process gas ambient. Typical base pressures were 4×10^{-6} Torr.

The top electrode was formed via thermal evaporation of Al through a shadow mask. Typical base pressures for this process were 1×10^{-6} Torr. Contact to the bottom (ITO) electrode was achieved by scratching through the upper insulating layers with a diamond scribe and melting pure indium metal onto the scratched area, which wets to the ITO layer for electrical contact.

3.2.4 Measuring EL Performance

The primary measures of device performance, namely brightness, efficiency, and chromaticity, were routinely measured. The electrical excitation was provided by a high voltage driver that produced alternating polarity 60 Hz trapezoidal pulses with a 5 μsec rise time, 30 μsec dwell, and 1 μsec fall time. Brightness and chromaticity were measured as a function of voltage using either a Pritchard spectrophotometer, or a Pritchard-type spectrophotometer from Photo Research, model PR650. Efficiency values were calculated from the brightness values and the dissipated power, calculated from time-resolved values of current and voltage over a full period.

Device stability was studied by accelerated aging using the same high voltage driver operating at 2.5 kHz instead of 60 Hz. Aging was done at 40V above the 2.5 kHz threshold voltage and brightness vs. voltage behavior was measured periodically during aging. The V_{th} was determined using the maximum slope intercept method, which was discussed above in Section 2.5.1.1.

3.2.5 Electrical and Optical Characterization

The electrical and optical properties were evaluated for a number of devices. Q-V, Q_{int}-F_p, and C-V plots were measured using a Sawyer-Tower bridge and either a 100 nF capacitor or 100 Ω resistor as the sense element to measure either the stored charge or the current, respectively, using a Tektronix TDS 510A digitizing oscilloscope. Luminance versus time (L(t)) data were collected on the oscilloscope from an Si-diode photomultiplier tube (PMT) manufactured by Oriel with a 1 kΩ bridge resistor. The sample was placed over an aperture on a 4" integrating sphere, which was then coupled into the PMT.

Optical scattering was measured using a standard diffuse reflectance technique. This employed a W-halogen lamp as the light source. The light source was coupled into a bifurcated optical fiber which was placed at a 45° angle to the sample surface. The second fiber collected diffusely reflected light and coupled into a CCD array spectrometer, Ocean Optics model P2000. The intensity of the backscattered light versus wavelength was measured relative to that for a $BaSO_4$ reflection standard, and the average diffuse reflectance over the visible range was recorded.

3.3 Results

Optical and electrical electroluminescent device properties are given for full stack samples processed with and without KCl co-doping, as described in section 3.2.

3.3.1 EL Performance

The primary measures of the performance of an ACTFEL device include brightness, efficiency, chromaticity, and stability. In terms of the brightness and efficiency, the addition of alkali halide co-dopants to ZnS:Mn ACTFEL devices during post-deposition annealing provides a dramatic improvement in device performance over the best sputtered ZnS:Mn devices, and even those grown by ALE or evaporation. Figure 3-2 shows the brightness and efficiency vs. voltage characteristics for the best devices with and without KCl co-doping; these samples were taken from the same ZnS:Mn sputter run. The B_{40} values were 581 cd/m^2 and 379 cd/m^2 for the KCl doped and undoped devices, with E_{40} values of 1.92 lum/W and 1.18 lum/W, respectively. To put the brightness values in perspective, they are compared in Figure 3-3 to the typical values obtained from optimized ALE and evaporated devices [121].

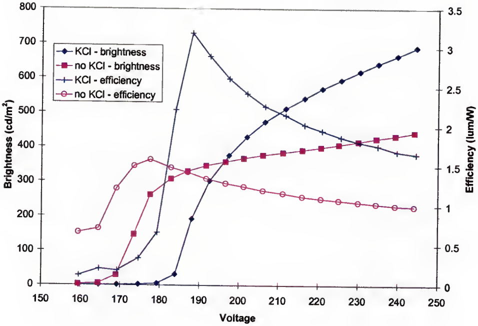

Figure 3-2. Brightness and efficiency vs. voltage for ZnS:Mn devices with and without KCl co-doping.

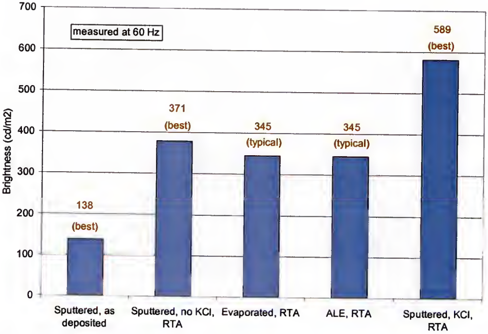

Figure 3-3. Comparison of B_{40} brightness values for as deposited, annealed, and KCl doped sputtered devices, and evaporated and ALE-grown devices.

The magnitude of improvement for these samples was a 53% improvement in B_{40} and a 62% improvement in E_{40}. B-V and E-V curves from within a ZnS:Mn run, but with varying thicknesses of KCl for diffusion are shown in Figure 3-4a and b. Comparing the five co-doped samples from that sputter deposition run to the two undoped samples from the same run, all plotted in Figure 3-4, yields an average 53% increase in brightness and an average 37% increase in efficiency. The average brightness and efficiency of the undoped samples is 103 cd/m^2 and 1.23 lum/W, respectively, with a standard deviation of 13 cd/m^2 and 0.17 lum/W. The values for the KCl doped samples are 157 cd/m^2 and 1.68 lum/W, with a standard deviation of 11 cd/m^2 and 0.07 lum/W. The average threshold voltage also increased from 168 V unco-doped to 184 V co-doped, with standard deviations of 0.3 and 2.6 V, respectively. While the specific values for threshold voltage vary from run to run, the increase was observed consistently with added KCl.

Data on the B-V and E-V performance of devices from different deposition runs are given in Figure 3-5. The run-to-run repeatability is reasonable, and the intra-run repeatability is even better. These samples were annealed at 650°C for 2 minutes with no co-dopant, and therefore the performance values cannot be compared in magnitude to the undoped samples in Figure 3-5. The B_{40} and E_{40} values have an average of 142 cd/m^2 and 0.771 lum/W, respectively. The intra-run standard deviations for these values are 4.8 cd/m^2 and 0.054 lum/W, while the standard deviations between runs are 6.4 cd/m^2 and 0.080 lum/W.

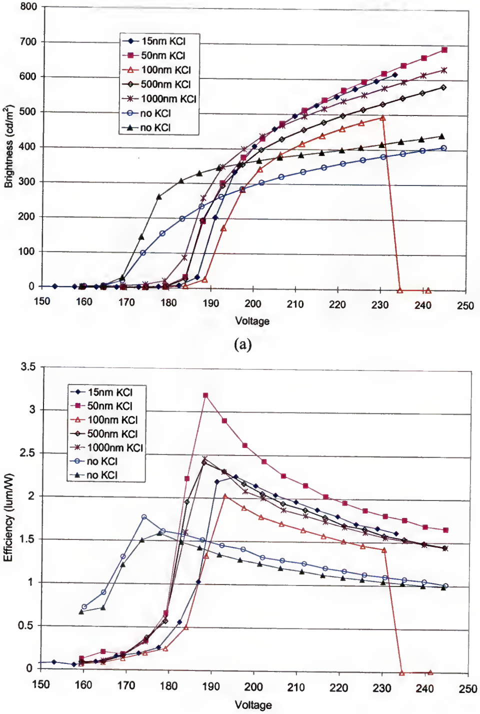

(a)

(b)

Figure 3-4. (a) Brightness (b) and efficiency vs. voltage curves for samples from the same ZnS:Mn sputter run using varying thicknesses of KCl.

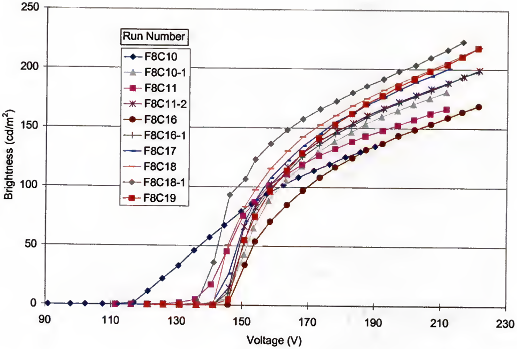

(a)

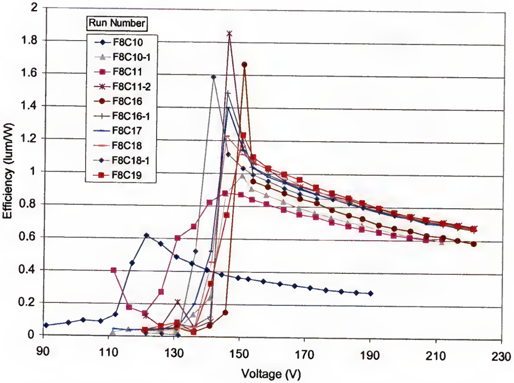

(b)

Figure 3-5. (a) Brightness (b) and efficiency vs. voltage curves for different ZnS:Mn sputter deposition runs using identical conditions, annealed at 650°C for 2 minutes.

EL emission spectra for samples with and without KCl are shown in Figure 3-6. The small differences in these emission spectra varied somewhat for each sample. They were shown to result from thin film interference fringes, since their wavelength and magnitude change as the viewing angle is changed. Note that both the high energy and low energy tails of the spectra match quite closely. In short, there was no systematic shift of the emission spectrum or CIE coordinates with KCl co-doping.

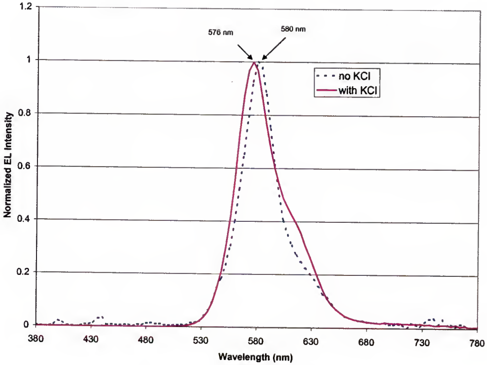

Figure 3-6. EL emission spectra for ZnS:Mn samples with and without KCl doping.

3.3.2 Optical Properties

Normalized PL decay behavior is shown in Figure 3-7 for as-deposited, 700°C annealed, and 700°C annealed/KCl codoped samples. Figures 3-8 and 3-9 show the EL emission decay data at threshold or 40V above threshold, 60 Hz for both polarities from

KCl doped and undoped samples. The decay behavior under the same conditions is shown in more detail in Figure 3-10.

The PL decay data in Figure 3-7 shows identical decay behavior for as-deposited, annealed, and KCl codoped/annealed samples. The best fit curve in Figure 3-7 shows that the decay follows the form $B = B_o\exp-(t/\tau)^\alpha$. The decay time, ~45 μs, is unusually fast for Mn^{2+} decay, and the cause is unknown. However it is clear that KCl codoping did not change the radiative relaxation time constant.

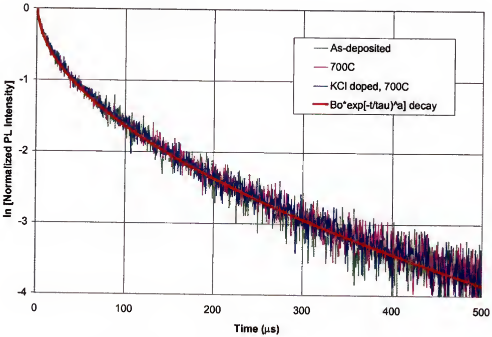

Figure 3-7. PL decay curves for as-deposited, 700°C annealed, and 700°C annealed/KCl co-doped samples.

The EL decay data in Figure 3-8 is shown to compare the relative intensities of the two different polarities of voltage pulses used to excite EL. The undoped sample shows very symmetric emission between the two pulses. For comparison, ALD-grown devices normally show more intense emission when the top surface acts as the cathode

[122], while electron-beam evaporated samples show higher emission from the nucleation surface as the cathode [123]. Unlike the undoped sample, the KCl doped sample shows 14% higher initial intensity for the ZnS/ATO interface as cathode than for the ZnS/BTO cathodic interface.

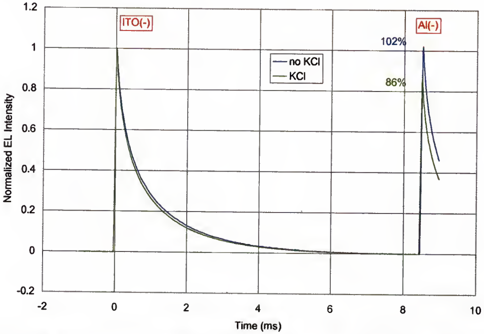

Figure 3-8. EL emission decay at 40V above threshold, 60Hz, for KCl doped and undoped ZnS:Mn samples. Both curves are normalized to the maximum intensity when the ZnS/ATO interface is the cathode ($t \approx 0$).

The radiative efficiency for different samples or conditions can be compared by measuring the EL decay behavior when excited by voltage pulses much shorter than the decay time [45]. With some approximations, when the decay is normalized to its maximum value, the integrated intensity is equal to the relative radiative efficiency. The EL decay data in Figure 3-9 show similar decay behavior for all conditions and polarities. The decay is normalized to the maximum intensity for both polarities of undoped and KCl codoped ZnS:Mn devices at 40V above threshold. In addition the decay of an undoped device at threshold is also shown. In all cases the decay is not described accurately by exponential decay, power law decay, or a combination of the two. There is a small and repeatable difference between the respective decay curves. The relative value of the integrated intensity for each normalized curve is an indication of radiative efficiency, since the duration of excitation (~40 μs) is much shorter than the decay time (~2 ms). The relative radiative efficiencies are given in Table 3-1, which shows that the highest efficiency is for the device at threshold, and that the lowest efficiencies are from the KCl codoped devices. The average KCl codoped intensity is just 4% lower than for the undoped sample at 40V above threshold.

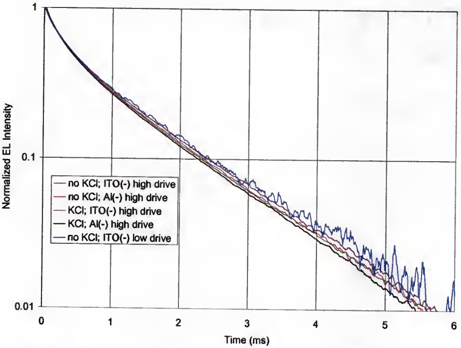

Figure 3-9. EL emission decay at 40V above threshold (high drive), 60Hz, for KCl doped and undoped ZnS:Mn samples. Both positive and negative polarity pulses are normalized to their maximum intensity. Also included is the EL emission decay for the ITO(-) pulse of the undoped sample at the threshold voltage (low drive).

Table 3-1. Relative luminous efficiencies for KCl codoped and undoped devices at 40V above threshold compared to an undoped device driven at threshold.

Device	Polarity	Relative Luminous Efficiency (%)
KCl	Al (-)	91
	ITO (-)	93
No KCl	Al (-)	94
	ITO (-)	97
No KCl (at V_{th})	ITO (-)	100

Figure 3-10 shows the luminescent decay data for the same samples and conditions on a shorter time scale. These data are normalized to unity when the excitation voltage is removed and reaches zero (t ~ 32 μs). These data show the increased excitation rate for the KCl codoped sample during the early portion of the voltage pulse, which accounts for the difference in radiative efficiency. For the sake of comparison, the relative initial intensity, B_o, is given for each curve in Figure 3-10.

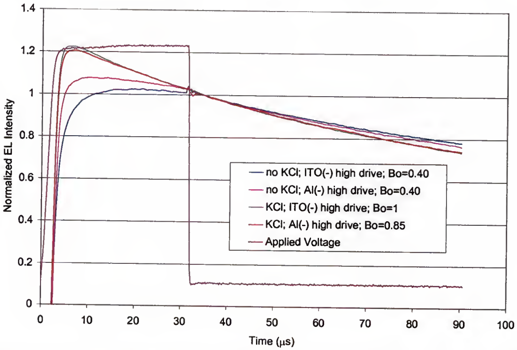

Figure 3-10. EL emission decay at 40V above threshold, 60Hz, for both polarities of KCl doped and undoped ZnS:Mn devices. The data are normalized to their maximum intensity as the voltage reaches zero (t ~ 32 μs). B_o refers to the relative initial intensity for each curve.

The values of diffuse reflectance after different RTA temperatures for either ATO or SiON as the bottom insulator are shown in Figure 3-11. These data show that the diffuse reflectance is low (≈10%), is slightly dependent on the type of bottom insulator used, and that for an ATO insulator (which was used for this study) the diffuse reflectance actually decreases slightly when KCl is added.

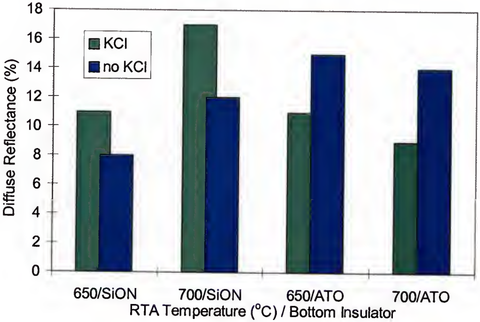

Figure 3-11. Diffuse reflectance values for KCl doped and undoped ZnS:Mn samples annealed at either 650 or 700°C using either SiON or ATO as the bottom insulator.

3.3.3 Electrical Measurements

Neglecting the additional dissipative process of luminescence, an ACTFEL device is essentially a two-terminal electrical device. The transport properties of an ACTFEL device are often most easily studied by investigating the time resolved electrical behavior of the device, sometimes in conjunction with studying the time resolved emissive characteristics. The significance and procedure for measuring the following electrical data were discussed in more detail in Section 2.8.

The Q-V plots in Figure 3-12 show the external charge on the y-axis versus the applied voltage on the x-axis. Data are shown in Figure 3-12 for as-deposited, 700°C annealed, and 700°C annealed/KCl codoped samples. They were measured at 40V above threshold using a 100 nF capacitor as the sense element. The corresponding Q_{int}-F_p plots, which refer to the conduction charge versus phosphor field, are shown in Figure 3-13.

The Q-V data in Figure 3-12 show some interesting characteristics. The most obvious differences are that (1) the amount of leakage charge differs between all of the samples, (2) the amount of total external charge is smaller for the as-deposited device, (3) the annealed, no-KCl sample shows an unusual two-step breakdown for both polarities at low voltage (~35-40 V), and (4) the KCl/annealed sample shows significant bending of the above threshold portion of the curve and shows a large amount of relaxation charge.

To analyze these features in more detail it is sometimes easier to use the Q_{int}-F_p plot shown in Figure 3-13. Figures 2-11 and 2-14 are repeated here for convenience as well. The dielectric constants for the layers are used as parameters in this analysis to obtain the most "ideal" shape for the curve, i.e., the most horizontal behavior during the D-E and I-J portions of the plot, and the most vertical behavior during the B-C and G-H portions of the curve. In this case the values used for the phosphor capacitance were11.5, 12, and 11 nF/cm^2 for the as-deposited, annealed, and KCl/annealed samples, respectively. These compare closely to 10.5 nF/cm^2 for the physical capacitance, calculated from the known dielectric constant and measured film thickness. The insulator capacitance values were 43, 38, 45, and 30 nF/cm^2 for the as-deposited, annealed, and KCl/annealed, and physical values, respectively. The as-deposited sample

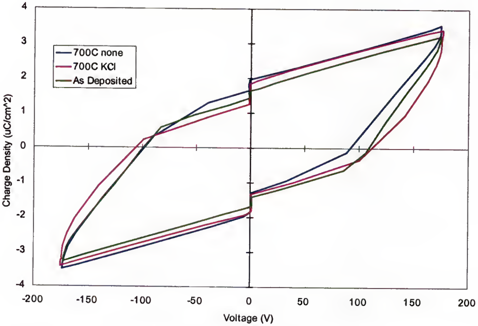

Figure 3-12. External charge-applied voltage (Q-V) plots for as-deposited, annealed, and annealed/co-doped ZnS:Mn samples.

clearly shows the lowest amount of conduction charge and the smallest amount of leakage charge at moderate phosphor fields. The annealed sample shows the largest conduction charge with asymmetric characteristics. Specifically, the leakage charge is smaller after the ITO (-) pulse, and the leakage charge is larger for the Al (-) pulse, while the conduction charge is similar for the two polarities. The phosphor fields are smaller for the annealed device than either of the other two. For the KCl-doped sample, the leakage charge is large and symmetric between the two polarities, and the breakdown field is larger than for the other two samples. In addition, the vertical portions of the curve are not constant.

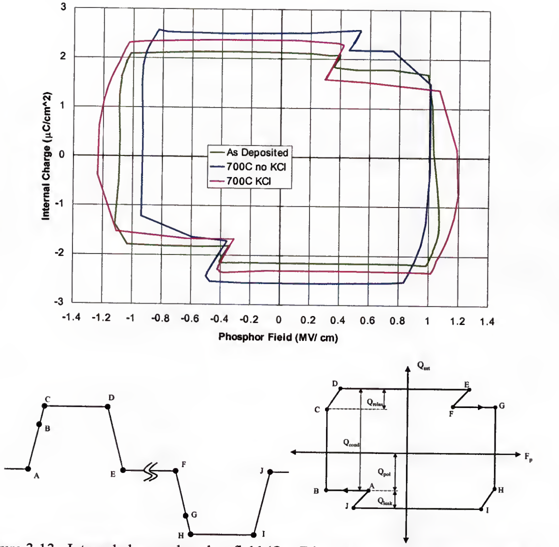

Figure 3-13. Internal charge-phosphor field (Q_{int}-F_p) plots for as-deposited, annealed, and annealed/co-doped ZnS:Mn samples. A positive field polarity refers to the ZnS/BTO interface as cathode. Figures 2-11 and 2-14, which illustrate the applied voltage waveform and corresponding Q-F_p plot are repeated for convenience.

Capacitance-voltage (C-V) plots were generated for a range of maximum voltages for both KCl-doped and undoped ZnS:Mn devices. The results are shown in Figure 3-14a and 14b for the KCl doped and undoped devices, respectively. The first characteristic to note for both plots is the rigid shift of turn-on voltage to lower values as

V_{max} increases. One interpretation of this behavior has been that the electrons are sourced from interface states, rather than the phosphor bulk [23]. Second, the capacitance values above turn-on are larger for the KCl doped device. Finally, the capacitance above turn-on for the KCl codoped device shows a linear upward slope which extrapolates back to the origin.

From the same measurements from which the C-V data were obtained, data were collected to investigate the maximum brightness, B_{max}, and internal or conduction charge, Q_{int}, as a function of voltage. These measurements were performed using short voltage pulses which had a 5 μs rise time, 5 μs dwell, and ~1 μs fall time. Transferred charge was determined using the Sawyer Tower bridge arrangement with a 100 Ω sense resistor. The current versus time data were integrated to obtain Q(t) for each polarity, and an example is shown in Figure 3-15. The internal charge was assumed to be the stored charge when the applied voltage reached a value of 0 V at the end of the pulse, which assumes that the rapid charge relaxation at the end of the voltage pulse is simply discharging the device capacitance. This routine is shown schematically in Figure 3-15.

The maximum brightness was measured simultaneously by recording the time-dependent EL emission, L(t). Due to voltage oscillations from the high voltages and ramp rates, it was necessary to extrapolate the L(t) back to its maximum value. This extrapolation could be done linearly due to the short time scales involved ($\sim 10^{-5}$ s) relative to the long decay time of the phosphor ($\sim 10^{-3}$ s). This is shown schematically in Figure 3-16.

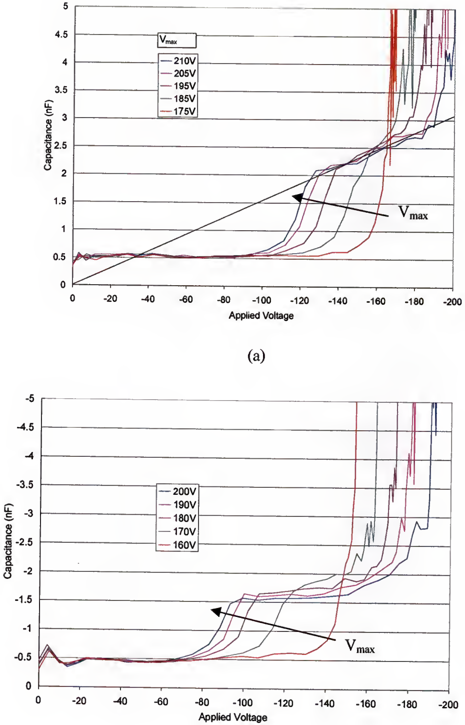

(a)

(b)

Figure 3-14. Capacitance vs. voltage curves for (a) KCl codoped and (b) undoped samples at various maximum applied voltages.

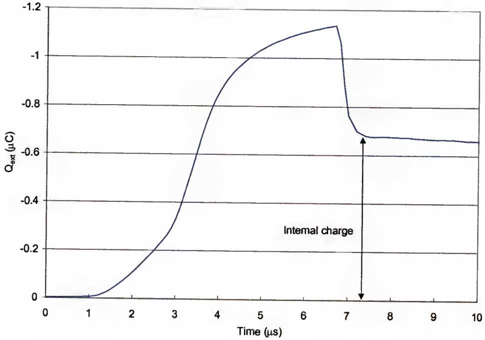

Figure 3-15. Determination of internal charge from Q_{ext} vs. t analysis.

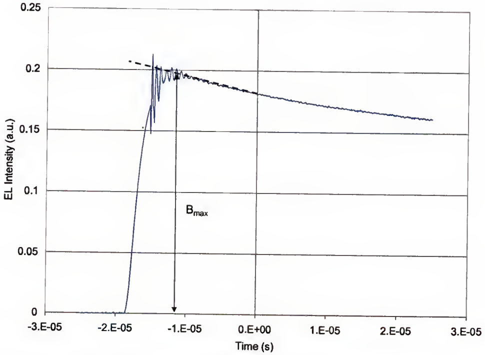

Figure 3-16. Determination of B_{max} from L(t) data. Note the necessary extrapolation back to the end of the voltage pulse which was necessary because of "ringing" as discussed in the text.

The values of B_{max} divided by Q_{int} at different voltages were determined as a function of voltage and Q_{int} for both voltage polarities. The results for KCl codoped and undoped samples are shown in Figure 3-17 as a function of voltage, and in semilog format in Figure 3-18 as a function of Q_{int}.

Several observation can be made based on the data in Figures 3-17 and 3-18. First, the excitation efficiency is 26% higher when the ATO/ZnS interface is the cathode both with and without KCl doping. Second, the excitation efficiency is ~75% higher for the KCl doped sample than for the undoped sample for both polarities.

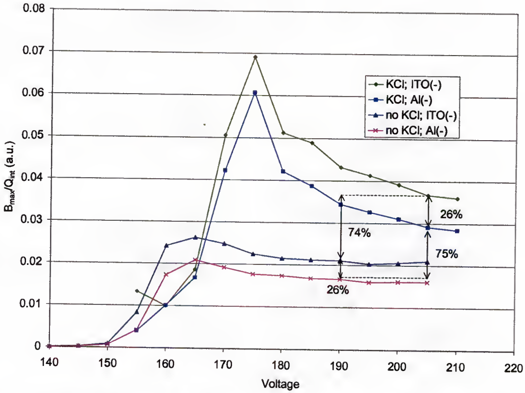

Figure 3-17. B_{max}/Q_{int} vs. applied voltage for both polarities of KCl codoped and undoped ZnS:Mn samples.

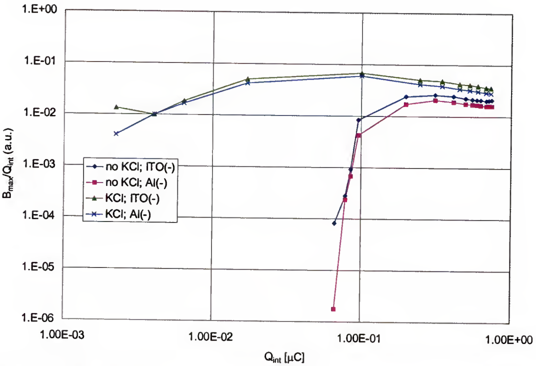

Figure 3-18. B_{max}/Q_{int} vs. Q_{int} for both polarities of KCl codoped and undoped ZnS:Mn samples.

Additional information from the above data is the behavior of Q_{max} as a function of V_{max}. These data are shown in Figure 3-19. Values for Q^e_{max}, or the external transferred charge are taken directly from the $Q^e(t)$ data, as are the values for V_{max}. From these data, the subthreshold insulator capacitance is subtracted leaving a plot of the internal charge vs. maximum applied voltage. Several features are worth noting from Figure 3-19. First, the undoped sample shows a large amount of overshoot, defined here as the large slope portion which saturates to a lower slope and has a value of 6.8 nF. The KCl doped sample on the other hand shows a higher turn-on voltage and less overshoot, but a much steeper slope corresponding to a capacitance of 16.6 nF. For the sake of comparison, a transferred charge capacitance plot from an evaporated ZnS:Mn device is shown in Figure 3-20. This device shows less overshoot at threshold than the sputtered, undoped device, but saturates to the insulator capacitance at higher voltages similar to the undoped sputtered device.

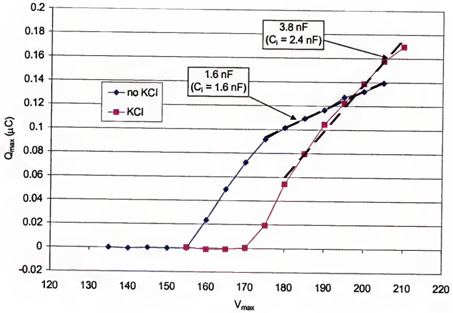

Figure 3-19. Q_{max} vs. V_{max} for KCl codoped and undoped ZnS:Mn samples.

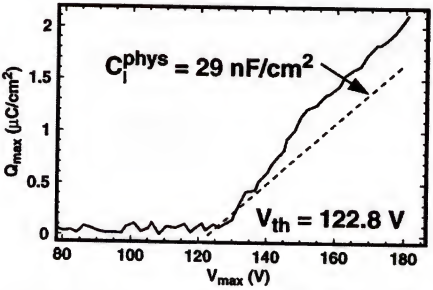

Figure 3-20. Q_{max} vs. V_{max} for an evaporated ZnS:Mn device [23].

3.3.4 Aging Measurements

Devices with and without KCl codoping were subjected to accelerated aging at 2.5 kHz using the standard 40 μs voltage pulse. The aging voltage was 40 V above the 2.5 kHz threshold voltage. The brightness-voltage behavior was measured periodically during aging. The results for (a) undoped and (b) KCl codoped devices are shown in Figure 3-21. These data show that the aging behavior is very similar for the two devices, primarily exhibiting a "p-shift" or an increasing threshold voltage. However for the KCl doped samples this shift is much less severe.

3.4 Discussion

It was mentioned previously that the primary measures of ACTFEL device performance are brightness, efficiency, chromaticity, and stability. The data in Figures 3-2 to 3-4 show that the diffusion of KCl into the phosphor layer during post deposition annealing of sputtered ZnS:Mn devices dramatically improves the EL performance in terms of brightness and efficiency. Specifically, the brightness improves 53% on average with a 37% increase in efficiency, and these values are 53% and 62% respectively for the best device. Figure 3-6 shows that there is no change in chromaticity with KCl doping. In addition, it is clear from Figure 3-21 that the inclusion of this co-dopant also improves the stability of the device over time.

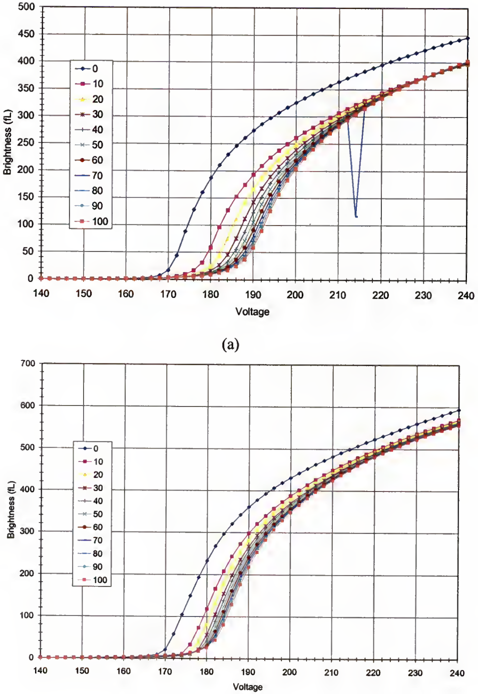

(a)

(b)

Figure 3-21. Brightness vs. voltage curves after 10 hour aging intervals for (a) undoped (b) and KCl co-doped ZnS:Mn devices.

The goal is then to determine the fundamental source of this improved performance. Based on the modified microstructure in these devices observed by Zhai, in addition to the role of alkali halide dopants in ZnS presented by Waldrip [96] and the explanations therein regarding modified microstructure and donor doping, several potential mechanisms for increased performance must be discussed:

- increased conduction charge
- improved optical outcoupling
- improved radiative relaxation efficiency
- improved excitation efficiency
- more efficient charge injection due to a modified phosphor/insulator interface
- modified band bending due to carrier trapping, ionization of the lattice, impurity atoms, or defects, or the lack thereof
- reduced scattering of ballistic electrons by defects due to improved microstructure

Even though device stability is not the focus of this work, it is important that the change in aging behavior be consistent with, or at least not contradict, the mechanisms determined to alter the device behavior.

3.4.1 Effects of Conduction Charge on Device Performance

One of the obvious issues to consider for a brighter device, especially when the interfacial microstructure is significantly changed, the grain size is larger [77], and known donor impurities are added to the host, is whether the amount of conduction charge has increased. Figure 3-14 shows the behavior of internal or conduction charge with the phosphor field, and conduction charge decreases slightly rather than increasing. However, this type of plot can be misleading for the purpose of comparing conduction charge since (1) the conduction charge is related to the voltage relative to threshold, which is usually not the same for different samples, and (2) the capacitance values are adjusted for "ideal" Q-F_p characteristics and this affects the magnitude of calculated conduction charge. For this analysis it is more reliable to use the Q-V data in Figure 3-13, which upon careful inspection, show nearly identical amounts of conduction charge. For some other samples, the measured conduction charge was slightly (≈ 20%) larger for KCl codoped samples.

It is also important to consider the experimental factors in measuring this data. For example, information regarding conduction charge can be drawn from Figure 3-19, which shows the relationship between Q^{int}_{max} and V_{max} for a different set of samples. From these data, at 40V above the electrical threshold there is a 35% increase in the amount of conduction charge. However the larger slope for the KCl doped samples shows how a careful selection of applied voltage is necessary to draw specific conclusions for a set of samples using only Q^{int}-F_p data.

The most important point to consider is that while increased conduction charge would be expected to result in a corresponding increase in brightness, it would not explain an increase in efficiency since the dissipated power would increase concomitantly. From these observations, it can be concluded that increased conduction charge would explain why for some samples the increase in brightness is larger than the corresponding increase in efficiency, such as the samples for which data are shown in Figure 3-4. However there must be other factors causing the observed increase in device efficiency.

3.4.2 ACTFEL Device Efficiency

From the previous section it is clear that it is important to note the concomitant increase in both brightness and efficiency, which are very similar in magnitude for the best samples. The similar magnitude of improved performance in terms of both brightness and efficiency suggests that the underlying cause for the improved behavior is an increased efficiency in some aspect of device operation, resulting in a corresponding improvement in brightness, assuming similar drive characteristics and dissipative charge.

Therefore a more detailed discussion of device efficiency is warranted. It is easier to consider the device efficiency by separating and considering individually the important aspects of device operation. Following closely the approach taken by Mach and Mueller [42] the most useful definition for device efficiency in terms of analyzing device processes is of the form

$$\eta = \frac{\text{photon flux}\left[\dfrac{\text{photons}}{\text{cm}^2\text{s}}\right]}{\text{transferred charge}\left[\dfrac{\text{electrons}}{\text{cm}^2 s}\right]}. \tag{3.1}$$

It is useful to further break this term up into components, namely

$$\eta = \eta_{exc}\eta_{lum}\eta_{opt} \tag{3.2}$$

with each term related to the primary processes involved in ACTFEL device operation. More specifically, η_{exc} is the efficiency of the excitation of luminescent centers by charge carriers, or

$$\eta_{exc} = \frac{\text{centers excited}\,[\text{cm}^{-3}]}{\text{electrons transferred}\,[\text{cm}^{-2}]}, \tag{3.3}$$

η_{lum} is the radiative efficiency of excited centers, or

$$\eta_{lum} = \frac{\text{centers decaying radiatively [cm}^{-3}\text{]}}{\text{centers excited [cm}^{-3}\text{]}}, \tag{3.4}$$

and η_{opt} is the outcoupling efficiency of the emitted photons out of the device, or

$$\eta_{lum} = \frac{\text{photons emitted through the surface [cm}^{-2}\text{]}}{\text{photons generated within the device [cm}^{-3}\text{]}}. \tag{3.5}$$

Each of these terms can be discussed with respect to the possible mechanisms for increased brightness and/or efficiency in the devices. Note that both η_{exc} and η_{opt} are related to the device length. This could complicate matters when there is a significant change in the device thickness and uniformity. In the present study, samples that are compared directly are always taken from the same sputter run.

3.4.2.1 Outcoupling efficiency

It is obvious that an increased probability for photons to escape the device in the direction of the viewer (detector), η_{opt}, would provide a concomitant increase in both brightness and efficiency. To a first approximation, assuming flat surfaces and no interference, optical outcoupling from a medium with higher index of refraction (n for ZnS = 2.4) to one of a lower index (n for air = 1.0) is determined by Snell's Law:

$$n_1 \sin\theta_1 = n_2 \sin\theta_2$$

where θ_1 is the angle of incidence and θ_2 the angle of the transmitted ray. This leads to the case of total internal reflection for $\theta_2 = 90°$ when $\theta_1 = \theta_{cr}$. For ZnS ($n = 2.4$) θ_{cr} is 23.5° which, assuming perfectly reflecting back electrodes (reasonable for our devices), leads to only ~13% of the generated photons escaping the device. For displays that use contrast-enhancing dark backing layers, this efficiency can be much worse.

Outcoupling efficiency can be improved by lowering the index of refraction of the phosphor layer. For this analysis we can use the approximation $\kappa = n^2$ where κ is the dielectric constant of the material, and relate the relative indices of refraction to the corresponding dielectric constants. We have the values of the dielectric constant for the total device in the sub-threshold regime of Figure 3-14 for (a) the KCl co-doped and (b) undoped samples, respectively, and they are almost exactly the same, with any small difference being decreased further upon conversion to the index of refraction. This implies indirectly that the critical angle for internal reflection does not change with KCl codoping.

A second device characteristic that could increase outcoupling efficiency is increased surface roughness, which would reduce internal refection. It has been shown that surface roughness can result in a value of η_{opt} in the range of 0.1 - 0.4 [124]. For a measure of this possibility we use the diffuse reflectance of the device, and Figures 3-11 shows that KCl doping does not increase diffuse reflectance and therefore cannot account for increased efficiency.

3.4.2.2 Radiative efficiency

There is a simple, often overlooked effect dealing with the de-excitation process by which the luminous efficiency could be improved. Attention must be drawn to one of the significant differences between the unitless efficiency term used here to discuss the device operation and those used in the Results section to describe actual device efficiency. The units of lm/W are those most commonly used in the display and phosphor community because of their practical nature. These units relate luminous flux, easily measured with a spectrophotometer, divided by power, easily measured from the electrical input to the test device. But it should be noted that the units of lumens take into account V(λ), the photopic spectral efficiency of the standard observer. Therefore a spectral shift can result in an increase or decrease in efficiency when using these units, even though the radiated power does not change. From Figure 3-6 and discussions above, it was concluded that the spectral distribution does not change between KCl codoped and undoped samples after accounting for film interference effects. Therefore a chromaticity change is not responsible for the improved EL properties.

The radiative or relaxation efficiency as defined above is a measure of the efficiency with which excited Mn centers, Mn*, relax radiatively producing a photon. Relaxation efficiency in ZnS:Mn devices was discussed in detail by J. Benoit et al. [45]. They found that the relaxation efficiency under normal ACTFEL operation is determined by two mechanisms. First there is diffusion-limited relaxation, in which energy is transferred between various Mn atoms. This is a concentration-dependent effect, and the concentrations used in ZnS:Mn devices are above the concentration threshold for this process to occur. At very low concentrations the diffusion limited relaxation is not significant, and the relaxation behavior shows characteristic Mn* relaxation with $e^{-\alpha t}$ time dependence, and a time constant of 1.3 ms for hexagonal ZnS. However at concentrations used in ZnS:Mn devices the diffusion-limited energy transfer process leads to a modified exponential, $\exp(t/\tau)^{-n}$, behavior.

The second limiting process is excited state interaction which leads to non-radiative decay. This process appears as something like $Mn^* + Mn^* \rightarrow Mn^{**}$ followed by emission of less than two photons. This process occurs at high drive conditions, such as those used in ZnS:Mn devices, and is affected by both activator concentration and drive level. Benoit et al. showed that with increasing drive level, there is a corresponding decrease in luminous efficiency due to the excited state interaction process. By comparing the long-time behavior of a heavily doped device under high and low drive conditions, Benoit et al. showed that the diffusion limited transfer process and excited state interaction process are independent of one another.

In Figure 3-7 it can be seen that under PL excitation, which is a low excitation condition due to the forbidden nature of the Mn^{2+} $^6A_1 \rightarrow {}^4T_1$ transition, the decay behavior of emission is identical for the KCl codoped and undoped devices. The decay follows the modified exponential behavior characteristic of the diffusion limited transfer process. This leads to the conclusion that the addition of KCl does not affect the diffusion limited transfer process. Since this is a primarily concentration-dependent effect, then the conclusion can be drawn that the KCl codoping does not affect the number of active Mn^{2+} ions contributing to luminescence.

Figure 3-9 shows the EL decay behavior for KCl codoped and undoped devices driven at 40V above threshold. It should be noted that this data is not spectrally selective, and that no filters or monochromator was used with the PMT. This high drive condition can lead to the occurrence of both non-radiative processes mentioned above. The decay in Figure 3-9 cannot be fit by exponential decay, modified exponential decay, or a combination of both. Also included in Figure 3-9 is the decay behavior for an undoped device driven at threshold. The data show that there is a small difference in the decay behavior with and without KCl codoping. This difference is seen more noticeably in Figure 3-10, which shows the same devices on a smaller time scale. A more rapid decay after the voltage is removed is observed for the KCl doped device for both polarities.

The decay is slightly faster for the undoped device when the Al electrode is the cathode than when the ITO is the cathode. When viewed on a longer time scale it is shown that the decay is also slightly faster for the KCl doped device when the Al electrode is the cathode than when the ITO is the cathode. In addition the decay of even the un-doped device at V_{40} is slightly faster than at threshold. Assuming the threshold decay to be the maximum luminous efficiency possible for these particular devices, the integrated intensity from the normalized decay curves can be used to compare the luminous efficiency for these samples. The results were given in Table 3-2. These show that the luminous efficiency actually decreases for devices doped with KCl, but only by ~4%. Reduced luminous efficiency is the expected result considering the excited state interaction process which has been shown to decrease this efficiency as excitation is increased.

From these observations it can be concluded that the improved performance due to the addition of KCl to ZnS:Mn devices does not come from an increased luminous efficiency nor a shift in spectral distribution. In fact, a small decrease in radiative efficiency of ~4% can be attributed to excited state interaction in the KCl doped devices.

3.4.2.3 Excitation efficiency

The analysis of excitation efficiency is not quite as straightforward as the other processes. Excitation efficiency refers to the number of excited states, in this case Mn*, created for every electron transported from the momentary cathodic phosphor/insulator interface to the anodic interface. With some approximations we can measure the relative excitation efficiency experimentally, following the procedure outlined by Zeinert et al. [63, 122]. Using the approximation that the initial brightness of a phosphor after an excitation pulse much shorter than the decay time (so that the extent of de-excitation is negligible) is proportional to the number of excited states generated during that pulse, then we can use the following relationship:

$$\eta_{exc} = \frac{\text{conc. excited centers}}{\text{no. electrons transported}} \propto \frac{B_{\max}}{Q_{\text{int}}}.$$

The proportionality consists of measurable quantities, although the measurement of Q_{int} itself contains some assumptions and approximations (see Section 2.8). If the value for B_{max}/Q_{int} is plotted as a function of maximum applied voltage or transported charge, then the effect of excitation efficiency on overall device performance can be analyzed.

Figures 3-15 and 3-16 show how these quantities were measured using a 5 μs excitation pulse. Figure 3-17 shows the resulting values obtained for each polarity for a KCl co-doped versus an undoped sample as a function of voltage. Several observation can be made from the data in Figure 3-17. First, the excitation efficiency is 26% higher when the ATO/ZnS interface is the cathode both with and without KCl doping. Second, the excitation efficiency is ~75% higher for the KCl doped sample than for the undoped sample for both polarities. It is also interesting to note the similarity of the excitation efficiency as a function of voltage and the overall efficiency versus voltage, such as that seen in Figure 3-2. This increased excitation efficiency appears to be the primary source of improved device performance from the addition of KCl, as discussed further below. However, an understanding of the reason for the improved excitation efficiency is needed.

As discussed by Mach and Mueller [42], the excitation efficiency can be further divided into

$$\eta_{exc} = \eta'_{exc}\,\eta_{hot}$$

where η_{hot} is the efficiency with which injected electrons are accelerated to "hot" energies sufficient to excite a Mn atom by direct impact, and η'_{exc} is the efficiency with which the hot electrons find and excite the Mn dopants. Mach and Mueller argue that since the impact length, l_i, of electrons at normal operating fields (for 1.5 MV/cm, impact cross-section $\sigma = 2 \times 10^{-16}$ cm^2, and $N_{Mn} = 1.5 \times 10^{20}$ [cm^{-3}], $l_i \approx 330$ nm) is much larger than the length, l_a, over which a freely accelerating electron will acquire the energy required to excite a Mn^{2+} ion (for 1.5 MV/cm and excitation energy 2.5 eV, $l_a = 17$ nm), then $\eta_{hot} \approx 1$, and therefore η_{exc} can be assumed to be equal to η'_{exc}. η_{exc} would then be just the impact length, l_i, which is determined only by the inverse of the concentration of Mn^{2+} centers times the impact cross section of the Mn^{2+} centers.

The estimated concentration of K^+ (or K^- for an interstitial) and Cl^- ions is estimated as 1×10^{19} [cm^{-3}], as compared to the Mn doping concentration of 1.5×10^{20} [cm^{-3}]. So the effect of KCl doping on η'_{exc}, or more specifically σ, the impact cross section, can be assumed as negligible. But since η_{exc} does increase, approximating η'_{exc} as the probability of impact, (i.e. assuming an impact excitation efficiency of unity), seems incorrect. The assumption of the probability of an electron being hot upon impact seems oversimplified and requires further examination. In Section 2.6.2 it was shown that the probability of an electron achieving sufficient energy to impact excite Mn^{2+} in ZnS was found to be different by different researchers, but in all cases but one was found to be significantly less than unity.

One important observation from Figure 3-10 is that there is no evidence of trailing edge excitation. Therefore any processes involving Mn ionization and electron recapture or exciton capture and energy transfer to Mn^{2+} do not appear significant. This supports the idea that there is no significant change in η'_{exc}.

It was shown in Section 2.6.2 that the excitation probability increases with field. In fact it was shown by Bringuier [24] that for a given external voltage (or average phosphor field) excitation efficiency is maximized when the field is uniform. Therefore the effects of non-homogeneous fields, which certainly are present due to bulk and interface space charge [22, 26, 70, 76, 85, 125-128], can not be neglected. It appears that the observed increase in excitation efficiency must come from these effects which alter the efficiency with which the electrons which travel from one phosphor/insulator interface to the other are able to generate Mn*.

3.4.3 Modified Interface Microstructure

The characteristics of the charge injection can certainly play a role in the efficiency of the device. More specifically, this characteristic can modify excitation efficiency. It has been shown in asymmetric devices where charge injection occurs at lower fields for one polarity, and of course the same amount of charge flows during that polarity than for the opposite one, as much as five times lower emission can result [16]. Charge injected below the threshold field necessary for efficient excitation is simply dissipated and the efficiency is lower.

It was shown that the bulk microstructure does not change dramatically [77, 96]. But significant change does occur at the nucleation surface of the ZnS layer when KCl is added. Grains grow and become columnar rather than remain as small, equiaxed grains such as in the as deposited and undoped, annealed films. This interface modification could result in the improved performance seen in the KCl doped vs. undoped films.

However there are two pieces of evidence which indicate that this is not a factor in the case of KCl co-doping. The strongest is the data in Figure 3-17, which show that the improved excitation efficiency is of similar magnitude for both polarities. Second, the relative intensities of the positive and negative pulses, shown in Figure 3-8, are similar for the co-doped and undoped samples, which suggests only a minor role played by the nucleation microstructure. For the KCl co-doped sample the intensity when the ATO/ZnS interface is the cathode becomes 14% larger than for the other polarity. After averaging the two polarities, this can account for only a 7% improvement in brightness and cannot explain the ~50% improvement seen for the efficiency.

This is a truly surprising result considering the dramatic change in interface microstructure after doping with KCl [77]. In short, it implies that the nature of the interface does not have a significant role in the improved performance, but rather that bulk properties of the ZnS layer are responsible.

3.4.4 Space Charge Effects

Still remaining is the investigation of the last two possible mechanisms for improved excitation listed at the beginning of Section 3.4. These two effects are an increased electron energy distribution, and the addition or removal of space charge in the phosphor bulk by ionization and/or carrier trapping. They are somewhat related and will be discussed together. However both require an introductory discussion of the current understanding of space charge in EL devices.

One of the least understood aspects of ACTFEL devices is the development of band bending due to trapped charge in the phosphor bulk. There is compelling evidence that it exists, as discussed below. However, all electrical measurements made to the two-terminal devices measure only external quantities, and the distribution of internal properties through the thickness of the phosphor layer cannot be determined in a straightforward and conclusive manner.

3.4.4.1 Definitions and characterization

The topic of space charge requires a brief introduction to the terminology unique to the field for the different types of space charge and how each may manifest itself. First, there is the issue of field clamping. This refers to the development of a constant phosphor field at or near the voltage at which significant charge injection takes place in the phosphor film (threshold voltage), due to development of an opposing field created by the conducted negative charge trapped at the anodic interface. This was mentioned in the discussion of the equivalent circuit model in Section 2.5.2. Space charge is simply a distribution of charge such that there is a local net negative or positive charge over a particular area. In the normal operation of an ACTFEL device there is no net current across the insulators, but rather just the movement of charge from one phosphor interface to the other. Thus every time an electron is stripped from a ground state and used in conduction, there is a separation of charge. Under normal circumstances the electron is transported to the anode with the positive charge remaining at the cathode, and therefore the field lines in the phosphor do not bend in the bulk of the phosphor because no charge is trapped there. There is only a net reduction in the applied field in the phosphor layer. In many ZnS devices, when the threshold field for electron tunneling is reached, the field is clamped due to this negative feedback field from the conduction charge. This field is normally observed as the vertical (B-C and G-H in Figure 2-14) portions of a Q_{int}-F_p plot. If lattice impact ionization takes place creating an electron-hole pair, and the electron and hole are able to travel freely to the anode and cathode, respectively, then these electrons and holes also contribute to field clamping and result in no net band bending in the phosphor bulk.

On the other hand, there are several mechanisms by which charge can be trapped within the phosphor layer, which results in a bending of the field lines in the phosphor. Among them are lattice ionization followed by hole trapping, as well as either field or impact ionization of defect centers. These defect centers might be intentional dopants such as Cl substituted on an S site (Cl_S), a K interstitial (K_I), or Mn substituted on a Zn site (Mn_{Zn}), or might be unintentional point defects such as vacancies (V_{Zn} or V_S) or complexes between unintentional and intentional point defects. In the case of lattice ionization followed by hole trapping or impact ionization of impurities there is necessarily a fixed positive charge in the lattice, assuming the ionizing electron reaches the anode. These two mechanisms, namely lattice ionization followed by hole trapping vs. trap-to-band ionization, are significantly different in terms of device operation, as will be discussed shortly.

The terminology typically used in the literature distinguishes between "static" space charge, which does not change in magnitude over times in the range of the excitation period, and "dynamic" space charge, which is created and annihilated on the time scale of the excitation frequency [26]. More recently there has been reference to "fixed" space charge, which is not created by an applied voltage and for steady state operation is no different than static space charge, which normally builds to a steady state after some short period of operation (usually ~3-4 periods of voltage [23, 129]).

There are several techniques used to identify space charge. One is the use of dynamic capacitance-voltage (C-V) plots such as those in Figure 3-21. Capacitance overshoot at turn-on is a conclusive indication of dynamic space charge. (Here capacitance overshoot is defined as a rapid increase followed by a decrease and saturation of at higher voltage. In some literature, any increase that saturates above the expected insulator capacitance is called an overshoot, but that terminology is not used here.) The data used in a C-V plot come from the instantaneous value of dQ/dV, or in the specific case of Figure 3-21, from i/(dV/dt). Thus overshoot represents a transient period when a larger amount of current flows through the phosphor, but only for a short period of time, and therefore must involve a transient current flow which is changing on the time scale of the excitation pulse.

A second method of characterizing space charge is the use of a Q^{e}_{max}-V_{max} or a Q^{int}_{max}-V_{max} plot, sometime referred to as a transferred charge capacitance plot, since the slopes are characteristic of a capacitance value. In a Q^{int}_{max}-V_{max} plot, the sub-threshold slope is essentially zero since the device capacitance is subtracted from the charge values. If there is no conduction charge in the phosphor, then the above threshold slope in a Q^{e}_{max}-V_{max} plot should equal the insulator capacitance. Conduction charge would yield an increased slope, as would charge multiplication. However, positive space charge would yield an overshoot at threshold, such as the one seen for the no-KCl device in Figure 3-19. This is due to the larger amount of injected charge than would be expected based on the assumption of an average field. Unfortunately, there is no way to distinguish between static and dynamic space charge using a Q_{max}-V_{max} plot. If there is C-V overshoot it can only be concluded that there is at least some dynamic space charge.

If there is transferred charge-capacitance overshoot and no C-V overshoot, then static rather than dynamic space charge exists.

3.4.4.2 Origin and modeling of space charge

As mentioned previously, space charge will occur any time there is conduction charge in a device. However we are only interested in charge which is stored in the phosphor bulk and therefore affects the field distribution. This can occur due to ionization of fixed centers, whether they are intentional dopants or point defects. Or it can occur due to lattice ionization and subsequent hole re-trapping.

Because external data cannot easily give conclusive data regarding the internal field, modeling of electrical behavior is the most promising technique for learning about space charge and its variation as a function of time and space [26]. However many modeling efforts assume an average field across the phosphor, neglecting variations of local field strength [22, 68, 130]. An excellent review of modeling efforts, illustrated by recent results, is given by Hitt et al. [26]. They use a model in which the phosphor layer is considered as a series of discrete capacitors, each in parallel with a voltage dependent current source. This is shown schematically in Figure 3-22. The current sources are then mathematically defined to account for tunneling from defect states, lattice and defect ionization either by impact, tunneling, thermalization, or phonon-assisted tunneling, and field- and occupancy- dependent capture of electrons and/or holes in deep traps. The individual layers then form a system of first order differential equations which can be solved numerically and determine the stored charge in each layer as a function of time. The published results are very impressive in terms of the ability of the model to mimic measurable external properties in ZnS:Mn devices.

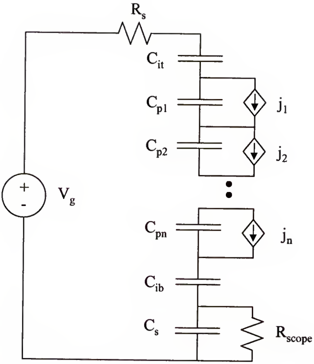

Figure 3-22. ACTFEL device equivalent circuit used for state-space analysis. The ACTFEL device is modeled assuming ideal top and bottom insulators, C_{it} and C_{ib}, respectively, with the phosphor layer divided into n layers, each modeled as a capacitance, C_{pk}, shunted by a current density, j_k, with k representing the layer number. Measurement circuit elements also included in the model are the driving voltage source, V_g, the series resistance, R_s, and the sense capacitor, C_s, which is shunted by the oscilloscope resistance, R_{scope} [26].

Among the results of this model is evidence that dynamic space charge does lead to C-V overshoot. In addition, in a second type of model using a SPICE-based circuit model, Bender et al. were able to show that static space charge could account for transferred charge-capacitance overshoot [131].

Another interesting result of the model is the demonstration of the very different behaviors of lattice ionization followed by hole re-trapping vs. trap-to-band ionization as sources of space charge. For trap-to-band ionization, the ionization probability is highest in the high field regions near the cathode. This ionization leaves behind a positive charge, enhancing the local cathodic field, which essentially yields a positive feedback to the tunnel injection process. Since the charge is localized at the cathode, which changes for alternating polarities, the space charge is created and annihilated with each pulse, i.e. is dynamic space charge which leads to C-V overshoot.

Lattice ionization and hole re-trapping has an important difference compared to trap-to-band ionization. The lattice ionization is also most efficient in the high field regions near the cathode. Hole re-trapping on the other hand is most efficient in the low field regions farther away [26]. Therefore the space charge is located in the central portion of the phosphor. Since the charge centroid does not move appreciably for alternating polarities, trapped charge remaining after one pulse when the opposing pulse is applied appears as static space charge.

3.4.5 The Role of KCl in ZnS

3.4.5.1 Point Defect Structure

Understanding the effects of K and Cl in ZnS on the electrical properties requires some understanding of the point defect structure. Some information is known from the literature regarding these ions, and other information can be deduced. The intrinsic defects which are believed to be important in ACTFEL device operation are zinc vacancies, estimated to have a concentration of 7 x 10^{16} cm^{-3} [85]. Quantitative SIMS measurements show that the concentrations of K and Cl are estimated to be ~10^{18} and 10^{19} cm^{-3}, respectively [unpublished data].

Cl dopants are known to substitute on the S site in ZnS, creating a donor level 0.25 eV below the conduction band [92]. Zhai has shown that it is unlikely that Cl occupy any other site in the ZnS lattice due to its size [77]. SIMS data has shown that there is approximately one order of magnitude higher concentration of Cl in the lattice than K [96]. Neglecting K for the moment, charge equilibrium must be established due to the valence mismatch between Cl and S. Two possible mechanisms are available to achieve equilibrium. One is to move the Fermi level to higher energy and the second is to compensate for the charge mismatch with another defect. Shih *et al.* have estimated that as donor impurities such as Cl_S are added to ZnS, when the Fermi level reaches just 2 eV (E_g ~3.7 eV) it is thermodynamically preferable to create charge compensating vacancies, in this case V_{Zn}, than to move the Fermi level further [76]. This conclusion is also the intuitive one for the devices in this study considering the defective nature of sputtered ZnS films. So considering Cl impurities alone, it is possible to compensate for charge mismatch by creating one fully ionized V_{Zn} for every two Cl_S in the lattice. This agrees with the assertion proposed by Zhai which suggests that formation of V_{Zn} by adding Cl_S would explain the observed increase in dislocation glide and climb rates during annealing [77]. The Cl_S do not necessarily remain isolated in the lattice. There is experimental evidence that the Cl_S and V_{Zn} form Cl_S-V_{Zn} complexes, yielding a singly charged acceptor level rather than the doubly charged V_{Zn} level. This complex can then be compensated by the other Cl_S which is isolated. This type of charge compensation is shown schematically in Figure 3-23. Although no reports of it were found in the literature, it is also possible that some of the defects form neutral Cl_S-V_{Zn}-Cl_S clusters. These would be expected to form shallower levels and would be harder to detect experimentally. The formation of these complexes would not preclude those mentioned above which have been detected experimentally.

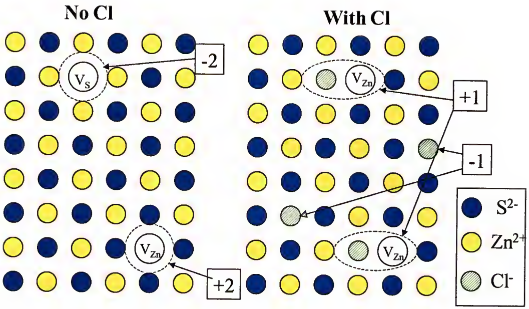

Figure 3-23. Schematic diagram showing the point defect and charge compensation structure expected when Cl is added to the ZnS lattice.

The role of K in the lattice is less clear. The two most probable sites that K would occupy are as a substitute for Zn on the cation site, and as an interstitial in the cubic phase as suggested by Zhai [77]. In the sense of the electrical behavior of the device it is not critical which of these is the case. As mentioned previously, the concentration of K was shown to be approximately one order of magnitude lower than that of Cl. If the K ions are incorporated substitutionally, they would act as electrical acceptor states. They would compensate for Cl donor levels both electrically and in terms of lattice charge, and reduce the number of Zn vacancies generated by the Cl donors by a factor of ~10%. On the other hand, if the K ions are incorporated interstitially, they would act as electrical donors, thus behaving similarly to the Cl donors both electrically (assuming the donor levels are similar, which is not known) and in terms of charge compensation. These two concepts are shown schematically in Figure 3-24. In either case the net effect would only be a fraction of the effects of the Cl donors which are more abundant.

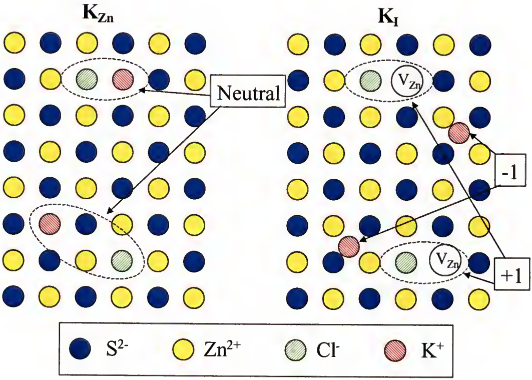

Figure 3-24. Schematic diagram showing two possible incorporation sites and the resulting charge compensation schemes for K in ZnS.

3.4.5.2 Effect of KCl doping on space charge and excitation efficiency

In the previous section it was shown that Cl added to ZnS is likely to result in V_{Zn} which have been experimentally shown to form V_{Zn}-Cl_S complexes. Analysis of the defect levels was given in Section 2.9.4.2. To summarize, it is believed that the defect energy level for Cl_S is 0.25 eV below the conduction band, and the energy levels for V_{Zn}^{2+}, V_{Zn}^{+}, and V_{Zn}-Cl_S are ~1.0, 0.44, and 0.2 eV above the valence band, respectively. The addition of a relatively large concentration of Cl and K compared to the concentration of intrinsic defects should result in clustering of a large number of the intrinsic zinc vacancies with Cl or K donors. According to the equation for tunneling from a Dirac well, which is appropriate for discrete states [22], the emission rate for a 0.5 eV trap is $>10^7$ times that for a trap depth of 1.0 eV. These traps would be effectively destabilized under the high field present during device operation. For a hole trap distribution made up primarily of singly ionized V_{Zn}-Cl_S complexes rather than doubly ionized V_{Zn}'s, it is expected that the space charge density due to lattice ionization followed by hole re-trapping would be reduced.

A second mechanism by which the space charge might be reduced deals with the fact that trapped charge must be stable during the time between voltage pulses. It was mentioned that the concentration of (Cl + K) is on the order of 10^{19} cm^{-3}, while the concentration of intrinsic vacancies is 10^{16} cm^{-3}. A consequence is the close proximity of electron and hole traps for the KCl co-doped films. For a uniform distribution, the distance between two V_{Zn}'s, $R_{V\text{-}V}$, is ~24 nm. For a uniform Cl concentration of 1 x 10^{19} cm^{-3}, $R_{Cl\text{-}Cl}$ is ~4.5 nm. This is close to the exciton Bohr radius of 2.2 nm in ZnS [132] and would result in more efficient annihilation of trapped electrons and holes under low fields, again reducing the space charge density.

Evidence supporting reduced hole trapping comes from several measurements. First, there is no evidence of C-V overshoot in either sample (Figure 3-14a and b), which indicates the absence of a significant amount of dynamic space charge. Other sputtered ZnS:Mn devices produced during this work have shown C-V overshoot, but the KCl doped samples did not significantly change the magnitude or character of the overshoot. In addition, the transferred charge-capacitance overshoot, an indication of space charge which must be static in the absence of C-V overshoot (Figure 3-19 for sputtered samples with and without KCl and in Figure 3-21 for an evaporated sample), show the expected trend. The amount of overshoot is largest for the sputtered sample, which has been shown to be more defective relative to evaporated films [133]. The evaporated sample shows less overshoot, while the KCl doped sample shows little or no overshoot.

A significant piece of evidence supporting reduced space charge is a larger threshold voltage, which was shown repeatedly for KCl doped samples (Figures 3-2 and 3-4). The mechanism for this is discussed shortly.

The assertion of improved excitation efficiency due to the reduction of space charge is not an obvious conclusion and must be discussed. Improved overall efficiency and excitation efficiency in ZnS:Mn devices when no space charge is present has been demonstrated by several investigators. In one case [129] this was achieved by electrically "resetting" the space charge in a device to zero by using a halogen lamp to excite trapped charge into the conduction or valence band. This technique has been demonstrated to effectively reduce stored charge in the device [72, 129, 134, 135]. The transient electrical and optical behavior was then studied for the first pulses as compared with those at steady state. It was shown that the overall efficiency was in fact higher for the first several pulses, before static space charge is developed for the steady state. A higher operating voltage was also observed for the reset devices. In other work [135] "virgin" samples (samples which have not been operated) were used to demonstrate higher excitation efficiency for the first pulses before space charge develops. And finally for ZnS:Mn devices [134] and for SrS:Ce devices [72], constant UV illumination during high voltage excitation is used to reduce space charge generation by depopulating trapped carriers; improved excitation efficiency was demonstrated and higher operating voltage was needed. From a mathematical approach, Bringuier has shown that for a given applied voltage, the most efficient excitation is achieved for flat bands (no space charge) [24]. Adding the fact that higher voltages are needed when space charge is reduced improves the excitation further.

The mechanism by which excitation efficiency is increased by reducing space charge is shown schematically in Figure 3-25. The figure on the left shows a schematic band diagram similar to what is usually seen in the literature to demonstrate the band bending associated with space charge. A decrease in space charge has the effect of flattening the bands closer to the flat-band or average field case. However a more accurate depiction of the case in ACTFEL devices is shown in Figure 3-25 on the right hand side. This figure also shows a band diagram, but instead of assuming the same average field for two different magnitudes of space charge, an identical local field at the cathodic interface is assumed. This is more realistic since this is the condition that determines the onset of conduction charge. It is seen in Figure 3-25 that a reduced amount of space charge results in an increased field across the entire phosphor layer, particularly in the anodic region. The increased field and extension of the high field region to a greater depth of the phosphor layer explains why the excitation efficiency is higher for cases in which space charge is reduced. It also would result in increased charge multiplication. This increased field across the phosphor also results in a higher average (or applied) field, represented in Figure 3-25 by $V_{a2} > V_{a1}$, which explains the increased threshold voltage measured experimentally.

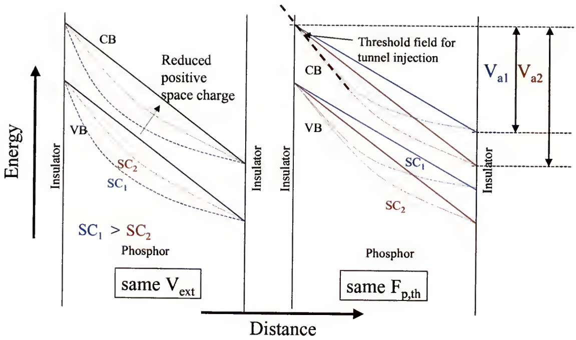

Figure 3-25. Schematic band diagrams showing the effect of positive space charge relative to (a) a constant average field and (b) a constant cathode field. Note that the case for reduced space charge at a constant cathode field results in increased V_{th}.

3.4.5.3 Effects of KCl on conduction charge

One of the interesting characteristics of the KCl doped devices is the positive slope above threshold in the C-V behavior (Figure 3-14a). This slope is consistent regardless of V_{max}, and appears to intercept the origin. To investigate the source of this increasing dynamic capacitance, a more careful look at the measurement technique and data interpretation is necessary. The capacitance values for these curves are calculated from the instantaneous current and voltage values as:

$$C = \frac{i}{\left(\frac{dV}{dt}\right)}.$$

The capacitance values below threshold, where there is very little conduction current, closely approximate the total device capacitance. Above threshold, the capacitance can only be as large as the insulator capacitance, unless there is additional conduction current. The above analysis assumes that the components are purely capacitive. If on the other hand, the current is a function of voltage, such as an ohmic resistance where $V = iR$, then the capacitance values will be given by:

$$C = \frac{V}{R * \left(\frac{dV}{dt}\right)}$$

which gives a linear voltage dependence to the calculated capacitance. Of course below threshold where there is no conduction current, the phosphor layer acts as a pure capacitor as expected. However, if above threshold the phosphor layer is not shunted out of the circuit as assumed, but rather limits the current by internal resistance, then the behavior for the KCl doped device in Figure 3-14 (a) is expected. The observed conduction mechanism can be said to be ohmic, since other conduction mechanisms such as Schottky or Poole-Frenkel conduction would not extrapolate to the origin. Therefore from this plot the ohmic resistance value was measured to be 1.6×10^6 Ω-cm, which is several orders of magnitude lower than the range reported for ZnS of 10^8-10^{14} Ω-cm [136]. This could be explained by the carriers in shallow traps, by active donors in the bulk, or could also be attributed to a current limitation in only part of the phosphor layer. The value is not suggested to be the bulk resistivity of the ZnS films, but rather an "effective" resistance of the devices. Limited current injection is normally attributed in ACTFEL devices to either insulator capacitance or to a small density of states which is insufficient to completely charge the capacitors. The presence of this resistive behavior is an indication that the current limit in this device is due to the bulk phosphor resistance, a situation which has not been previously observed. This resistive behavior is possible because of the large amount of electron multiplication or the ionization of donors as discussed earlier and seen in the C-V and Q^{int}_{max}-V_{max} behavior.

CHAPTER 4
Zn_2GeO_4:Mn ACTFEL DEVICES

4.1 Introduction

The most commonly used and most comprehensively studied ACTFEL phosphor hosts are sulfur-based compounds. Oxide compounds have not been as extensively investigated because of the general requirement for higher processing temperatures to achieve good crystallinity in oxides, and the empirical observation that they are not capable of transporting a significant current density of hot electrons [3]. Recent work on several oxide-based phosphor systems which indicates that some oxides may in fact be excellent candidates for ACTFEL displays has led to renewed interest in the potential of oxide ACTFEL phosphors [20].

Advances in blue emitting ACTFEL phosphors have resulted in a need for brighter, more efficient green emitting phosphors. Coincidentally, the best performing oxide based phosphors are green-emitting phosphors [20]. This has led to the current investigation of Zn_2GeO_4:Mn as a potential oxide phosphor material.

A brief analysis of microstructure/stoichiometry/morphology was performed which demonstrates the onset of crystallization between 600 and 700°C, which is consistent with reports in the literature. Optical characterization was performed to reveal an optical bandgap of 4.68 eV for Zn_2GeO_4:Mn thin films, as well as a defect state with a depth of 615 meV. Efficient energy transfer from this state to the Mn^{2+} excited state was observed. Transient electrical and optical measurements reveal anomalous behavior.

The behavior is explained by a combination of slow onset of conduction current, tentatively attributed to the phosphor RC time constant, an unusually large amount of dynamic space charge near the cathode, and nearly resonant energy transfer from defect to Mn* are used to explain the observed phenomena.

In Section 4.2 the experimental procedure for this study is presented. Section 4.3 presents the results of the study, and in Section 4.4 the results are discussed.

4.2 Experimental Procedure

ACTFEL devices with the standard MISIM device structure were fabricated using RF magnetron sputtering to deposit the Zn_2GeO_4:Mn phosphor layer. The procedure is similar to that described in Section 3.2. A process flow diagram is shown in Figure 4.1, and the details of the individual step are given in this section. Two different sets of experiments were used in this study using independent sputter targets and deposition systems. One set of samples was fabricated using equipment at Planar Systems, Inc. The second was performed at the University of Florida. For the sake of simplicity, samples from the first set of experiments will be referred to herein as “Planar” samples, and the second set as “University of Florida” or just “UF” samples.

4.2.1 Substrate Preparation

The substrates for the Planar samples consisted of NEG glass, which allows higher temperature processing than standard soda-lime or Corning 7059 glass. Softening of the glass substrate was observed after annealing at 860°C for 2 minutes. However for evaluation purposes, the devices did not show any noticeable degradation due to this softening. For the UF samples Corning 7059 glass was used. For both experiments the transparent electrode was ITO deposited by an outside vendor. The bottom dielectric was ATO deposited by atomic layer deposition (ALD) by Planar Systems, Inc. Prior to phosphor deposition the substrates were cleaned with methanol followed by an ozone clean for six minutes to remove organic residuals.

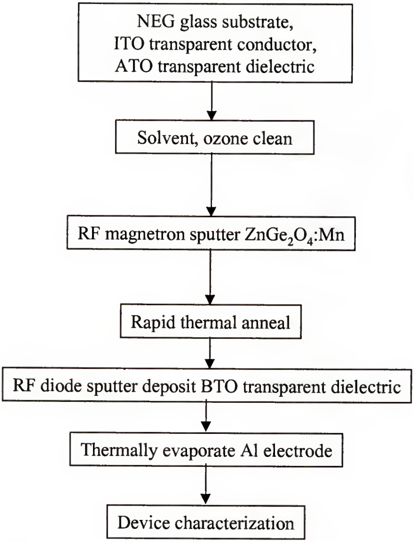
NEG glass substrate,
ITO transparent conductor,
ATO transparent dielectric
Solvent, ozone clean
RF magnetron sputter $ZnGe_2O_4$:Mn
Rapid thermal anneal
RF diode sputter deposit BTO transparent dielectric
Thermally evaporate Al electrode
Device characterization

Figure 4-1. Process flow diagram for the preparation of Zn_2GeO_4:Mn ACTFEL devices.

4.2.2 Sputter Target Preparation

Three different sputter targets were used for these experiments. The two sputter targets used for the Planar samples were prepared at Sarnoff Labratories, Inc. and details of the preparation are not available. These two targets consisted of non-stoichiometric Zn_2GeO_4:Mn, with excess GeO_2 added to the starting powder. The Zn:Ge ratio in the starting material was 3:2 rather than the stoichiometric ratio of 2:1. In addition 1.5% Mn (relative to Zn) was added as the activator. One of the targets also had a small amount of SnO_2 added to the starting material. The excess GeO_2 was added due to improved performance seen in Zn_2SiO_4:Mn when excess SiO_2 is added [93]. The incorporation of SnO_2 is believed to result in deep level traps, and the effects of these traps were to be investigated [93]. The no-SnO_2 and SnO_2-doped targets were 2" and 3" in diameter, respectively.

The target used to deposit the UF samples was fabricated by solid state reaction. The starting materials were ZnO, GeO_2, and MnO_2, all 99.999% pure (metal basis) Puratronic® from Alfa Aesar. The powders were weighed and combined for stoichiometric Zn_2GeO_4 with 1.5% (Zn-substituted) Mn. The powder mixture was ball milled in acetone for 18 hours and dried by evaporation on a hot plate. The powder was then fired in air at 800°C for 16 hours.

After firing and re-crushing the powder using a mortar and pestle, the powder was uniaxially pressed at room temperature into a 31.75mm diameter pellet. The pellet was sintered at 1050°C in air for 6 hours. The sintered pellet was shaped into a 1" diameter target and mounted to an aluminum backing plate.

4.2.3 Device Fabrication

The device structure for standard experiments was the conventional MISIM structure using the ITO/ATO layers on the substrate as the bottom electrode and insulator, respectively. This structure was discussed and illustrated in Section 2.4.1.

4.2.3.1 Planar samples

The sputter sources were built by AJA International, and the chamber was a custom built turbo pumped system with a base pressure ~1 x 10^{-7} torr. The samples were on the perimeter of a rotating stage and each sample passed underneath the sputter gun one time, similar to a linear pass. The sputter gas was a 60/40 mixture of Ar/He, with O_2 added for some experiments. Deposition parameters such as pressure, O_2 partial pressure, substrate temperature, and sputter power were varied in the range given in Table 4-1 to improve the brightness and efficiency.

The phosphor layer thickness varied from 200 to 800 nm, but was typically ~400 nm thick. After deposition of the phosphor, the samples were typically annealed in an RTA furnace with a N_2 ambient. Occasionally the samples were annealed in a muffle furnace in air.

Table 4-1. Range and best value of processing parameters used for the phosphor layer in the Planar Zn_2GeO_4:Mn samples.

Processing parameter	Range investigated	Best conditions
Sputter pressure	5-35 mTorr	20 mTorr
O_2 partial pressure	0-6 mTorr	6 mTorr (extremum)
RF power (2” target)	60-100 W	100 W (extremum)
Substrate temperature	150-300 °C	250 °C
RTA temperature	600-860 °C	860 °C (extremum)

The top insulator was barium tantalate ($BaTa_2O_6$, or BTO), and was deposited by RF magnetron sputtering. This layer was typically 250 nm thick. The top Al electrode was then deposited by e-beam evaporation, and was 100 nm thick.

4.2.3.2 University of Florida samples

The phosphor layer sputter sources were built by AJA International, and were 1" in diameter. The system was a cryo-pumped system with a base pressure ~1 x 10^{-6} torr. The system was built by MRC, but with significant modification to allow the addition of the AJA sputter sources. The sputter conditions were based on the results of the parameter study with the Planar samples. The most critical difference between the systems is that the UF system did not allow substrate heating during deposition, and there was no sample motion. The standard deposition conditions are given in Table 4-2.

Table 4-2. Standard processing conditions used for the phosphor layer in the UF Zn_2GeO_4:Mn samples.

Deposition parameter	Value
Ar flow	70 sccm
O_2 partial pressure	4.5 mTorr
Sputter pressure	15 mTorr
RF power	20 W
Substrate temperature	Unheated
RTA temperature	800°C

The top insulator for the UF samples was BTO, and was deposited by RF diode sputtering. This layer was typically 250 nm thick. The top Al electrode was then deposited by thermal evaporation, and was 100 nm thick.

4.2.4 Device Characterization

4.2.4.1 Microstructural and chemical characterization

X-ray diffraction was performed on both target powders and phosphor thin films using a Philips APD 3720 powder diffractometer, employing Cu-Kα radiation at 40 kV excitation and 20 mA current. A continuous scan of 2θ with a scan rate of 0.020 deg/s was used for all samples.

For the Planar samples film thickness was measured using optical interference in transmission mode for a film deposited on a bare glass substrate. For the UF samples phosphor film thickness was measured and deposition rate was monitored by measuring a masked edge in the center of the sample using a Tencor AlphaStep profilometer. Film thickness variation in both studies was shown to be <10% across the useful portion of the substrate.

Scanning electron microscopy (SEM) was performed using a JEOL 6400 microscope at 15kV primary beam energy. The samples were coated with a thin layer of carbon to prevent charging. On the same system energy dispersive spectroscopy (EDS) was performed using a Princeton Physics detector. Digital imaging and EDS data was collected using a LinkISIS data collection system.

4.2.4.2 Optical characterization

Optical scattering was measured using a different technique than that described in Chapter 3. The technique measured scattering of a 620 nm HeNe laser source. The sample was place on the entrance aperture to a 4" integrating sphere. The beam was aligned so that after passing through the sample it struck the wall of the sphere. This was considered to be a case of perfect scattering and was used as the calibration value as measured by a photometer. The sphere was then re-aligned so that after passing through the sample the unscattered portion passed through a small exit aperture. The intensity inside the sphere as measured by the photometer was then recorded as the scattered intensity and scattering was calculated as the ratio of scattered intensity to the calibration value for perfect scattering.

Photoluminescence (PL) and photoluminescence excitation (PLE) spectra were collected using a Photon Technology International integrated PL system that used a 150W Xe lamp source for excitation and double ¼ m monochromators for both excitation and detection.

Electroluminescent brightness and efficiency vs. voltage data were collected on the Planar samples using a Pritchard spectrophotometer as well as a current meter. The excitation voltage was provided by a high voltage driver that supplies a trapezoidal waveform with a 5 μs rise, 30 μs dwell, and 5 μs fall time, operating at 60 Hz. The same driver was used for the UF samples, but brightness was measured using a Photoresearch PR-650 spectrophotometer.

Time-dependent and spectrally selective EL emission data were collected using an Oriel 77000 single grating 1/4m monochromator and a Si-based photomultiplier tube (PMT). The PMT output was measured using a 1kΩ bridge resistor and a Tektronix TDS 510A digitizing oscilliscope.

Electrical data was collected using a standard Sawyer-Tower bridge circuit similar to that shown in Figure 2-10, using either a 100 Ω resistor or a 30 nF capacitor as the sense element. Data was collected using a Tektronix TDS 510A digitizing oscilliscope.

Some time-resolved measurements were performed using a variable capacitor bridge, similar to the one shown in Figure 2-9. The high voltage waveform was obtained from an arbitrary waveform generator and high voltage amplifier. The voltage and conduction current were measured on a Tektronix digitizing oscilloscope. The transient light output was measured with spectral selectivity using a monochromator and Si-based photomultiplier.

4.3 Results

4.3.1 Planar Samples

4.3.1.1 Device properties

Basic EL performance data, namely brightness-voltage (B-V), efficiency-voltage (E-V), and chromaticity, were collected for all samples. The best device values were $L_{40} = 74$ cd/m^2, $E_{40} = 0.19$ lm/W, and CIE $x = 0.300$ and $y = 0.664$. The diffuse scattering for all samples was < 1%. The B-V behavior was primarily characterized by leaky subthreshold turn-on, very rapid increase, followed by B-V saturation. A set of B-V and E-V characteristics is shown in Figure 4-2.

4.3.1.2 Parameter study

Fifty-four runs were completed using the two targets during the Planar study. Many of the EL performance results are not conducive to systematic analysis due to modifications made to the system during the study. However, the trends observed while systematically changing processing conditions will be given in this section. The complete set of results is given in Appendix B. For plots of phosphor brightness versus any particular parameter, the samples were processed under identical conditions, other than the independent variable for that plot.

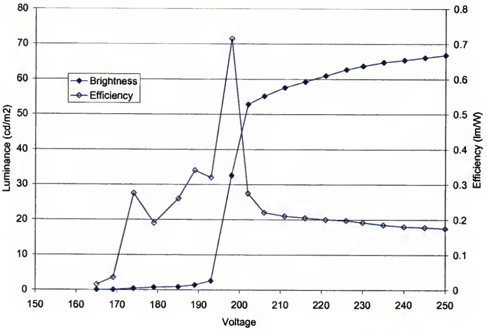

Figure 4-2. B-V and E-V characteristics of a Planar Zn_2GeO_4:Mn sample.

The correlation between EL characteristics and phosphor thickness was studied. A plot of the brightness value at 40 V above threshold, B_{40}, versus phosphor thickness for samples otherwise processed identically is shown in Figure 4-3. The B_{40} values are approximately linear up to ~600 nm. The value for a phosphor thickness of ~800 nm is less than expected according to the linear relationship. Most of the samples fabricated during this study had a thickness of ~400 nm. Therefore, for the sake of simple comparisons, the data presented in the remainder of this section is normalized for brightness to a value of 400 nm.

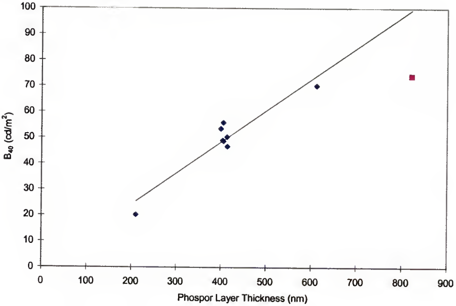

Figure 4-3. B_{40} versus phosphor thickness. The values are approximately linear up to ~600 nm.

The effect of oxygen added to the sputter gas was studied. The B_{40} values as a function of O_2 partial pressure in the sputter gas are shown in Figure 4-4a for samples with no tin added, and in Figure 4-4b for samples with tin. It should be noted that the total sputter pressure for each of these samples was not always the same, and varied from 20-35 mTorr. It is evident from Figure 4-4 that for both targets, some oxygen added to the sputter gas is necessary for reasonable performance. It also appears that a maximum B_{40} value has not been reached, though further studies at even higher O_2 partial pressures would be required to verify this.

The effect of RF power was investigated. Figure 4-5 shows the relationship between B_{40} and RF power for no-tin and tin added samples. The targets were not the same size, so the power density must be considered. The target with no tin had a 2" diameter, and the target with tin had a 3" diameter. Regardless, the performance of these samples is not strongly dependent on sputter power; for both targets an intermediate value was best. The samples with no tin added are less dependent on the sputter power.

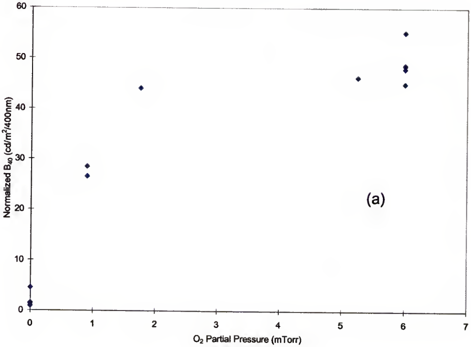

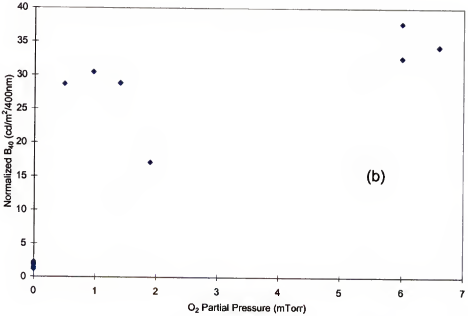

Figure 4-4. B_{40} versus O_2 partial pressure for samples (a) without and (b) with tin added.

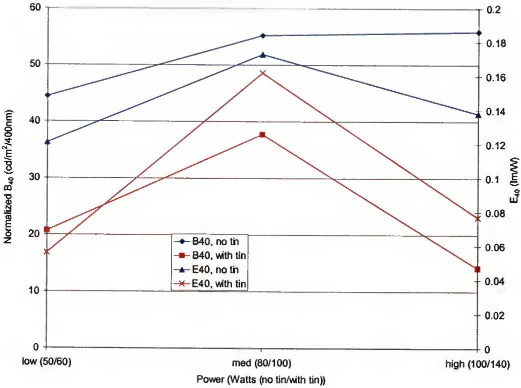

Figure 4-5. B_{40} and E_{40} versus applied RF sputter power for both no-tin and tin added samples.

Sputter pressure, the chamber pressure during sputter deposition, was briefly investigated. Two different sputter pressures were used for each target. The results are shown in Figure 4-6. For both targets the higher pressure, 20 mTorr, gave better results than the lower pressure, 5 mTorr. However, further investigation is required for process optimization.

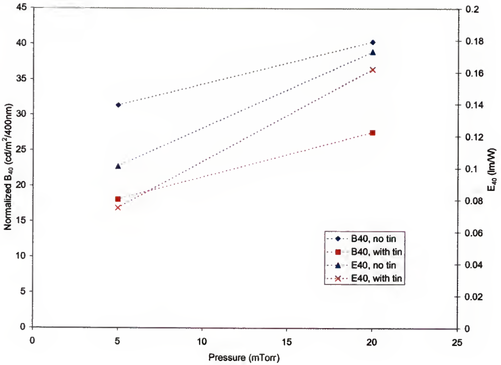

Figure 4-6. B_{40} and E_{40} at two different sputter pressures.

The effect of substrate temperature during deposition was investigated. The results are shown in Figure 4-7. The data show that the intermediate substrate temperature, 250°C, resulted in the best performance for samples with and without tin. Once again, the samples with tin were more sensitive to this parameter.

The effect of RTA temperature on device performance was investigated. The results of this study are shown in Figure 4-8. The RTA time was 2 minutes for all temperatures used. The onset of luminescence occurs between 600 and 650°C. It is not clear from this data whether there is a gradual increase in brightness with RTA temperature, or whether the improvement occurs in discrete steps. Further experiments are required to make a determination. It should be noted that the change in brightness after increasing the RTA temperature from 810°C to 860°C is not representative of the rest of the data. This can be seen from the data in Appendix B. Typically an improvement of ~20% in brightness by increasing the RTA temperature from 810°C to 860°C was seen. However, improvements of 0% to 100% were observed.

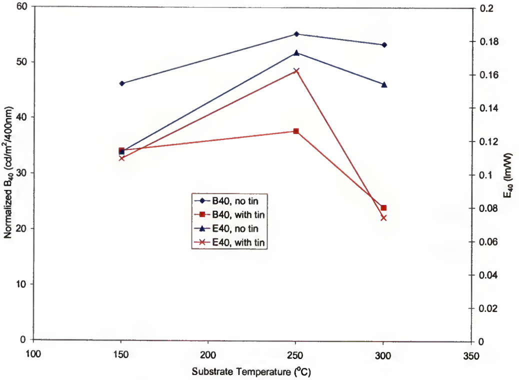

Figure 4-7. B_{40} and E_{40} values for various substrate temperatures during phosphor deposition.

4.3.2 UF Experiments

4.3.2.1 Target preparation

During target preparation, routine characterization techniques were used to monitor the characteristics of the target material. Figure 4-9 shows x-ray diffraction spectra from ball-milled, unfired target powder and from the sintered target, indicating complete transformation to Zn_2GeO_4, without a large amount of amorphous phase. An x-ray diffraction scan of pre-sintered powder also showed conversion to Zn_2GeO_4. Figure

4-10 shows a PL spectrum from the sintered target excited by a handheld UV lamp. The spectrum shows the characteristic green emission of the $^4T_1 \rightarrow {}^6A_1$ transition from Mn^{2+} in Zn_2GeO_4 with its peak wavelength at 537 nm. The small features at ~405 nm and 630 nm are artifacts from the UV lamp.

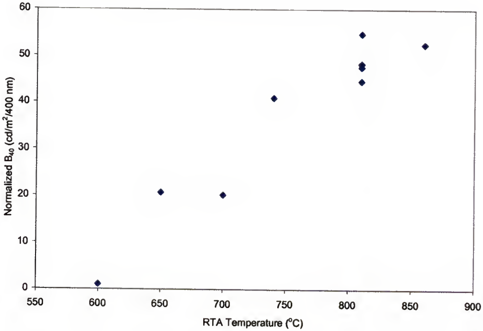

Figure 4-8. B_{40} values as a function of RTA temperature. All RTA conditions were for 2 minutes.

4.3.2.2 Sputtered Zn_2GeO_4 microstructural and chemical characterization

The crystallinity of some films from the UF study was investigated using x-ray diffraction for a range of RTA temperatures. All films were annealed for 2 minutes in flowing N_2. The results are shown in Figure 4-11. The variation with RTA temperature of the full-width at half-maximum (FWHM) of the Zn_2GeO_4 (006) peak is shown in Figure 4-12. There was no (006) peak present in the as-deposited film.

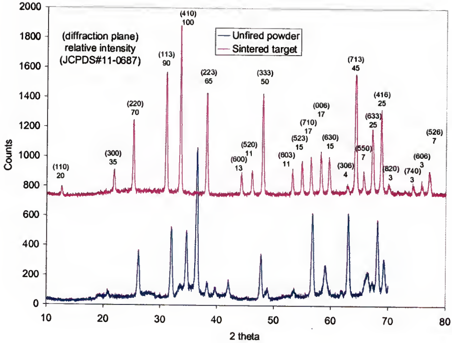

Figure 4-9. X-ray diffraction spectra for unfired target powder and Zn_2GeO_4:Mn, indicating the diffraction planes and relative intensities given in JCPDS file #11-0687 for Zn_2GeO_4 rhombohedral phase.

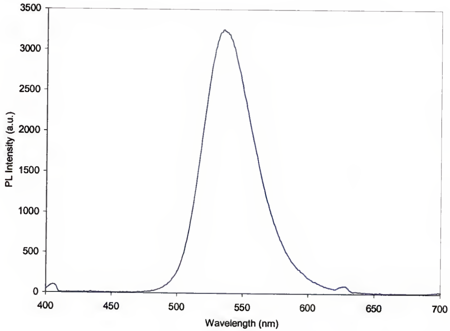

Figure 4-10. PL spectrum from Zn_2GeO_4:Mn target excited by a handheld UV lamp.

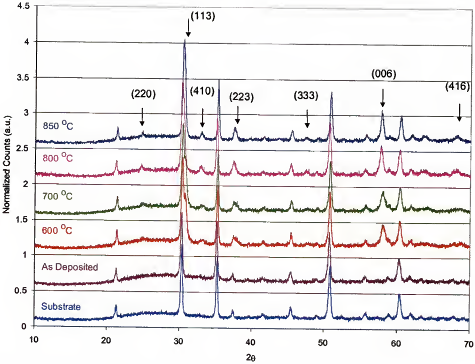

Figure 4-11. X-ray diffraction spectra for Zn_2GeO_4:Mn thin films annealed at a range of temperatures. All anneals were for 2 minutes in flowing N_2. Selected diffraction planes from rhombohedral Zn_2GeO_4 (JCPDS#11-0687) are indicated by the arrows.

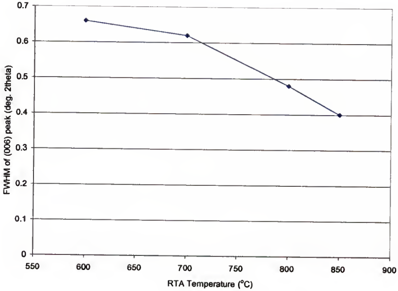

Figure 4-12. Variation of FWHM of the (006) diffraction peak with RTA temperature.

Scanning electron micrographs were collected to analyze the evolution of surface morphology with annealing. Figure 4-13 shows surface micrographs for samples annealed at a) 600, b) 700, and c) 800°C, respectively. Figure 4-13d shows a cross-section view of a sample annealed at 850°C, with the underlying ATO, ITO, and glass substrate apparent. The micrographs show that all of the surfaces are relatively smooth, with rounded surface features. There is little or no increase in the size or shape of the surface features at higher RTA temperatures.

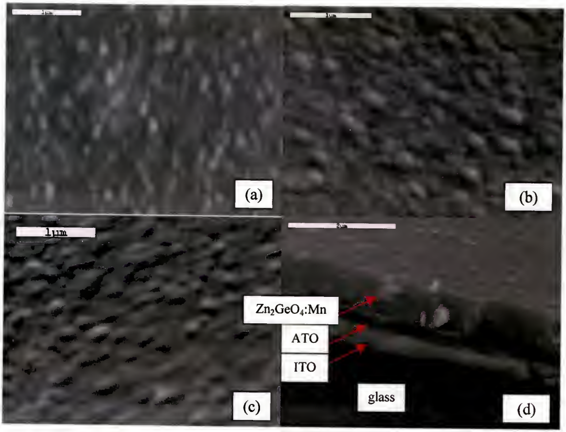

Figure 4-13. SEM micrographs of the surface morphology of samples annealed at (a) 600°C, (b) 700°C, and (c) 800°C, and (d) a cross-sectional view of a sample annealed at 850°C.

Energy-dispersive spectroscopy (EDS) was used to measure the composition of the films. The oxygen content could not be analyzed due to the underlying oxide layers, which confound the quantification routine. However, the relative amounts of Zn, Ge, and Mn could be analyzed, and the results are given in Table 4-3. The Zn/Ge ratio is fairly consistent, showing a slight increase at 850°C. The Mn concentration is very close to the expected 1.5% relative to Zn for the 600 and 700°C annealed samples. The concentration for the 850°C sample is about an order of magnitude lower at 0.2%.

Table 4-3. Zn/Ge ratio for a range of RTA temperatures.

RTA Temperature (°C)	Zn/Ge Ratio	Mn/Zn ratio
600	0.99	0.013
700	0.99	0.016
850	1.04	0.002

4.3.2.3 Optical characterization

Photoluminescence (PL) and photoluminescence excitation (PLE) spectra for a Zn_2GeO_4:Mn thin film are shown in Figure 4-14. The PLE spectrum was measured by monitoring at 540 nm, and the PL spectrum used 251 nm excitation. The PL emission spectrum shows the characteristic green emission of Zn_2GeO_4:Mn with a maximum at 535 nm. The PLE spectrum shows a broad absorption band with a maximum at 310 nm and a higher energy absorption band. More detailed analysis of the high energy absorption is shown in Figure 4-15. Traditional absorption spectra cannot be measured from these devices due to absorption from the ITO and glass layers. Because there is efficient transfer from the host lattice into the Mn^{2+} excited state (this is discussed in Section 4.4.2.2), the excitation into the host lattice is used to approximate a standard absorption measurement. The spectrum in 4-14 is plotted as the absorption (excitation) squared versus energy, and reveals an optical band gap for Zn_2GeO_4:Mn of 4.68 eV.

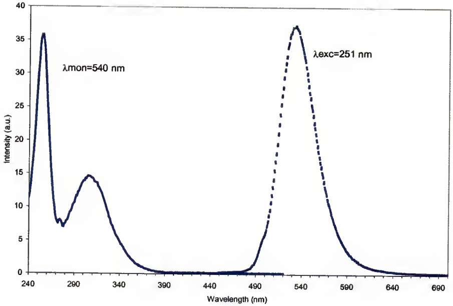

Figure 4-14. PL (dashed line) and PLE (solid line) spectra for a Zn_2GeO_4:Mn thin film. The PLE spectrum was monitored at 540 nm and the PL spectrum used 251 nm excitation.

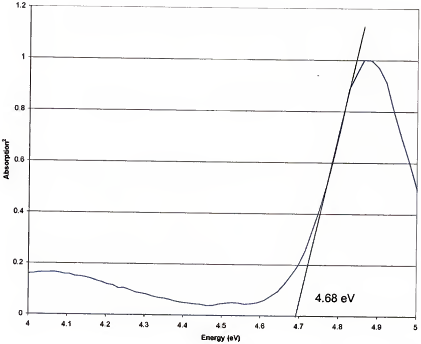

Figure 4-15. PLE spectrum for Zn_2GeO_4:Mn plotted as excitation^2 versus energy. The excitation band extrapolates to 4.68 eV on the energy axis.

4.3.2.4 Electroluminescence behavior

The brightness versus voltage behavior for UF Zn_2GeO_4:Mn samples annealed at a range of temperatures is shown in Figure 4-16. The curves labeled "fresh" were measured when the devices were first operated. The curves labeled "aged" were operated at 1 kHz, 40 V above threshold for 20 minutes. All samples were processed under otherwise identical conditions with a thickness of ~470 nm. The as-deposited and 600°C annealed samples did not show visible emission. The 700°C sample was measurable when fresh and is included in Figure 4-16. After aging this sample, green emission was visible but was below the sensitivity of the spectrophotometer. In Table 4-4 the B_{40} and V_{th} values for these samples are summarized. Figure 4-17 shows the EL emission spectrum from a Zn_2GeO_4:Mn sample. The emission peak is 540 nm, and the chromaticity values are CIE x = 0.293 and CIE y = 0.672.

Table 4-4. B_{40} and V_{th} values for the RTA series shown in Figure 4-16.

	Fresh		Aged	
RTA Temperature (°C)	B_{40} (cd/m^2)	V_{th}	B_{40} (cd/m^2)	V_{th}
As deposited	-	-	-	-
600	-	-	-	-
700	0.3	164	-	-
800	23.3	144	15.1	172
850	75.3	134	38.7	169

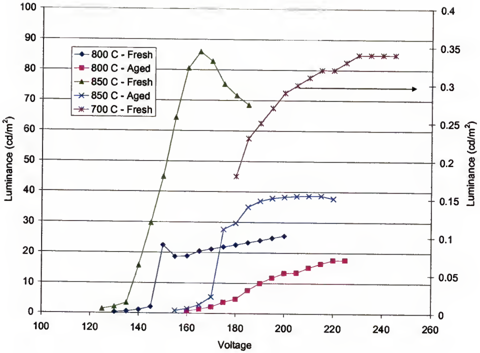

Figure 4-16. Brightness-voltage (B-V) curves for Zn_2GeO_4:Mn samples annealed at a range of temperatures. Aging was performed at 1 kHz, 40 V above threshold for 20 minutes.

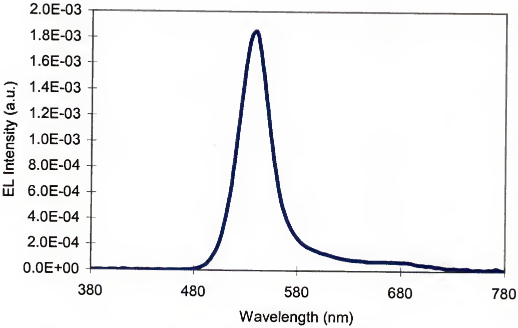

Figure 4-17. EL emission spectrum from a Zn_2GeO_4:Mn sample.

4.3.2.5 Transient electrical measurements

Optical and electrical characterization was performed on three Zn_2GeO_4:Mn samples having the standard device structure with ATO bottom insulator, BTO top insulator, and with phosphor layer thicknesses of 200, 480, and 700 nm, respectively. These measurements were performed using the Sawyer-Tower bridge circuit using a 30 nF sense capacitor. The external charge and external voltage were used to calculated internal charge, external current, internal (dissipative) current, and phosphor field as described in Section 2.8. The measurements were recorded on fresh devices and after aging at 1 kHz and V_{40} for 20 minutes.

The external charge-voltage (Q-V) behavior for the three devices is shown in Figures 4-18 – 4-23. Figures 4-18, 4-20, and 4-22 show data for the fresh 200 nm, 480 nm, and 700 nm devices at various maximum applied voltages. Figures 4-19, 4-21, and 4-23 show Q-V data for the same devices, respectively, after aging.

Internal charge vs. phosphor field (Q-F_p) data were extracted from the Q-V data shown above according to the procedure discussed in Section 2.8. As discussed previously the selection of the phosphor and insulator capacitance is critical to the characteristics of these plots. Figure 4-24 shows the Q-F_p behavior for the fresh 480 nm sample using the DC capacitance values for the phosphor and insulator, which were 11 nF/cm^2 and 29 nF/cm^2, respectively. The DC measured phosphor capacitance for all samples were all similar to those found from the sub-threshold slope of the Q-V plot. This was not the case for the insulator capacitance values.

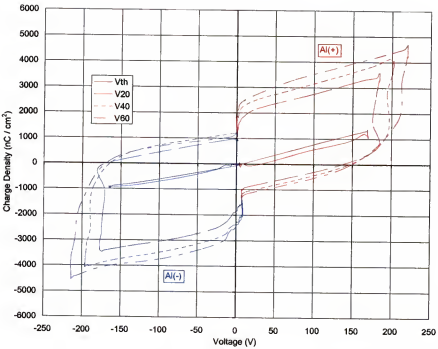

Figure 4-18. Q-V data for the fresh 200 nm Zn_2GeO_4:Mn device at various applied maximum voltages.

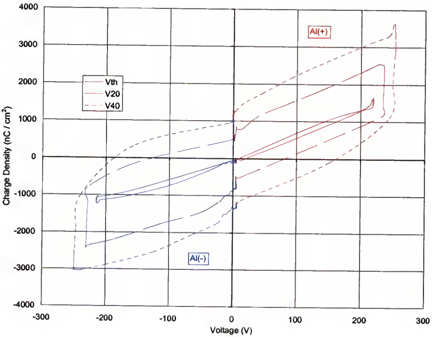

Figure 4-19. Q-V data for the 200 nm Zn_2GeO_4:Mn device at various applied maximum voltages after aging at 1 kHz, V_{40}, for 20 minutes.

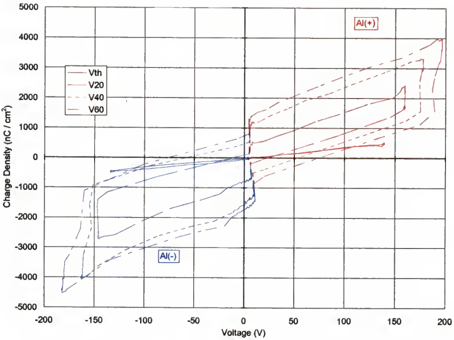

Figure 4-20. Q-V data for the fresh 480 nm Zn_2GeO_4:Mn device at various applied maximum voltages.

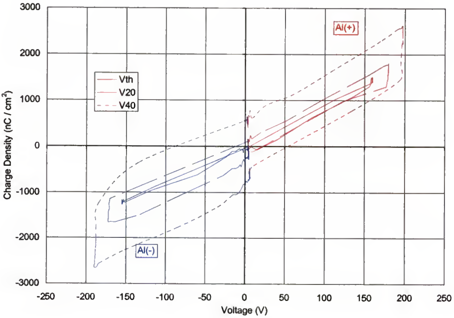

Figure 4-21. Q-V data for the 480 nm Zn_2GeO_4:Mn device at various applied maximum voltages after aging at 1 kHz, V_{40}, for 20 minutes.

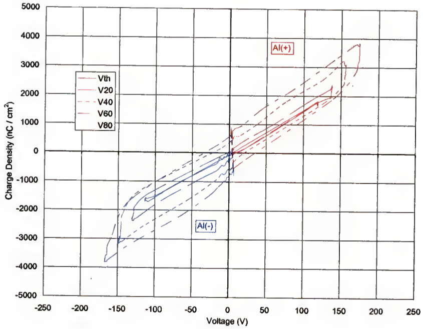

Figure 4-22. Q-V data for the fresh 700 nm Zn_2GeO_4:Mn device at various applied maximum voltages.

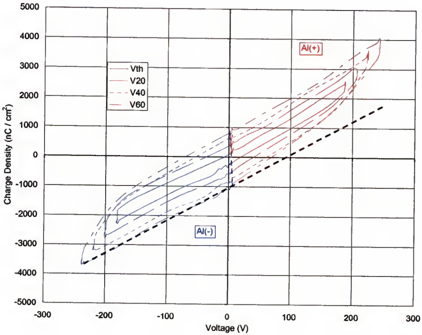

Figure 4-23. Q-V data for the 700 nm Zn_2GeO_4:Mn device at various applied maximum voltages after aging at 1 kHz, V_{40}, for 20 minutes. The dashed line indicates the slope normally used to define the total device capacitance.

Idealized Q-F_p plots were obtained by using the capacitance of the phosphor and insulators as adjustable variables. For Figures 4-25 – 4-30 an arbitrarily large insulator capacitance value was used (in this case 10,000 nF/cm^2) such that the ratio of $(C_i + C_p)/C_i \approx 1$. The exception is the 700 nm sample after aging. For this sample a value of $C_i = 150$ nF/cm^2 was used. Figures 4-25, 4-27, and 4-29 show data for the fresh 200 nm, 480 nm, and 700 nm devices at various maximum applied voltages. Figures 4-26, 4-28, and 4-30 show Q-F_p data for the same devices, respectively, after aging at 1 kHz, V_{40}, for 20 minutes.

Note that Figure 4-24 and 4-27 use the same Q-V data, except that in 4-24 the physical capacitances are used while in 4-27 these are adjustable parameters. For reasons discussed in section 4.4.3.1, the more realistic behavior is that shown in Figure 4-24. However the idealized curves are often better for observing features such as turn-on and curvature caused by space charge. For these reasons the phosphor field and voltage values calculated using the physical insulator capacitance value, 29 nF/cm^2 (the values used for Figure 4-24), are given in Table 4-5. These are believed to be more realistic values. However all other plots use the idealized capacitance values, and the quantitative values should not be extracted from them (this holds true for Figures 4-31 – 4-35 as well).

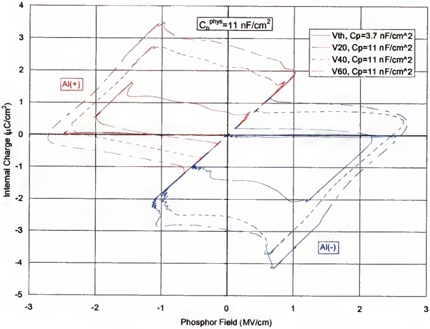

Figure 4-24. Q-F_p data for the fresh 480 nm sample using the measured DC capacitance values for above-threshold data.

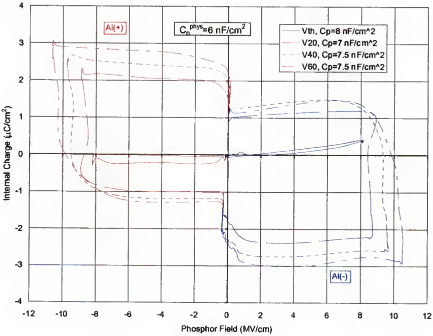

Figure 4-25. Q-F_p data for the fresh 200 nm sample using the idealized capacitance values, C_i = 10,000 nF/cm^2.

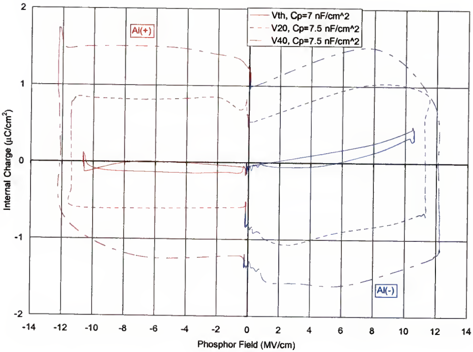

Figure 4-26. Q-F$_p$ data for the 200 nm sample using the idealized capacitance values, $C_i = 10{,}000$ nF/cm^2, aged at 1 kHz, V_{40} for 20 minutes.

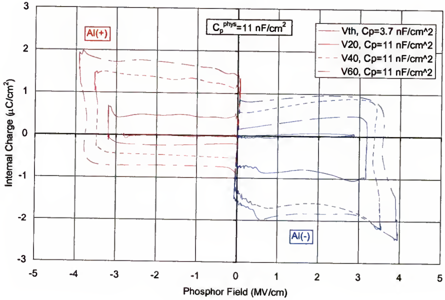

Figure 4-27. Q-F$_p$ data for the fresh 480 nm sample using the idealized capacitance values, $C_i = 10{,}000$ nF/cm^2.

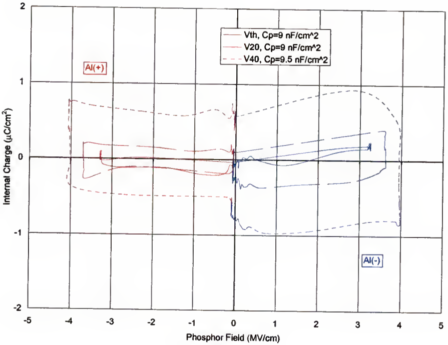

Figure 4-28. Q-F_p data for the 480 nm sample using the idealized capacitance values, C_i = 10,000 nF/cm^2, aged at 1 kHz, V_{40} for 20 minutes.

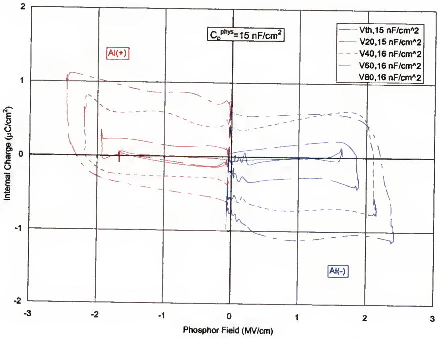

Figure 4-29. Q-F_p data for the fresh 700 nm sample using the idealized capacitance values, C_i = 10,000 nF/cm^2.

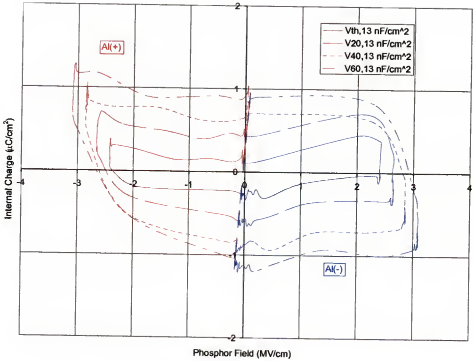

Figure 4-30. Q-F_p data for the 700 nm sample using the idealized capacitance values, $C_i = 150$ nF/cm^2, aged at 1 kHz, V_{40} for 20 minutes.

Table 4-5. Maximum calculated phosphor field values using the measured DC insulator capacitance value of $C_i = 29$ nF/cm^2.

Phosphor thickness (nm)	V_{40} maximum calculated phosphor field (MV/cm)	V_{40} voltage (V)	Phosphor voltage (V)
200	7.5	199	150
480	2.4	170	115
700	1.0	152	70

The same Q-F_p data are shown in Figures 4-31 and 4-32 for fresh and aged samples, respectively, comparing the different thicknesses for the phosphor layer. These data show that the phosphor field increases dramatically for thinner phosphor layers, both for the fresh and the aged samples.

Figures 4-33, 4-34 and 4-35 show Q-F_p data for the 200, 480, and 700 nm samples, respectively, comparing the fresh and aged Q-F_p behavior. Voltages were chosen for these plots which showed similar amounts of conduction charge. The data show that aging results in reduces space charge, larger phosphor field, and reduced internal charge. The leakage charge observed in the fresh samples is almost eliminated for the aged samples by an amount that nearly accounts for all of the reduction in conduction charge. The 700 nm sample shows the effects of aging to a lesser degree than the thinner samples.

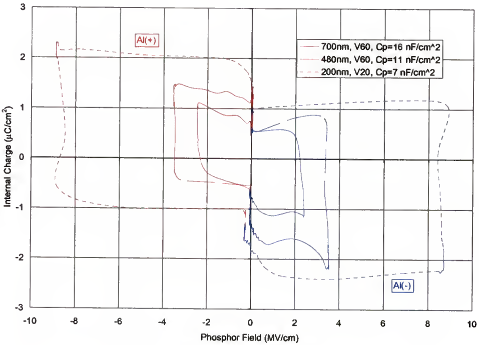

Figure 4-31. Q-F_p data for fresh samples with different phosphor layer thickness.

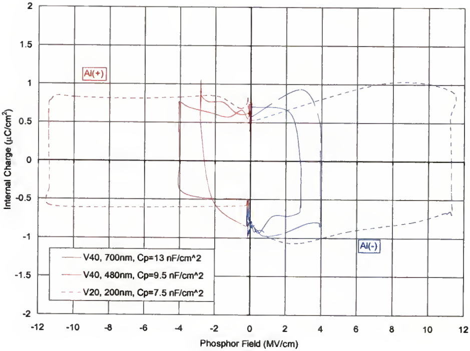

Figure 4-32. Q-F_p data for aged samples with different phosphor layer thickness.

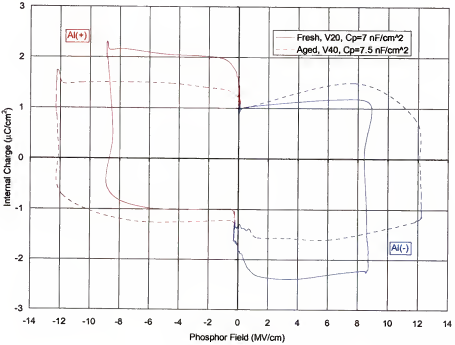

Figure 4-33. Comparison of the fresh and aged Q-F_p behavior for the 200 nm sample.

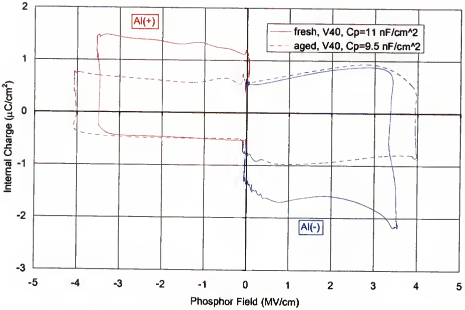

Figure 4-34. Comparison of the fresh and aged Q-F_p behavior for the 480 nm sample.

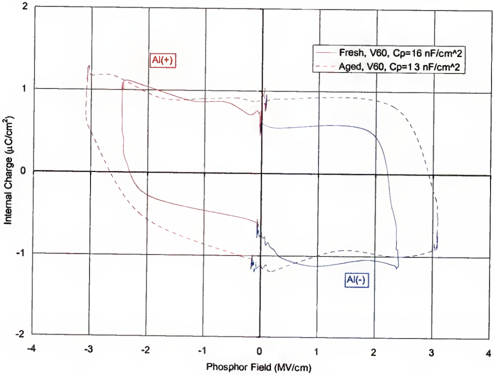

Figure 4-35. Comparison of the fresh and aged Q-F_p behavior for the 700 nm sample.

4.3.2.6 Transient optical measurements

The data in this section were collected from the 480 nm sample while fresh. Transient monochromatic light emission from the sample was collected at various wavelengths, allowing spectra to be generated as a function of time. This was done for each polarity of the applied voltage.

EL decay behavior is shown in Figure 4-36 for various emission wavelengths using the aluminum-positive (Al(+)) polarity, or that in which the ATO/Zn_2GeO_4:Mn interface acts as the cathode. The analogous data for the Al(-) polarity are shown in Figure 4-37.

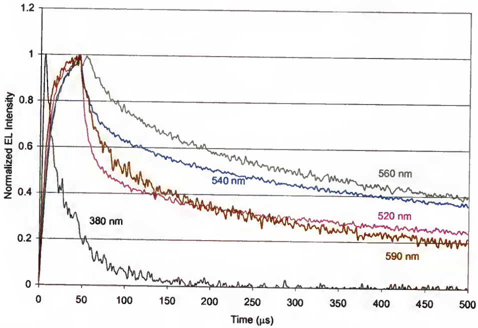

Figure 4-36. EL decay behavior at various wavelengths for the Al(+) polarity.

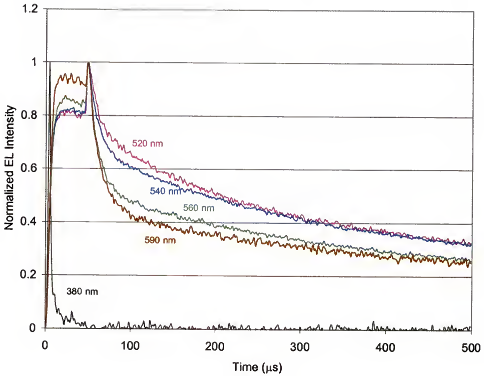

Figure 4-37. EL decay behavior at various wavelengths for the Al(-) polarity.

Figure 4-38 shows the EL emission spectrum for the Al (+) polarity taken 6μs after the voltage pulse is applied, which is close to the time that the voltage reaches its maximum value (point C in Figure 2-11). Two features should be noted. (1) The maximum intensity occurs at 540 nm, expected for the $^4T_1 \rightarrow {}^6A_1$ transition of Mn^{2+} in Zn_2GeO_4:Mn. (2) There is a low intensity, broad band from ~360-430 nm. It is not clear whether other small features, such as the peak at 450 nm and the shoulder at 515 nm, are real. Figure 4-39 shows the same type of data for the Al(-) polarity. This spectrum shows primarily Mn^{2+} emission also, with more intense low wavelength emission that is more broad than for the Al(+) polarity.

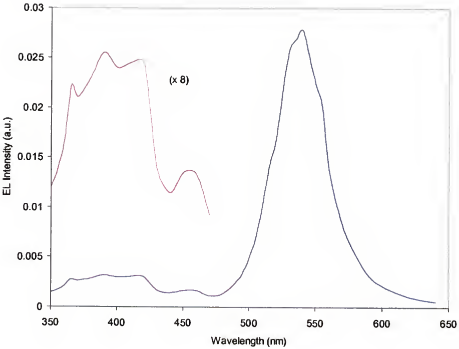

Figure 4-38. EL emission spectrum measured 6 μs after the Al(+) voltage pulse is applied, approximately when the voltage pulse reaches its maximum value.

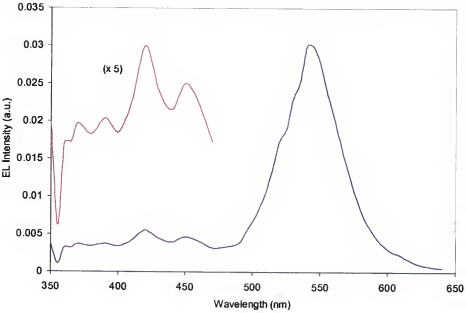

Figure 4-39. EL emission spectrum measured 6 μs after the Al(-) voltage pulse is applied, approximately when the voltage pulse reaches its maximum value.

Figure 4-40 shows the EL decay behavior (L(t)) of 390 nm emission for both polarities, with the time behavior of the internal current for the Al(-) polarity shown for comparison. The current behavior for the Al(+) polarity was different in magnitude but not significantly different in shape. The spectra show that for the Al(-) polarity the emission essentially follows the current as a function of time, indicating very fast decay. The Al(+) polarity on the other hand shows exponential decay with a time constant of 30 μs.

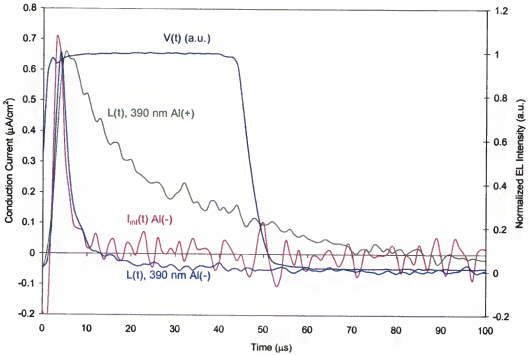

Figure 4-40. EL decay behavior for 390 nm emission for each polarity relative to the time behavior of the internal current.

Spectra were generated from the decay data at various wavelengths. Figure 4-41 shows normalized spectra measured 100 and 500 μs after the Al(+) voltage pulse, or ~60 μs and 460 μs after the voltage pulse ends. The spectra are nearly identical, which was also observed for the Al(-) pulse (not shown). Figure 4-42 shows spectra measured 10, 40, 70, and 100 μs after the onset of the Al(+) voltage pulse, and Figure 4-43 shows the analogous spectra for the Al(-) pulse. Figure 4-42 shows that for the Al(+) pulse, the 10 and 40 μs spectra have maxima at ~538 nm with a shoulder on the high energy side at ~530 nm. For the 70 and 100 μs spectra the maximum has shifted to ~543 nm. All spectra have a low energy shoulder at ~555 nm. For the Al(-) spectra in Figure 4-43, the 530 nm shoulder is missing. The 70 and 100 μs spectra are similar to those for the Al(+) polarity. The 10 μs and 40 μs have maxima at 545 nm and a larger low energy tail than the 70 and 100 μs spectra. Figure 4-44 shows the same spectra given in Figure 4-42 measured 40 and 100 μs after the onset of the Al(+) voltage pulse. The difference between the spectra corresponds to the rapid decay after the voltage pulse seen in Figure 4-36. The difference is plotted in Figure 4-42. The 100 μs and the "difference" spectra were fit with a Gaussian approximation on an energy scale, also shown in the Figure. Figure 4-45 shows the corresponding data measured for the Al(-) polarity. The Gaussian fit parameters are given in Table 4-6.

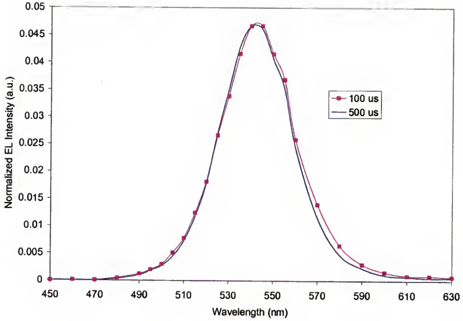

Figure 4-41. Normalized EL emission spectra for the Al(+) polarity measured 100 μs and 500 μs after the 40 μs voltage pulse is applied.

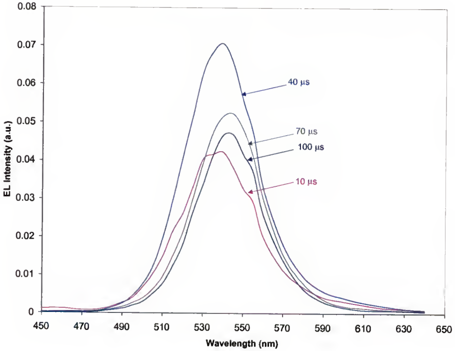

Figure 4-42. EL emission spectra for the Al(+) voltage pulse measured 10, 40, 70, and 100 μs after the onset of the voltage pulse.

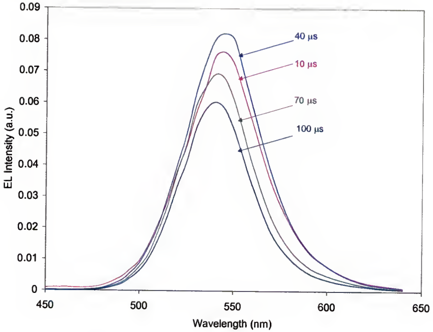

Figure 4-43. EL emission spectra for the Al(-) voltage pulse measured 10, 40, 70, and 100 μs after the onset of the voltage pulse.

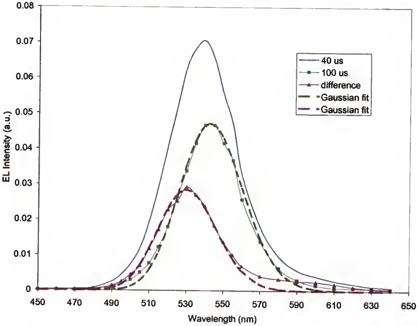

Figure 4-44. EL emission spectra for the Al(+) voltage pulse measured 40 and 100 μs after the onset of the voltage pulse. The difference between the spectra and Gaussian fits on an energy scale for the 100 μs and "difference" spectra are shown.

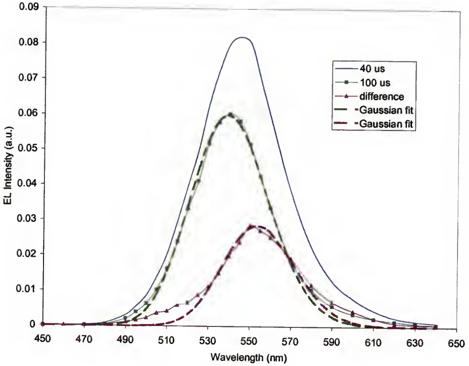

Figure 4-45. EL emission spectra for the Al(-) voltage pulse measured 40 and 100 μs after the onset of the voltage pulse. The difference between the spectra and Gaussian fits on an energy scale for the 100 μs and "difference" spectra are shown.

Table 4-6. Gaussian fit parameters used for the curves in Figure 4-44 and 4-45.

	Al(+)		Al(-)	
Mean, μ (nm)	530	543	539	554
Std. dev., σ (nm)	16	17	20	17
Relative Intensity	0.59	1	1	0.42

Figure 4-46 shows 540 nm emission from the fresh 700 nm sample driven at 1 kHz and V_{40}, along with the applied voltage.

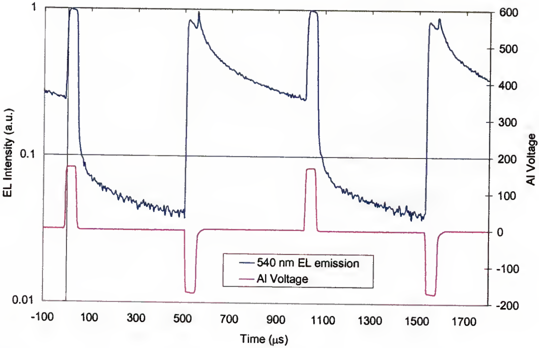

Figure 4-46. 540 nm EL emission from the fresh 700 nm sample and the applied voltage vs. time.

Figure 4-47 and 4-48 show L(t), i_{cond} (t), and V(t) data measured using a variable capacitor bridge circuit and collecting only 520 nm emission. The waveform in Figure 4-47 has a frequency of ~47 Hz while that in Figure 4-48 has a frequency of ~700 Hz.

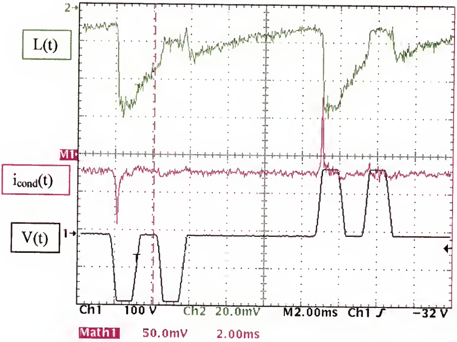

Figure 4-47. 520 nm EL emission, conduction current, and applied voltage vs. time for low frequency double voltage pulses.

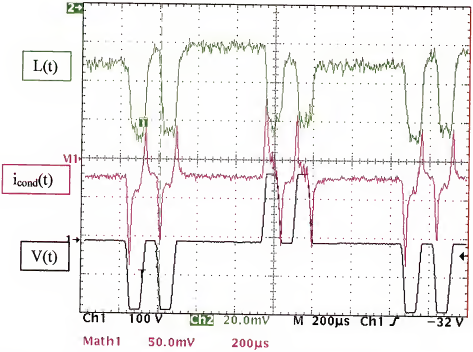

Figure 4-48. 520 nm EL emission, conduction current, and applied voltage vs. time for high frequency double voltage pulses.

4.4 Discussion

4.4.1 Planar Parameter Study

There are several overriding points to take from the parameter study. First, the best device performance was found to be $B_{40} = 74$ cd/m^2, $E_{40} = 0.19$ lm/W, and CIE x = 0.300 and y = 0.664. There were brighter samples and more efficient samples, but this device showed the best overall performance in terms of brightness, efficiency, and color coordinates. Second, the diffuse scattering values of <1% for all samples showed that this performance was achieved even with very poor outcoupling efficiency. As discussed in Section 2.6.5, it has been shown that surface roughness can increase optical outcoupling by as much as an order of magnitude [46]. Empirically, when a test dot was electrically excited, the sample brightness at the edges of the glass was rather bright relative to the test dot. Noting that the sample edge is large compared to the area of the test dot, these two observations indicate good internal efficiency from the devices. Third, all Planar samples were evaluated when fresh. It was at the end of the study that the aging behavior was noticed and addressed.

In terms of the processing parameters, the study revealed a rather robust process. Within the processing parameter window studied, performance was reasonable regardless of conditions as long as some amount of oxygen was added to the sputter gas. The second critical parameter was the annealing temperature. The best performance was achieved at higher annealing temperatures, shown in Figure 4-8, the highest being 860°C. This was the limit of the substrate and underlayers, since glass softening was observed even at 860°C, and ITO is known to degrade above this temperature. Whether a maximum was reached in terms of either anneal time or temperature is not known. The reason for the robustness of the process is suspected to be that the deposited films are amorphous (discussed in the following section) and therefore only stoichiometry is a critical parameter during deposition.

4.4.2 UF Study

4.4.2.1 Structural, morphological, and chemical analysis

The processing of sputter targets revealed that after firing ZnO, GeO_2, and MnO_2 powders at 800°C, complete conversion to Zn_2GeO_4:Mn had taken place. This was indicated by x-ray diffraction data as well as by bright green luminescence under UV excitation (data not shown). After sintering a pressed pellet at 1050°C for 6 hours the same was still true, as evidenced by the x-ray diffraction and PL spectrum for the sintered pellet shown in Figures 4-9 and 4-10.

X-ray diffraction (XRD) of sputtered samples annealed over a range of RTA temperatures was performed, shown in Figure 4-11. The data reveal that the as-deposited and 600°C annealed films are amorphous. Above 600°C crystallization takes place, consistent with the data in Figure 4-8 which show increased EL brightness in samples annealed above this temperature. For the crystalline samples the primary diffraction peak was the (006) peak. There appears to be some diffraction from the (113) plane as well, though this overlaps strongly with a substrate peak making analysis difficult. The (006) plane diffraction indicates preferred orientation of the films along the c-axis. Possible diffraction from the (113) plane indicates grains slightly mis-oriented from the c-axis. Other peaks that appear with higher annealing temperature belong to the (220), (410), (333), and (416) planes of Zn_2GeO_4:Mn. The FWHM of the (006) peak was analyzed as a function of RTA temperature, and this data, shown in Figure 4-12, revealed gradually improving crystallinity with higher annealing temperature, consistent with the increase in EL brightness. The onset of crystallinity is consistent with that reported previously [48, 100, 119], but the XRD diffraction patterns are inconsistent with those presented by Bondar et al. [119] for sputtered Zn_2GeO_4:Mn films. Their films showed only slight (001) texturing and generally better crystallinity.

SEM microscopy was performed on the temperature series. The cause for the poor optical outcoupling from the devices is evident in the smooth surfaces and rounded features on the films. Across the range from 600°C to 850°C, no significant change in morphology is observed despite the fact that the XRD shows crystallization taking place in this range. This indicates that even though crystallization takes place, ionic mobility is still low.

Energy-dispersive spectroscopy (EDS) shows little or no change in stoichiometry across the temperature series. The Zn/Ge ratio of ~1 (Table 4-3) deviated significantly from the expected ratio of ~2. The cause for this discrepancy is not clear, but there are several possibilities. Measurement error in EDS is certainly a consideration. The smooth film surface is a benefit to obtaining accurate results. However the thin film thickness can distort the ZAF correction routine. The accelerating voltage was 15 kV for a film thickness of 570 nm. As there are no heavy elements in the film, the electron beam penetration depth is expected to be well into the ATO layer beneath the phosphor. But the EDS data in Table 4-3 for the 850°C annealed sample were collected at the angle shown in the micrograph in Figure 4-13d, resulting in an effectively larger film thickness. The change from a Zn/Ge ratio of 0.99 to 1.05 is in the direction towards a stoichiometric film, so some of the error may be a penetration depth effect. Still, the deviation from stoichiometry is large and the samples appear to be zinc deficient to some extent. The starting material was prepared as stoichiometric Zn_2GeO_4, and neither ZnO nor GeO_2 would be expected to volatilize under the temperatures and atmospheres used in processing. If deviation from stoichiometry were to take place it would be expected to be during the sputtering process. The film XRD data show the presence of Zn_2GeO_4, and no other phases are evident.

Given this information there are several possibilities regarding the incorporation of excess germanium.

1. Measurement error: As discussed previously this is not likely to account for all of the deviation from stoichiometry.
2. Non-stoichiometric Zn_2GeO_4: This is doubtful, since $ZnGeO_3$ is also a stable phase, but was not observed by XRD.
3. Phase segregation of Zn_2GeO_4 and GeO_2: This option seems the most likely, but there is no direct evidence for it. The GeO_2 could be present but undetectable by XRD as an amorphous phase, since the ATO layer beneath the phosphor is partially amorphous. How the amorphous phase would be incorporated is not clear. Long scale segregation is unlikely because of low mobility at the annealing temperatures used. The low mobility is inferred from the lack of surface texture combined with the empirical evidence that brighter films are obtained at higher annealing temperatures. Short scale segregation, in the form of small Zn_2GeO_4 grains with amorphous GeO_2 incorporated at the grain boundaries is a possibility. How this would affect the performance of the device is not known.

4.4.2.2 Optical characterization

The sputtered, annealed films show PL emission spectra characteristic of the $^4T_1 \rightarrow {}^6A_1$ transition from Mn^{2+} in Zn_2GeO_4. The PL and PLE spectra are shown in Figure 4-14. Mn^{2+} usually shows multiple excitation bands due to higher-lying excited states such as those seen in Figure 2-18 [44], but these are not observed, so it is clear that Mn^{2+} is not excited directly. Therefore the good PL intensity (no quantitative value is available) indicates efficient charge transfer from the lattice to Mn^{2+}. The high energy excitation band is attributed to band gap absorption. There is a very efficient lower energy excitation band with a maximum at 310 nm, corresponding to 615 meV below bangap energy. This band is most easily attributed to either a charge transfer transition or to a defect state. Mn^{2+} is not a particularly good candidate to exhibit metal-to-ligand charge transfer or ligand-to-metal charge transfer, since it is not stable in either a Mn^{1+} or Mn^{3+} valence, but this is not out of the question. This suggests that the excitation band is due to a defect state, corresponding to 615 meV from either the conduction or valence band. The charge transfer efficiency from this band to the Mn^{2+} excited state is nearly as good as that from the band gap.

The band gap excitation band was used to approximate a traditional absorption spectrum. This is justified because the band gap excitation band is strong. By plotting the absorption (excitation) squared versus energy as in Figure 4-15 and extrapolating the data to the energy axis, the optical band gap of the Zn_2GeO_4:Mn was found to be 4.68 eV. This band gap is within the range suitable for an EL host material. For example, SrS is an excellent phosphor host with a band gap of 4.2 eV [31].

In comparison to the PL spectrum, an EL emission spectrum for an Zn_2GeO_4:Mn device is shown in Figure 4-17. The EL spectrum has a maximum ~539 nm, compared to 535 for the PL spectrum. In addition there is an extended broad emission to the low energy side of the peak.

4.4.2.3 Electroluminescence characterization

The B-V characteristics of the temperature series are shown in Figure 4-16. The as-deposited, 600°C annealed, and 700°C aged samples were all too dim to measure. Aging or burn-in of the sample during operation of the devices can be seen due to the time required to perform the measurements. The aging results in the downward slope of the B-V curve for the 850°C annealed sample. The B_{40} and V_{th} values are given in Table 4-4. The best brightness value was 75 cd/m^2 measured from the sample annealed at 850°C, but this brightness reduced to 39 cd/m^2 with aging. Several trends are seen. The B_{40} value increases dramatically with RTA temperature. The threshold voltage also decreases slightly with RTA temperature. Firnally, the threshold voltage increases and B_{40} decreases as the sample is aged.

4.4.3 Electroluminescent Behavior of Zn_2GeO_4:Mn Devices

Other than the emission spectrum shown in Figure 4-17 and the B-V characteristics of the devices shown in Figures 4-2 and 4-16, the electroluminescent behavior of the Zn_2GeO_4:Mn devices are anomalous with regard to "traditional" behavior in every sense. In Section 4.4.3.1 the electrical data presented in Section 4.3 is discussed, and in Section 4.4.3.2 the optical data is discussed. Finally in Section 4.4.3.3 a model to explain the behavior is presented.

4.4.3.1 Electrical behavior

Q-V analysis. Q-V data for the thickness series is shown in Figures 4-18 to 4-23. There are a number of observations that should be pointed out.

1. The 200 nm sample shows significant dynamic space charge when fresh (Figure 4-18). This is evidenced by the curvature above threshold (the B-C-D portion of the curve according to the labeling scheme in Figure 2-14). The Q-V curve is relatively symmetric for the Al(+) and Al(-) pulses.
2. Upon aging (Figure 4-19), the space charge is significantly reduced. Also, there is no traditional "turn-on" such as the B-C portion of Figure 2-14, where the Q-V slope increases below V_{max}. Instead there is little conduction charge below V_{max}, especially at lower values of V_{max}, and all of the conduction charge is relaxation charge (the C-D portion of Figure 2-14). The leakage charge seen in the fresh devices (E-F in Figure 2-14) is almost eliminated, and the device is still rather symmetric.
3. The fresh 480 nm sample (Figure 4-20) shows a large amount of dynamic space charge. The shape of the curves is similar for both pulses, but there is more conduction charge and more leakage charge for the Al(-) pulse. The slope of the Q-V data for V_{th} is significantly lower than the slope for higher values of V_{max}. There is no explanation for this observation.
4. After aging (Figure 4-21), the changes are similar to those seen for the 200 nm sample. The biggest difference is that there is still more conduction charge and some leakage charge for the Al(-) pulse.
5. The behavior of the 700 nm sample (Figure 4-22) is significantly different than the other two samples. For the fresh device the Al(-) pulse shows little or no dynamic

space charge, and for the highest applied voltage, V_{80}, begins to show traditional turn-on below V_{max}. For the Al(+) pulse there is evidence of space charge, and the conduction charge does not occur completely at V_{max}, i.e. the turn on is more traditional. There is little or no leakage charge for the Al(+) pulse, while there is some leakage charge for the Al(-) pulse.

6. After aging the 700 nm sample (Figure 4-23), the Al(+) pulse shows conduction charge beginning at very low voltages, especially for high values of V_{max}. This is demonstrated in Figure 4-23 by the dashed line, which shows that the Al(-) slope is higher than the slope that is usually indicative of the device capacitance. This is not the case for the Al(-) polarity, which shows more traditional Q-V behavior with sub-threshold charge, conduction charge, and leakage charge all evident.

The general shape of the Q-V curves seen in Figures 4-18 to 4-23, namely a single slope up to V_{max} and a nearly vertical slope above that, is very similar to the Q-V curves shown by Keir et al. [137]. In this paper the anomalous Q-V behavior is shown to be due to leaky insulators. However, for the Zn_2GeO_4:Mn devices, the pulse width was varied from 15-125 μs to show that there is not a significant DC component to the conduction current. This data is not shown, but the result can be seen from the $i_{int}(t)$ data in Figure 4-40. It is evident from these data that the conduction current occurs over a short period, but the onset of conduction occurs only when the applied voltage reaches a maximum. From these observations leaky insulators are not suspected.

Q-F_p analysis. Q-F_p data for the thickness series is shown in Figures 4-24 to 4-30. Before discussing the Q-F_p data it is important to reiterate the effects of the selection of C_I and C_p values. These values are normally taken from the slopes above and below turn-on of the Q-V data. As mentioned previously, in the case of the Zn_2GeO_4:Mn samples the Q-V data is anomalous in that there is generally no traditional Q-V turn-on. Instead there is a single slope up to V_{max}, and the conduction charge then results in a nearly vertical slope. Therefore to achieve the most ideal Q-F_p plots, a very large value of C_I must be used. For ease of analyzing such aspects as space charge and field clamping this approach was taken for Figures 4-25 to 4-30. However a more realistic picture of the internal charge-phosphor field behavior is that seen in Figure 4-24, which uses the measured DC insulator capacitance value of 29 nF/cm^2. The reason that this plot is more realistic is that for the ideal curve, a vertical slope is obtained for the B-C portion of the plot (notation refers to Figure 2-14). However in the Zn_2GeO_4:Mn devices the field increases to a maximum with little conduction current. When conduction current flows at V_{max} there should be a concomitant decrease in the phosphor field since the applied voltage is no longer increasing. In section 2.8 it was shown that the calculated phosphor field is dependent on the insulator value used, and by comparing Figure 4-24 ($C_i = 29$ nF/cm^2) with Figure 4-27 (same input data, $C_i = 10{,}000$ nF/cm^2) it can be seen that the field values obtained by using the idealized plots are not accurate. For this reason the ideal Q-F_p curves are shown in Figures 4-25 to 4-30, but the V_{40} maximum field values calculated using $C_i = 29$ nF/cm^2 are shown in Table 4-6.

Analysis of the Q-F_p plots in Figures 4-25 to 4-30 show several interesting trends.

1. For the 200 nm device, both fresh (Figure 4-25) and aged (Figure 4-26), the lack of field clamping is apparent by the increasing phosphor field during the conduction portion of the curve. Both fresh and aged devices are relatively symmetric, and show gradual turn-on only at higher voltages. The fresh device shows more

dynamic space charge, apparent by the field curvature during conduction, and more leakage charge. With aging, the phosphor field increases while the amount of conduction and leakage charge decreases.

2. The same observations are true for the 480 nm device (Figures 4-27 and 4-28), except that the Al(-) polarity results in more conduction charge as well as more leakage charge.
3. The fresh 700 nm device (Figure 4-29) shows a small amount of dynamic space charge, but only on the Al(-) polarity. There is also a larger amount of conduction and leakage charge for this polarity. The change in conduction charge and phosphor field with aging is less significant than for the thinner devices.

Table 4-6 shows several trends in electrical behavior. As the phosphor thickness increases, the phosphor field decreases, the threshold voltage decreases, and the average voltage across the phosphor decreases. A decreased threshold voltage is normally attributed to increased space charge [85, 129].

Mechanism for anomalous conduction behavior. There is no clear mechanism to explain the anomalous Q-V/Q-F_p behavior of the Zn_2GeO_4:Mn devices. The following explanation is proposed. In "normal" devices, the rate of conduction charge (i_{int}) is limited by the voltage slew rate and field clamping. This leads to conduction current which begins during the voltage ramp and lasts several μs (see Chapter 3). Figures 4-25 to 4-30 show that there is no field clamping taking place in the Zn_2GeO_4:Mn devices. But there must be some reason why the conduction current lasts for several μs, even after the voltage is no longer increasing (see Figure 4-40). One explanation is a broad distribution of defect states which will empty due to tunneling or thermally-assisted tunneling over a range of applied voltages. This would be expected to result in a sub-V_{max}, or traditional, turn-on but this is not observed. Another explanation is that the device response time is inherently slower than the voltage ramp time. This might be expected for a phosphor layer with a higher resistance and higher capacitance than other phosphors, leading to a large RC time constant. Using the measured DC device capacitance (0.9 nF) and a rough estimate of the device resistance from current-voltage data (25 kΩ, data not shown) the RC time constant expected is 20 μs. This is about an order of magnitude off the measured decay time of the conduction current in Figure 4-40 of ~3 μs. Given the uncertainty in the resistance estimate this explanation is a possibility, and is the only explanation currently available.

4.4.3.2 Optical behavior

Many of the optical properties of the Zn_2GeO_4:Mn were found to be anomalous as well. As mention previously, the PL and EL spectra in Figures 4-14 and 4-17 exhibit the expected emission from the $^4T_1 \rightarrow {}^6A_1$ transition of Mn^{2+}. The ~1 ms decay time for 540 nm excitation in Figure 4-46 is additional evidence of this. The EL decay is similar to the ZnS:Mn decay observed in Chapter 3 in the non-exponential nature of the decay. All of the transient optical measurements shown are measured from the 480 nm UF sample while fresh, but limited measurements using Planar samples showed similar results.

Figures 4-36 and 4-37 show normalized decay behavior for selected wavelengths for the Al(+) and Al(-) polarities, respectively. Several features are worth noting. There is a short wavelength component to the emission with a fast decay time. This will be discussed in more detail shortly. There is a rapid decay of the520-590 nm emission which lasts ~20 μs, and the magnitude of this decay is different for different wavelengths.

The onset of emission is very different in character for the two polarities. The Al(+) polarity shows a slower build up and no trailing edge emission. The Al(-) has a much more rapid build up for all wavelengths and shows a sharp trailing edge peak upon removal of the voltage pulse. This trailing edge intensity is different in magnitude for different wavelengths. The rapid decay seen for the Al(+) polarity is also seen in this polarity, but the magnitude of it for the various wavelengths is not consistent between the two polarities.

The nature of the various portions of these decay curves are analyzed here in more detail.

"Blue flash" luminescence. At the onset of EL emission there is a significant short-wavelength component. Spectra collected 6 μs after the onset of the voltage pulse, which corresponds to the intensity maximum of 380 nm emission in Figures 4-36 and 4-37, are shown in Figures 4-38 and 4-39 for the Al(+) and Al(-) polarity voltage pulses, respectively. These spectra show primarily green emission characteristic of Mn^{2+} along with a short wavelength component. The short wavelength component of the Al(-) pulse is more intense relative to the Mn^{2+} intensity compared to the Al(+) pulse and is broadly distributed across the blue/near UV, while for the Al(+) pulse there appears to be a more structured band centered at ~390 nm. This emission is similar to the well known "blue flash" emission observed in ZnS:Mn devices [22]. The ZnS:Mn devices have a broad, fast-decay component centered at ~425 nm that is attributed to interband transitions. The same explanation is given for the short wavelength component of Zn_2GeO_4:Mn. The decay of 390 nm emission for both polarities is shown relative to the internal current in Figure 4-40. The decay time of ~20 μs for the Al(+) polarity is consistent with that of donor-acceptor pair recombination in ZnS phosphors [4]. The 390 nm emission from the Al(-) pulse follows almost exactly the conduction current flow. The proposed reason for this will be discussed in Section 4.4.3.3. The blue/UV emission is attributed to e-h pair recombination associated with defect states, which reduce the energy of the transition. One implication of this emission is that it implies that electrons reach sufficient energy to create e-h pairs of at least the energy seen in the spectra, corresponding to 3.54 eV, and probably higher. A second implication is that there must be a region in the phosphor layer with a low enough electric field to allow e-h pair recombination without field quenching. The coexistence of these seemingly contradicting assertions is discussed shortly.

Long decay emission. The long-lived emission was initially attributed to Mn^{2+} emission, but this should be verified. To do this, emission spectra which were measured 100μs and 500 μs after the onset of the voltage pulse were compared. Even at 100 μs the fast-decay component is essentially gone, so that only the long-lived component is remaining. These two spectra are shown in Figure 4-41, which shows that the two spectra are virtually identical and similar to the EL emission spectra of the devices. This indicates that the long-lived component is a single type of transition with a single decay behavior across the broad emission band. It was mentioned earlier that the decay time and decay behavior is consistent with Mn^{2+} decay in ZnS ACTFEL devices. This is sufficient evidence to attribute the long-lived component to the ${}^4T_1 \rightarrow {}^6A_1$ transition of Mn^{2+}.

The intermediate decay behavior, which occurs near the removal of the voltage pulse, is more complicated. The short decay time indicates that there is one of three things taking place. There is either a) another type of Mn^{2+} center with a fast time constant, b) a non-radiative process from the Mn^{2+} excited state competing with the radiative Mn^{2+} relaxation, or c) there is another type of decay process entirely.

The first possibility, a second type of Mn^{2+} center, can be essentially ruled out by the observation that the decay time of 10's of μs is far too short for the spin- and parity-forbidden Mn^2 transition. The local crystal/ligand field and symmetry can affect this decay, but that would be expected to drastically affect the transition energy as well.

The second possibility, non-radiative recombination, cannot be ruled out as quickly. The decay curve is not too different from that of Mn in ZnS where it was shown [45] that at high excitation densities, excited state interaction can result in non-radiative relaxation of the excited state. This could take place in Zn_2GeO_4:Mn, but it is not expected to be as significant as the fast decay that is seen. This is due to the fact that a) the average Mn-Mn distance in 1.5 Zn% Zn_2GeO_4 is very similar to that in 0.6 Zn% ZnS, b) the excitation density in Zn_2GeO_4 should not be as large as that in the more efficient ZnS device, and c) the rapid decay is even more severe than that for Mn^{2+} in ZnS shown by Benoit. Further evidence against this interpretation is given in the next paragraph.

The third possibility is that there is some other type of recombination center. Neglecting the possibility that the rapid decay may be due to an unintentional impurity may be premature, but it would otherwise be due to some type of e-h pair recombination. Unfortunately the emission spectrum prior to the rapid decay is very similar to the Mn^{2+} emission (see Figures 4-42 and 4-43), making analysis more difficult. Given that the emission is in the green portion of the spectrum the e-h pair would necessarily be involved with some type of defect state. The spectral distribution at several moments in time both during and after the voltage pulse are shown in Figures 4-42 and 4-43 for the Al(+) and Al(-) polarities, respectively. These figures show a red shift for the Al(+) polarity and a blue shift for the Al(-) polarity. The emission spectrum before and after rapid decay and the difference between them is shown for each polarity in Figures 4-44 and 4-45. The difference between these spectra can be used as an approximation for the fast-decay component, but by no means assures that the decay is radiative. These emission bands were fit on an energy scale with a Gaussian approximation, also shown in Figures 4-44 and 4-45. The fit parameters, given in Table 4-5, show that for both polarities the 100 μs spectrum can be fit with similar parameters centered at ~540 nm. As mentioned, this is attributed to Mn^{2+} emission. The fast decay component for the Al(+) polarity is centered at ~530 nm, while that for the Al(-) is centered at ~554 nm. This evidence also serves to refute both of the possibilities mentioned previously.

The "blue flash" emission is attributed to band-edge e-h pair recombination. The long-lived decay component which dominated the emission spectrum is attributed to Mn^{2+} emission. Considering the decay time and polarity-dependent spectral shifts, the fast-decay component is attributed to defect-related e-h pair recombination.

4.4.3.3 Device process model

The observations regarding the electrical and optical behavior of the Zn_2GeO_4:Mn devices have been incorporated into a phenomenological model for device operation. The model is a device in which only one interface efficiently injects high energy electrons into the phosphor, creating an asymmetric space charge distribution. This model and the supporting evidence will be explained in this section from the standpoint of device processes.

The foundation of the model is that the BTO/Zn_2GeO_4:Mn interface acts as an efficient cathode (Al(-) polarity) while the ATO/Zn_2GeO_4:Mn interface does not. Evidence supporting this comes primarily from L(t) measurements. A higher excitation rate is seen from the emission build up in Figure 4-37 as compared to Figure 4-36. In addition, Figure 4-46 clearly shows that only the Al(-) polarity efficiently excited the long-lived Mn^{2+} emission.

The Q-V and Q-F_p data clearly demonstrate dynamic space charge. This phenomenon was discussed in more detail in Chapter 3, but results when space charge is created and annihilated on a time scale smaller than that of the excitation waveform. This type of space charge is evident in SrS:Ce ACTFEL devices, and in these devices it is usually attributed to trap-to-band ionization of point defects [26, 69, 71-73, 138]. Because of the similar nature of the Q-V/Q-F_p curvature to that in SrS:Ce, this mechanism is also proposed here. It has been discussed that this type of space charge develops preferentially near the cathodic interface. It follows that the interface that provides the more energetic electron energy distribution would result in a larger amount of ionization and therefore space charge.

The sample thickness would have a dramatic influence on the energy band profile through the film. It is proposed that for a thick phosphor layer, the creation of a large amount of space charge near one cathode results in a broad low field region near the anode. For a thin phosphor layer the low field region would not be exist. This assertion is validated by the phosphor field data shown in Table 4-6, which demonstrates that a thicker phosphor layer results in a smaller average phosphor field. This concept is shown schematically in Figure 4-49.

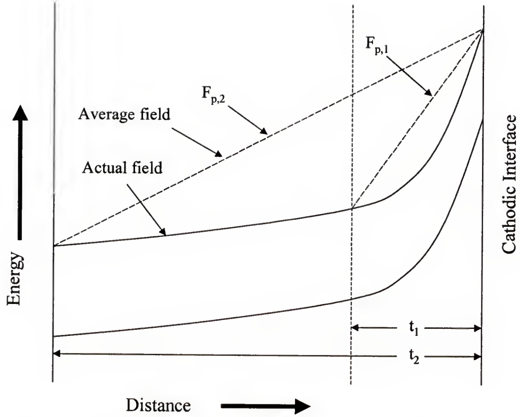

Figure 4-49. Schematic energy band diagram showing the smaller average phosphor field for a thicker phosphor layer exhibiting dynamic space charge.

Given the asymmetric band bending and electron energy distribution, the following processes are proposed to explain the observed data:

When the Al(-) excitation pulse is applied, electrons tunnel at ballistic energies into the conduction band of the phosphor. They achieve sufficient energy to cause impact ionization of the lattice and/or trap levels, resulting in sub-gap emission, or "blue flash" emission (processes 1 and 3 in Figure 4-50). Direct impact excitation of Mn^{2+} is also possible and efficient (process 2 in Figure 4-50). As trap-to-band ionization takes place, space charge is generated which enhances the local field near the cathode. This field quenches the blue flash emission, as shown experimentally in Figure 4-40, and results in a broad low field region near the anode. These processes are shown schematically in Figure 4-50.

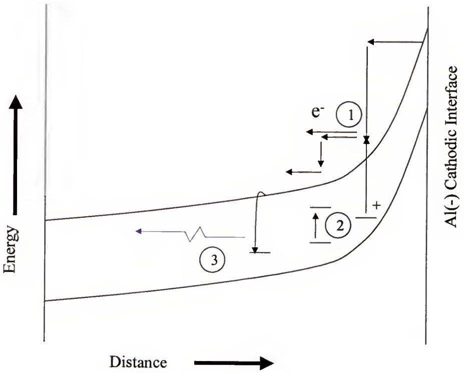

Figure 4-50. Schematic diagram showing EL processes for the Al(-) polarity in Zn_2GeO_4:Mn devices.

When the Al(-) excitation pulse is removed, there is an opposing field due to the conduction current. The opposing field is larger for this polarity since the magnitude of conduction charge is larger. The field lines would show a minimum within the phosphor layer, spatially located where positive charge is trapped near the BTO/Zn_2GeO_4:Mn cathode. A small number of electrons in shallow traps are then able to move back towards the potential minimum, resulting in radiative recombination with holes generated by trap-to-band ionization or hole re-capture. This results in the short-lived trailing edge emission seen at the end of the Al(-) pulse in Figure 4-46. Additional leakage charge occurs between the voltage pulses, but is too small to detect and therefore may result in radiative or non-radiative recombination.

When the Al(+) excitation pulse is applied, the processes which take place depend significantly on the phosphor layer thickness. For a thin phosphor layer the low field region does not exist so the processes are similar to those from the Al(-) polarity. However for a thick phosphor layer the field lines are relatively flat near the cathode and electrons are not injected as efficiently as for the Al(-) polarity. In fact it is shown later that the electrons may be sourced from bulk phosphor traps for this polarity rather than the iterface. This means that a smaller number of electrons reach energies large enough to ionize defects or impact excite Mn^{2+} centers. These two observations are demonstrated by the data in Figures 4-38 and 4-46. In addition, because of the lower field and lack of space charge generation the blue flash emission is not quenched by high fields, as demonstrated by Figure 4-40. The primary emission mechanism is e-h pair recombination between the low energy conduction electrons and the positive charges in the lattice. For an intermediate phosphor thickness an intermediate situation takes place where some Mn^{2+} excitation occurs along with the e-h pair recombination. Upon removal of the Al(+) excitation pulse, little out of the ordinary takes place. This is because a smaller amount of conduction charge is observed and the Al(-) interface has sufficiently deep traps to store the electrons until the Al(+) excitation pulse is applied. Therefore the leakage charge that results in the trailing edge emission for the Al(-) polarity is not observed.

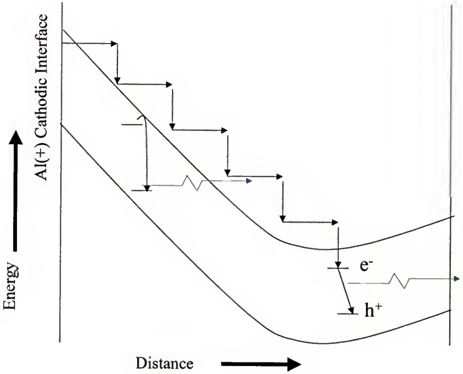

Figure 4-51. Schematic diagram showing the EL processes which occur during the Al(+) excitation pulse in Zn_2GeO_4:Mn devices.

The data in Figure 4-48 shows L(t) and $i_{cond}(t)$ data for a 700 Hz waveform which uses two consecutive pulses of the same polarity. This data is very unusual in that consecutive same-polarity pulses are normally observed to result in little or no excitation [3]. However the data support the above model. The second-pulse emission is not observed in Figure 4-47, which uses identical conditions as Figure 4-46 except that the frequency is 47 Hz. It has been shown that space charge decays over time between pulses if charge carriers are not efficiently trapped [26]. Figure 4-47 shows that at 47 Hz there is no trailing edge current, indicating that electrons are efficiently trapped.

However at 700 Hz, the large trailing edge current indicates that a) a large amount of space charge was created which leaves an opposing field and b) the electrons are not sufficiently trapped and can conduct due to the field created by space charge. In this case the electrons may simply be trapped in the phosphor, not at interface states. The reason that second-pulse emission is usually not seen is that the opposing field remaining due to stored charge prevents significant conduction charge [3]. However in the 700 Hz data, there is little or no stored charge and second-pulse excitation is allowed.

The quenching of Mn^{2+} by the Al(+) pulse as seen in Figure 4-46 is very unusual. The L(t) data in Figure 4-47 is even more unusual. This shows that a second pulse of the same polarity at low frequency also results in quenching of Mn^{2+} emission. But the emission appears to be restored upon removal of the pulse as if the quenching had not taken place. There is no clear mechanism to explain the observations. Quenching of Mn^{2+} emission could be explained by a field quenching process in which the excited state becomes ionized by tunneling of the electron into the conduction band. This is not expected because the Mn^{2+} excited state has been demonstrated by the data here to be stable under high fields under most circumstances. The rapid decay behavior does not resemble what is expected by an excited state interaction process [45]. The explanation that seems most probable is that there is some type of defect state that is nearly resonant with the Mn^{2+} excited state. The e-h pair recombination spectra in Figures 4-44 and 4-45 demonstrate that there are certainly defect states available in the forbidden gap. The quenching of Mn^{2+} emission occurs most severely for the 700 nm sample, as shown in Figure 4-46, and only for the Al(+) polarity. As mentioned previously the Mn* excited centers are believed to be near the BTO/Zn_2GeO_4:Mn interface where positive charge is trapped. It is proposed that when electrons are available to annihilate the positive charge some sort of energy transfer mechanism occurs between Mn* and nearly resonant states, quenching Mn^{2+} emission. Upon removal of the field, under certain circumstances it is plausible that deep traps nearly resonant with the Mn* excited state could transfer the energy back to Mn^{2+}, restoring the Mn^{2+} emission, as seen in Figure 4-46. It was disscussed previously that there appears to be a significant amount of e-h pair recombination taking place at energies similar to the Mn^{2+} transition, so this explanation seems plausible.

CHAPTER 5
CONCLUSIONS

5.1 Co-Doping of ZnS:Mn with K and Cl

The effects of K and Cl doping on ZnS:Mn ACTFEL devices fabricated by RF magnetron sputtering were investigated and compared to devices without co-doping. The codoping was shown to increase the B_{40} brightness value from 379 cd/m^2 to 581 cd/m^2 and the E_{40} efficiency value from 1.18 lum/W and 1.92 lum/W at 60 Hz for the best devices. This corresponds to an improvement of 53% in B_{40} and a 62% in E_{40}. The effects of conduction charge, optical outcoupling, radiative efficiency, and interface microstructure were shown to have a small effect on performance relative to the observed improvement. Transient opto-electrical measurements were used to show that the improved performance comes primarily from a 75% increase in Mn^{2+} excitation efficiency. By studying the electrical behavior of the co-doped devices as compared to the undoped devices, it was determined that there is a reduced amount of static space charge in the co-doped films, resulting in a larger average field, increased excitation efficiency, and increased charge multiplication. The reduced space charge is attributed to the addition of shallow charge compensating V_{Zn}-Cl_S acceptor complexes and Cl_S donor point defects, both of which reduce the effects of V_{Zn} deep hole traps. It is postulated that there is sufficient electron multiplication or donor ionization to create a situation in which the current limit is set by the phosphor resistance rather than a capacitance or density of states.

5.2 Zn_2GeO_4:Mn devices

RF magnetron sputter deposited Zn_2GeO_4:Mn thin film phosphors were evaluated in ACTFEL devices. The best devices achieved B_{40} and E_{40} values of 74 cd/m^2 and 0.19 lm/W, respectively, with saturated green chromaticity of CIE x = .300 and y = 0.664. Optical data reveal efficient charge transfer from the lattice and a 615 meV sub-band gap defect state to the Mn^{2+} ion. Unique transient optical and electrical behavior is observed, and a phenomenological model is presented to explain it. The electrical and optical properties are strongly dependent on the thickness of the phosphor layer. This is attributed to efficient charge injection only from the top phosphor/insulator interface and an unusually large amount of dynamic space charge near the cathode. The dynamic space charge creates an extended low field region for thick devices which allows efficient electron-hole pair recombination. Unusual transient electrical behavior is attributed to slow charge injection dominated by the RC time constant of the phosphor layer. Fast band-edge recombination, deep level electron-hole pair recombination, and near-resonant energy transfer to and from the Mn^{2+} excited state are observed and are used to explain the anomalous transient optical behavior.

CHAPTER 6
FUTURE WORK

6.1 Co-Doping of ZnS:Mn with K and Cl

Co-doping of ZnS:Mn with alkali halides is potentially a commercially important process, and warrants further investigation. In addition, a better understanding of the mechanisms could provide insight into how other phosphor systems could achieve better performance using similar processes. The following areas of work are proposed. The first three suggested areas were investigated in a cursory fashion and should be more thoroughly studied:

1. A statistical study of co-doping effects. The results which were presented and analyzed in this work come from a limited number of samples. Experience shows that device properties can vary significantly from sample to sample, and a better understanding of the universal effects of co-doping would aid the understanding of the mechanisms involved. For example, increased brightness, efficiency, and threshold voltage are seen consistently, but the magnitude differs. Other effects are not necessarily as consistent and these should be investigated.
2. A comparison of the effects of co-doping on sputtered films versus evaporated or ALE ZnS:Mn films. The primary reason is that most previous work on ZnS:Mn devices uses one of these other deposition methods, and the properties of the devices are better known and better understood. This would provide a better understanding for the baseline properties of the control samples. In addition, improving the

performance for samples grown by these methods is more likely to have a commercial impact.

3. A detailed comparison of the effects of different alkali halide compounds. This study would provide more insight into the role of the cation and anion. For example, while evidence shows that potassium is likely to be an interstitial defect, this may not be true for smaller cations such as sodium or lithium. Different defect levels could also change the performance of the devices. The limited results already obtained are given in Appendix A.
4. Hall conductivity and photoconductivity measurements. Incorporating these measurements into the previously mentioned analyses should provide a better understanding of the electrical nature of the dopants, as compared to SIMS measurements which only provide a physical concentration.
5. Incorporating the proposed defect levels into state-space device models. This would help to confirm or refute the proposed mechanisms. To date, the state space approach has yielded accurate simulations for ZnS:Mn devices grown by evaporation or ALE.
6. Investigation of "blue-flash" luminescence. This would give some insight into possible excitonic recombination processes.

6.2 Zn_2GeO_4:Mn devices

Zn_2GeO_4-based devices have shown interesting and unique characteristics. But more importantly, have shown promise as a commercially useful EL phosphor. However, more work is necessary to provide a better evaluation of this phosphor. The following areas of research are suggested:

1. Analysis of efficiency similar to the one used for ZnS:Mn. This would lead to several new areas of study such as:

- Improve outcoupling efficiency. The most obvious approach would be to modify the surface morphology.
- Study/improve radiative efficiency. PL lifetime studies would indicate the significance of competing non-radiative processes, and processing conditions can be used to improve the performance
- Improve excitation efficiency. This is especially significant for thicker phosphor layers where efficient Mn excitation only occurs for one polarity. A study using different insulator materials or modified interface properties could improve the device performance considerably.

2. Optimization study (not necessarily using sputter deposition) which includes the following:

- Mn doping concentration
- Zn_2SiO_4:Mn alloying
- Improved surface morphology
- Investigation of the $(Zn,Be)_2(Ge,Si)O_4$:Mn system. (This would be recommended only after significant progress has been made in understanding the device properties and requirements, due to the dangerous effects associated with Be.)

3. Investigate transient electrical and optical behavior using non-trapeziodal waveforms. This would require a high voltage amplifier used in tandem with an arbitrary wavefore generator. Understanding the unique electrical behavior in these devices would be aided by using the technique employed by Neyts, *et al.* which employs

triangular voltage pulses rather than the trapezoidal pulses used during this work. In addition, preliminary studies using unconventional pulse sequences, such as consecutive same-polarity pulses, showed unusual behavior which should be investigated further. Most importantly, using a slow voltage slew rate would help to confirm or deny the explanation that the unusual Q-V characteristics are due primarily to the RC time constant of the device.

4. Measure emission spectra of undoped devices. These studies should give insight into the possibility that the short-lived decay comes not from energy transfer away from Mn, but rather from another source such as e-h pair recombination.
5. Electron paramagnetic resonance (EPR) measurements would help give some insight into the symmetry and surroundings of the Mn^{2+} ion. This would help to confirm or deny the possibility that the unusual emission behavior is related to different Mn^{2+} symmetries.
6. Coerced-field measurements. This refers to the types of measurements discussed in Ch. 3 regarding the elimination of space charge by constant illumination with sub-band gap radiation during operation. This would reduce band bending and give more insight into the role of the low-field regions in allowing electron-hole pair recombination to occur.

LIST OF REFERENCES

1. Infinite Technologies, Inc., *Global Liquid Crystal Display/Flat Panel Display Market Strategies 2001*. Singapore: Asia Info Tsushinsha Ptc. Ltd., 2000.

2. Candescent Technologies Corp., website, www.candescent.com

3. Ono, Y.A., *Electroluminescent Displays*. Singapore: World Scientific Publishing Co., 1995.

4. Tannas, L.E., *Flat-Panel Displays and CRT's*. New York: Van Nostrand Reinhold, 1985.

5. Rack, P.D. and P.H. Holloway, Materials Science and Engineering. R21 *4* (1998) 171-219.

6. Castellano, J.A., *Handbook of Display Technology*. San Diego: Academic Press, Inc., 1992.

7. Lyons, E., *David Sarnoff*. New York: Harper & Row, 1966.

8. Sobel, A., *Flat-Panel Displays*, in *Electro-Optical Displays*, M.A. Karim, Editor. 1992, Marcel Dekker, Inc.: New York. p. 121-185.

9. Matsumoto, S., *Electronic Display Devices*. New York: John Wiley & Sons, 1984.

10. Gudden, B. and R. Pohl, Z. Phys. 2 (1920) 192.

11. Lossev, O.W., Telegrafia i Telefonia. 18 (1923) 61.

12. Destriau, G., J. Chim. Phys. 34 (1937) 462.

13. Destriau, G., J. Chim. Phys. 33 (1936) 587.

14. Destriau, G., J. Chim. Phys. 34 (1937) 327.

15. Henisch, H.K., *Electroluminescence*. International Series of Monographs on Semiconductors. Vol. 5. New York: Pergamon Press, 1962.

16. Mach, R. and G.O. Mueller, Semiconductor Science and Technology. 6 (1991) 305-323.

17. T. Inoguchi, et al., SID 74 Digest. (1974) 84-95.

18. S. Mito, et al., SID 74 Digest International Symposium. (1974) 86-87.

19. King, C.N., J. SID. 4 *3* (1996) 153-156.

20. Minami, T., Display and Imaging. 8, suppl. (1999) 83-93.

21. Duan, L., T. Xiao, and A.H. Kitai, Proceedings of the 15th International Display Research Conference. (1997).

22. Smith, D.H., J. Lumin. 23 (1981) 209-235.

23. Wager, J.F. and P.D. Keir, Annu. Rev. Mater. Sci. 27 (1997) 223-248.

24. Bringuier, E., J. Appl. Phys. 75 *9* (1994) 4291-4312.

25. Sun, S.-S. and R. Khormaei, SPIE vol. 1664 High-Resolution Displays and Projection Systems. (1992) 48-55.

26. Hitt, J.C., J.P. Bender, and J.F. Wager, Crit. Rev. in Solid State and Mat. Sci. 25 *1* (2000) 29-85.

27. Bringuier, E., J. Appl. Phys. 66 (1989) 1314.

28. Vincent, G., A. Chantre, and D. Bois, J. Appl. Phys. 50 (1979) 5484.

29. Rosencher, E., V. Mosser, and G. Vincent, Phys. Rev. B. 29 (1984) 1135.

30. Kobayashi, S., J.F. Wager, and A. Abu-Dayah, EL 92 Proceedings. (1992) 234.

31. Dur, M., S.M. Goodnick, R. Redmer, M. Reigrotzki, N. Fitzer, and M. Stadele, Physica B. 272 (1999) 295-298.

32. Mach, R. and G.O. Mueller, Journal of Crystal Growth. 101 (1990) 967-975.

33. Dur, M., S. Goodnick, S.S. Pennathur, J.F. Wager, M. Reigrotzki, and R. Redmer, J. Appl. Phys. 83 *6* (1998) 3176-3185.

34. Bringuier, E. and K. Bhattacharyya, Semicond. Sci. Technol. 10 (1995) 1065-1075.

35. Cleary, B.A., P.D. Keir, J.C. Hitt, T.K. Plant, J.F. Wager, and S.S. Sun, Third International Conference on the Science and Technology of Display Phosphors. (1997).

36. Thompson, T.D. and J.W. Allen, J. Phys. C: Solid State Phys. 20 (1987) L499-L503.

37. Bringuier, E., J. Appl. Phys. 70 *8* (1991) 4505-4512.

38. Baraff, G.A., Phys. Rev. 128 *6* (1962) 2507-2517.

39. Douglas, A.A., J.F. Wager, D.C. Morton, J.B. Koh, and C.P. Hogh, Appl. Phys. Lett. 63 *2* (1993) 231-233.

40. Brennan, K., J. Appl. Phys. 64 *8* (1988) 4024-4030.

41. Bhattacharyya, K., S.M. Goodnick, and J.F. Wager, J. Appl. Phys. 73 *7* (1993) 3390-3395.

42. Mach, R. and G.O. Mueller, Physica Status Solidi (a). 81 (1984) 609-623.

43. Bringuier, E., J. Appl. Phys. 67 *11* (1990) 7040-7044.

44. Blasse, G. and B.C. Grabmaier, *Luminescent Materials*. Berlin: Springer-Verlag, 1994.

45. Benoit, J., P. Benalloul, C. Barthou, S. Casette, and J.C. Soret, Physica Status Solidi (a). 122 (1990) 427-438.

46. Holloway, P.H. and S.L. Jones, Journal of Surface Analysis. 3 *2* (1998) 226-231.

47. Stevens, H., personal communication, 2000.

48. Keir, P.D., *Dissertation*, Electrical and Computer Engineering, Oregon State University, 1999.

49. Kim, H. and C.M. Gilmore, J Appl Phys. 86 *11* (1999) 6451-6461.

50. Honda, S., A. Tsujimoto, M. Watamori, and K. Oura, J Vac Sci Tech A. 13 *3* (1995) 1100-1103.

51. Suzuki, M., Y. Maeda, M. Muraoka, S. Higuchi, and Y. Sawada, Mater Sci Eng B. 54 (1998) 43-45.

52. Jia, Q.X., J.P. Zheng, H.S. Kwok, and W.A. Anderson, Thin Solid Films. 258 (1995) 260-263.

53. Kamei, M., Y. Shigesato, I. Yasui, N. Taga, and S. Takaki, J Non-Crystalline Solids. 218 (1997) 267-272.

54. Laux, S., N. Kaiser, A. Zoller, R. Gotzelmann, H. Lauth, and H. Bernitzki, Thin Solid Films. 335 (1998) 1-5.

55. Tominaga, K., T. Ueda, T. Ao, M. Kataoka, and I. Mori, Thin Solid Films. 281-282 (1996) 194-197.

56. Utsumi, K., O. Matsunaga, and T. Takahata, Thin Solid Films. 334 (1998) 30-34.

57. Aduodija, F., H. Izumi, T. Ishihara, and H. Yoshioka, Appl Phys Lett. 74 *20* (1999) 3059-3061.

58. Paine, D.C., T. Whitson, D. Janiac, R. Beresford, and C.O. Yang, J Appl Phys. 85 *12* (1999) 8445-8450.

59. Kobayashi, H. and S. Tanaka, J. SID. 4 *3* (1996) 157-163.

60. Mauch, R.H., J. SID. 5 *3* (1997) 173-178.

61. Ballato, J., J.S. Lewis, and P. Holloway, MRS Bulletin. 24 *9* (1999) 51-56.

62. Ylilammi, M., Acta Polytech. Scand. Appl. Phys. Ser. 170 (1990) 149-152.

63. Zeinert, A., P. Benalloul, J. Benoit, C. Barthou, J. Dreyhsig, and H.E. Gumlich, Journal of Applied Physics. 71 *6* (1992) 2855-2862.

64. Sun, S.-S., E. Dickey, J. Kane, and P.N. Yocom. in *1997 International Display Research Conference*. 1997.

65. Troppenz, U., B. Huttl, U. Storz, P. Kratzert, K.O. Velthaus, S.-S. Sun, and R.T. Tuenge, Extended Abstracts of the Fourth Intl Conf on the Sci and Tech of Display Phosphors / the Ninth Intl Workshop on Inorg and Org Electroluminescence. (1998) 187-190.

66. Lide, D.R. and H.P.R. Frederikse, eds. *CRC Handbook of Chemistry and Physics.* 78th ed. , ed. D.R. Lide and H.P.R. Frederikse. 1997, CRC Press: Boca Raton.

67. Sawyer, C.B. and C.H. Tower, Physical Review. 35 (1930) 269-273.

68. Neyts, K.A. and P.D. Visschere, J. Appl. Phys. 68 *8* (1990) 4163-4171.

69. Neyts, K., IEEE Transactions on Electron Devices. 43 *9* (1996) 1343-1350.

70. Neyts, K.A., D. Corlatan, P.D. Visschere, and J.V.d. Bossche, J. Appl. Phys. 75 *10* (1994) 5339-5346.

71. Ohmi, K., S. Inoue, S. Tanaka, and H. Kobayashi, Appl. Phys. Lett. 64 *25* (1994) 3464-3466.

72. Ohmi, K., K. Ishitani, S. Tanaka, and H. Kobayashi, Appl. Phys. Lett. 67 *7* (1995) 944-946.

73. Neyts, K. and E. Soininen, IEEE Transactions on Electron Devices. 42 *6* (1995) 1086-1092.

74. Myers, R. and J.F. Wager, J. Appl. Phys. 81 *1* (1997) 506-510.

75. Shih, S., P.D. Keir, J. Hitt, and J.F. Wager, Appl. Phys. Lett. 69 *13* (1996) 1921-1923.

76. Shih, S., P.D. Keir, J.F. Wager, and J. Viljanen, J. Appl. Phys. 78 *9* (1995) 5775-5781.

77. Zhai, Q., *Dissertation*, Materials Science and Engineering, University of Florida, 1999.

78. Busse, W., H.-E. Gumlich, A. Geoffroy, and R. Parrot, Phys. Stat. Sol. (b). 93 (1979) 591.

79. Yamaga, S., A. Yoshikawa, and H. Kasai, Journal of Crystal Growth. 86 (1988) 252-256.

80. Neumark, G.F., Mater Sci Eng. R21 (1997) 1-46.

81. Watkins, G.D., J Cryst Growth. 159 (1996) 338-344.

82. Watkins, G.D., Solid State Communications. 12 (1973) 589-592.

83. Georgobiani, A.N., R.G. Maev, Y.V. Ozerbov, and E.E. Strumban, Phys. Stat. Sol. (a). 38 (1976) 77-83.

84. Vlasenko, N.A., M.M. Chumachkova, Z.L. Denisova, and L.I. Veligura, J. Crystal Growth. 216 (2000) 249-255.

85. Hitt, J.C., P.D. Keir, J.F. Wager, and S.S. Sun, J. Appl. Phys. 83 *2* (1998) 1141-1145.

86. Tessaro, G. and P. Mascher, Journal of Crystal Growth. 197 (1999) 581-585.

87. Matsuura, K., S. Kishida, and I. Tsurumi, Phys. Stat. Sol. (b). 140 (1987) 347-353.

88. Hauksson, I.S., J. Simpson, S.Y. Wang, K.A. Prior, and B.C. Cavenett, Appl Phys Lett. 61 *18* (1992) 2208-2210.

89. Hermans, J., J. Woitok, J. Geurts, J. Sollner, M. Heuken, H. Stanzl, and W. Gebhardt, J Crystal Growth. 159 (1996) 363-367.

90. Faschinger, W., J Crystal Growth. 159 (1996) 221-228.

91. Walukiewicz, W., J Crystal Growth. 159 (1996) 244-247.

92. Bube, R., *Photoconductivity of Solids*. Huntington, NY: Rob Kreiger Publishing, 1978.

93. Leverenz, H.W., *An Introduction to Luminescence of Solids*. Structure of Matter Series, ed. M.G. Mayer. New York: John Wiley & Sons, Inc., 1950.

94. Brown, R.A., J. Electrochem. Soc. 118 *6* (1971) 937-942.

95. Kun, Z.K., D. Leskell, P.R. Malmberg, J. Murphy, and L.J. Sienkiewicz, J Electronic Mater. 10 *1* (1981) 287-300.

96. Waldrip, K.E., J.S. Lewis, Q. Zhai, M. Puga-Lambers, M.R. Davidson, and P.H. Holloway, J. Appl. Phys. submitted 9/00 (2000).

97. Binet, L. and D. Gourier, J Solid State Chem. 113 (1994) 420-433.

98. Stodilka, D., A.H. Kitai, and Z. Huang, SID 00 Digest. (2000).

99. Poort, S.H.M., D. Cetin, A. Meijerink, and G. Blasse, J Electrochem Soc. 144 *6* (1997) 2179-2183.

100. Kitai, A.H. in *Extended Abstracts of the Fourth International Conference on the Science and Technology of Display Phosphors and the Ninth International Workshop on Inorganic and Organic Electroluminescence*. 1998. Bend, OR.

101. Minami, T., Y. Kubota, and T. Miyata, Proceedings of the 18th International Display Research Conference. (1998) 1015-1018.

102. Minami, T., Extended Abstracts of the Fourth International Conference on the Science and Technology of Display Phosphors and the Ninth International Workshop on Inorganic and Organic Electroluminescence. (1998) 195-198.

103. Minami, T., T. Kuroi, and S. Takata, J Society for Information Display. 4 *4* (1996) 299-303.

104. Minami, T., S. Takata, Y. Kuroi, and T. Maeno, J Society for Information Display. 4 *2* (1996) 53-58.

105. Minami, T., T. Nakatani, and T. Miyata, J Vac Sci Technol A. 18 *4* (2000) 12341238.

106. Minami, T., Y. Kubota, T. Miyata, and Y. Sakagami, Extended Abstracts of the Fourth International Conference on the Science and Technology of Display Phosphors and the Ninth International Workshop on Inorganic and Organic Electroluminescence. (1998) 319-322.

107. Miyata, T., T. Nakatani, A. Mikami, and T. Minami, Extended Abstracts of the Fourth International Conference on the Science and Technology of Display Phosphors and the Ninth International Workshop on Inorganic and Organic Electroluminescence. (1998) 113-116.

108. Miyata, T., T. Nakatani, and T. Minami, J Lumin. 87-89 (2000) 1183-1185.

109. Minami, T., T. Nakatani, T. Miyata, and T. Shirai, Extended Abstracts of the Fourth International Conference on the Science and Technology of Display Phosphors and the Ninth International Workshop on Inorganic and Organic Electroluminescence. (1998) 105-108.

110. Minami, T., Y. Sakagami, and T. Miyata, Extended Abstracts of the Third International Conference on the Science and Technology of Display Phosphors. (1997) 37-40.

111. Minami, T., Y. Kuroi, H. Yamada, and S. Takata, J Society for Information Display. 6 *1* (1998) 17-22.

112. Minami, T., Y. Kuroi, and S. Takata, J Vac Sci Technol A. 14 *3* (1996) 1736-1740.

113. Minami, T., Y. Kuroi, T. Miyata, H. Yamada, and S. Takata, J Lumin. 72-74 (1997) 997-998.

114. Minami, T., S. Takata, Y. Kuroi, and T. Maeno, SID 95 Digest. (1995) 724-727.

115. Miyata, T., J Lumin. 60-61 (1994) 926-929.

116. Minami, T., T. Miyata, and Y. Sakagami, Surface and Coatings Technology. 108-109 (1998) 594-598.

117. Ouyang, X., A.H. Kitai, and T. Xiao, J Appl Phys. 79 *6* (1996) 3229-3234.

118. Miura, N., T. Ishikawa, T. Sasaki, T. Oka, H. Ohata, H. Matsumoto, and R. Nakano, Jpn J Appl Phys, Pt.2. 31 *1* (1992) L46-L48.

119. Bondar, V., L. Axelrud, V. Davydov, Y. Dubov, S. Popovich, J. Wager, J. Bender, and S.S. Sun. in *6th International Conference on the Science and Technology of Display Phosphors*. 2000. San Diego, CA.

120. Clark, B.L., D.A. Kezler, J.P. Bender, and J.F. Wager. in *6th International Conference on the Science and Technology of Display Phosphors*. 2000. San Diego, CA.

121. Sun, S.-S., personal communication, 1998.

122. Zeinert, A., P. Benalloul, C. Barthou, J. Benoit, J. Dreyhsig, and H.E. Gumlich, Journal of Crystal Growth. 117 (1992) 1016-1020.

123. Zeinert, A., W. Busse, J. Dreyhsig, H.-E. Gumlich, P. Benalloul, and J. Benoit, Acta Polytech. Scand. Appl. Phys. Ser. 170 (1990) 189-192.

124. Mach, R., G.O. Mueller, L. Schrottke, P. Benalloul, and J. Benoit, Acta Polytech. Scand. Appl. Phys. Ser. 170 (1990) 161-169.

125. Keir, P.D., W.M. Ang, and J.F. Wager, J. Appl. Phys. 78 *7* (1995) 4668-4680.

126. Keir, P.D., W.M. Ang, and J.F. Wager, SID Digest. (1995) 476-479.

127. Howard, W.E., O. Sahni, and P.M. Alt, J. Appl. Phys. 53 *1* (1982) 639-647.

128. Douglas, A.A., J.F. Wager, D.C. Morton, J.B. Koh, and C.P. Hogh, J. Appl. Phys. 73 *1* (1993) 296-299.

129. Corlatan, D., K.A. Neyts, and P.D. Visschere, J. Appl. Phys. 78 *12* (1995) 7259-7264.

130. Zhi-Lin, Z., Z. Bu-Xin, Z. Wei-Ming, J. Xue-Yin, L. Zu-Gang, and X. Shao-Hong, Journal of Crystal Growth. 117 (1992) 1012-1015.

131. Bender, J.P. and J.F. Wager, IEEE Transactions on Electron Devices. 47 *5* (2000) 1113-1115.

132. Manar, A., A. Chergui, D. Guennani, D. Ohlmann, T. Cloitre, and R.L. Aulombard, Mater Sci Eng. B43 (1997) 121-125.

133. Waldrip, K.E., M.R. Davidson, J.H. Lee, B. Pathangey, M. Puga-Lambers, K.S. Jones, P.H. Holloway, S.S. Sun, and C.N. King, Display and Imaging. 8, suppl. (1999) 73-82.

134. Zeinert, A., P. Benalloul, J. Benoit, C. Barthou, H.E. Gumlich, and R. Tornqvist. in *13th International Display Research Conference*. 1993. Strasbourg, France: Society for Information Display.

135. Zeinert, A., C. Barthou, P. Benalloul, J. Benoit, and H.-E. Gumlich. in *1994 International Workshop on Electroluminescence*. 1994. Beijing, China: Science Press.

136. Abrikosov, N., V. Bankina, L. Poretskaya, L. Shelimova, and E. Shudnova, *Semiconducting II-VI, IV-VI, and V-VI Compounds*. New York: Plenum Press, 1969.

137. Keir, P.D., H. Le, R.L. Thuemler, J. Hitt, and J.F. Wager, Appl. Phys. Lett. 69 *16* (1996) 2421-2422.

138. Ohmi, K., K. Ishitani, Y. Kashio, S. Tanaka, and H. Kobayashi, Journal of the SID. 5 *2* (1997) 145-149.

APPENDIX A
EFFECTS OF VARIOUS ALKALI HALIDES ON ZnS:Mn DEVICES

Preliminary experiments were performed to investigate the effects of other alkali halides, not just KCl, on ZnS:Mn devices. The experimental procedure was identical to that described in Chapter 3. Only the alkali halide compound was different. The results are shown below.

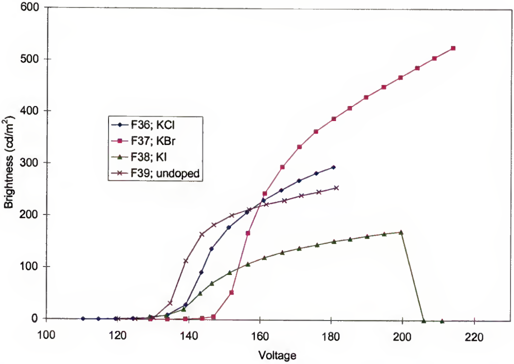

Figure A-1. B-V data for ZnS:Mn ACTFEL devices co-doped with various alkali halide compounds.

Table A-1. Performance data for ZnS:Mn ACTFEL devices co-doped with various alkali halide compounds.

Sample name	Vth	B_{40} (cd/m^2)	E_{40} (lm/W)	CIE x	CIE y	Co-dopant
F36	137.6	287.9	1.568	0.516	0.482	KCl
F37	149.9	431.8	2.086	0.533	0.465	KBr
F38	135.7	144.7	0.762			KI
F39	133.0	242.0	1.220	0.531	0.467	None

APPENDIX B
EL PERFORMANCE DATA FOR Zn_2GeO_4:Mn DEVICES

Run #		Target#	RTA	O2p.p.	O2%	Press	Thick	B40	E40	B40(norm)	CIEx	CIEy	comments
			°C	mTorr		mTorr	Å	Nits	lm/W	nits/400nm			
b7-109	c	245	810	0	0	35	2106	2.4	0.01	4.5536562	0.361	0.591	
b7-109	d	245		0	0	35				0			
b7-110	c	245	810	0	0	35	10286	3.43	0.01	1.3319074	0.389	0.525	
b7-110	d	245	??	0	0	35		7.54	0.01	2.9301964	0.349	0.579	*burnout
b7-111	c	246	810	0	0	35	8175	2.4	0.01	1.1730887	0.396	0.573	
b7-111	d	246		0	0	35				0			
b7-112	c	246	810	0	0	35	9909	4.45	0.01	1.7973559	0.371	0.599	
b7-112	d	246	**	0	0	35		13.7	0.02	5.530326	0.346	0.611	**air,700C,5hrs.,*burnout
b7-113	c	246	810	0	0	35	5652	2.06	0.01	1.4543524	0.406	0.558	
b7-113	d	246	**	0	0	35		9.93	0.02	7.0293701	0.38	0.625	**air,700C,5hrs
b7-114	c	246	810	0	0	35	6749	3.77	0.01	2.2329234	0.355	0.607	
b7-114	d	246	**	0	0	35		5.14	0.02	3.0448955	0.335	0.623	**air,700C,5hrs
b7-115	c	246	810	0	0	50	6243	3.08	0.01	1.975012	0.378	0.595	
b7-115	d	246		0	0	50				0			dead
b7-116	c	245	810	0	0	35	6040	1.37	0	0.9072848	0.408	0.556	
b7-116	d	245		0	0	35				0			
b7-117	c	246	810	1.9	5.5	35	4967	21.2	0.09	17.100866	0.365	0.597	
b7-117	d	246	860	1.9	5.5	35		44.9	0.2	36.132474	0.308	0.629	
b7-118	c	245	810	0	0	35	4399	1.71	0.01	1.5571721	0.415	0.55	
b7-118	d	245	810	0	0	35				0			*not coated (pallet stuck)
b7-119	c	246	810	0.96	2.75	35	3505	26.7	0.11	30.487874	0.285	0.661	
b7-119	d	246	860	0.96	2.75	35		56.5	0.26	64.493581	0.259	0.678	
b7-120	d	245	810	0	0	35		*	*	#VALUE!			*burnout
b7-120	c	245	**	0	0	35	9413	2.74	0.01	#DIV/0!	0.375	0.582	(repeat b7-118, thicker)
b7-121	c	246	810	0.49	1.4	35	4393	31.5	0.14	28.691099	0.342	0.634	
b7-121	d	246	750	0.49	1.4	35		13.7	0.06	12.474391	0.346	0.628	
b7-122	c	246	810	1.4	4.1	35	3325	24	0.09	28.842105	0.306	0.649	

b7-122	d	246	650	1.4	4.1	35		15.1	0.05	18.129323	0.358	0.601		
b7-123	c	246	810	1.9	5.5	35	3063	16.1	0.06	21.021874	0.271	0.665		
b7-123	d	246		1.9	5.5	35				0				
b7-124	c	246	810	1.9	5.5	35	3325	23.6	0.09	28.430075	0.283	0.672	room temp.	
b7-124	d	246	860	1.9	5.5	35		32.5	0.11	39.142857	0.272	0.68	room temp.	
b7-125	a	246	810	1.9	5.5	35				#DIV/0!			static	room temp.
b7-125	e	246	810	1.9	5.5	35				#DIV/0!			static	room temp.
b7-126	c	246	810	0.275	5.5	5	5871	19.9	0.04	13.534321	0.326	0.637	room temp.	
b7-126	d	246	810	0.275	5.5	5		19.9	0.065	13.534321	0.324	0.638	room temp.	
b7-127	c	246	810	1.9	5.5	35	5707	37.3	0.125	26.166112	0.299	0.66	room temp.	
b7-127	d	246	860	1.9	5.5	35		45.9	0.18	32.167514	0.292	0.664	room temp.	
b7-128	c	245	810	1.9	5.5	35	2215	26.4	0.121	47.625282	0.295	0.667	room temp.	
b7-128	d	245	860	1.9	5.5	35		36.6	0.207	66.180587	0.287	0.663	room temp.	
b7-129	c	245	810	0.275	5.5	5	6902	52.1	0.08	30.170965	0.319	0.647	room temp.	
b7-129	d	245	860	0.275	5.5	5		88.7	0.148	51.409736	0.313	0.652	room temp.	
b7-130	c	246	810	0.96	2.75	35	3447	25.3	0.119	29.411082	0.294	0.666	installed nichrome heaters	
b7-130	d	246	860	0.96	2.75	35		52.4	0.286	60.809399	0.274	0.689		
b7-131	c	246	810	0.96	2.75	35	3666	27.7	0.178	30.270049	0.302	0.666	repeat b7-119	
b7-131	d	246	860	0.96	2.75	35		54.8	0.313	59.79269	0.286	0.677		
b7-132	c	246	810	0.275	5.5	5	4943	9.59	0.035	7.7604694	0.317	0.643	installed MFC on O2 line	
b7-132	d	246	860	0.275	5.5	5		28.4	0.123	23.004248	0.318	0.641		
b7-133	c	245	810	1.49	5.5	27	3898	32.9	0.105	33.74038	0.328	0.634		
b7-133	d	245	860	1.49	5.5	27		52.1	0.169	53.422268	0.29	0.671		
b7-134	c	245	810	6.6	30	22	3667	50.3	0.145	54.919553	0.287	0.666		
b7-134	d	245	860	1.49	5.5	22		58.2	0.182	63.512408	0.281	0.68		
b7-135	c	245	810	5.25	15	35	3377	39	0.108	46.248149	0.298	0.654		
b7-135	d	245	860	5.25	15	35		56.9	0.186	67.343796	0.273	0.688		
b7-136	c	245	810	1.5	30	5	4022	43.8	0.154	43.600199	0.287	0.658		
b7-136	d	245	860	1.5	30	5		64	0.189	63.697166	0.309	0.659		
b7-137	c	246	810	6.6	30	22	3316	28.4	0.091	34.291315	0.284	0.681		
b7-137	d	246	860		30	22		43.5	0.17	52.469843	0.259	0.701		

b7-138	c	245	810	1.75	5	35	5540	61	0.131	44.018051	0.315	0.652	
b7-138	d	245	860	1.75	5	35		57.5	0.135	41.545126	0.3	0.665	
b7-138	d	245	650	1.75	5	35		20.9	0.039	15.084838	0.357	0.611	
	*												
b7-139	c	245	810	0.9	2.5	35	4373	31.2	0.104	28.509033	0.331	0.637	
b7-139	d	245	740	0.9	2.5	35		41.8	0.116	38.220901	0.302	0.662	
b7-140	c	245	810	0.9	2.5	35	4278	28.4	0.098	26.580178	0.336	0.632	repeat b7-139
b7-140	d	245	650	0.9	2.5	35		14.7	0.046	13.770453	0.361	0.6	
b7-141	c	245	810	6	30	20	4042	55.8	0.173	55.247402	0.277	0.685	similar to b7-134 for RTA profile
b7-141	d	245	860	6	30	20		53.4	0.117	52.874814	0.306	0.664	
b7-142	c	245	810	6	30	20	4141	46.6	0.133	44.993963	0.297	0.668	repeat b7-141 for RTA profile
b7-142	d	245	740	6	30	20		42.8	0.121	41.354745	0.291	0.672	
b7-143	c	245	810	6	30	20	4032	49	0.135	48.58879	0.286	0.678	repeat b7-141 for RTA profile
b7-143	d	245	700	6	30	20		20.6	0.055	20.386905	0.336	0.624	
b7-144	c	245	810	6	30	20	4133	50.3	0.14	48.727317	0.299	0.666	repeat b7-141 for RTA profile
b7-144	d	245	650	6	30	20		21.6	0.057	20.883136	0.349	0.61	
b7-145	c	245	810	6	30	20	4055	48.6	0.134	47.975339	0.295	0.662	repeat b7-141 for RTA profile
b7-145	d	245	600	6	30	20		1.1	0.006	1.0811344	0.526	0.445	
b7-146	c	245	810	6	30	20	8214	74	0.123	36.026297	0.308	0.656	thickness profile, 800nm
b7-146	d	245	810	6	30	20		66.8	0.11	32.52374	0.319	0.646	
b7-147	c	245	810	6	30	20	3991	53.4	0.149	53.550489	0.317	0.647	repeat to clean target
b7-147	d	245	810	6	30	20		52.1	0.144	52.177399	0.305	0.657	
b7-148	c	245	810	6	30	20	2106	20.2	0.12	38.380817	0.277	0.663	thickness profile, 200nm
b7-148	d	245	810	6	30	20		23.6	0.159	44.88604	0.303	0.651	
b7-149	c	245	810	6	30	20	6119	70.2	0.127	45.898023	0.316	0.642	thickness profile, 600nm
b7-149	d	245	810	6	30	20		74.7	0.133	48.808629	0.313	0.645	
b7-150	c	246	810	6	20	30	3361	27.4	0.115	32.609342	0.276	0.682	
b7-150	d	246	860	6	20	30		43.8	0.194	52.174948	0.287	0.673	
b7-151	c	246	810	6	30	20	4428	41.8	0.162	37.746161	0.319	0.644	std. conditions
b7-151	d	246	860	6	30	20		42.8	0.157	38.674345	0.314	0.646	
b7-152	c	246	-	6	30	20	1196	-	-	-	-	-	accident run

b7-152	d	246	-	6	30	20		-	-	-	-	-	
b7-153	c	246	810	6	30	20	2845	14.7	0.056	20.706503	0.319	0.636	low power (60W)
b7-153	d	246	810	6	30	20		13	0.054	18.29877	0.366	0.586	
b7-154	c	246	810	6	30	20	4935	17.5	0.077	14.158055	0.327	0.634	high power (140W)
b7-154	d	246	860	6	30	20		45.2	0.146	36.644377	0.306	0.659	
b7-155	c	246	810	1.5	30	5	3984	24.7	0.075	24.759036	0.307	0.654	low pressure (5mTorr)
b7-155	d	246	860	1.5	30	5		39	0.145	39.201807	0.287	0.673	
b7-156	c	246	810	6	30	20	3943	23.6	0.074	23.974131	0.326	0.635	High T (300 C)
b7-156	d	246	860	6	30	20		42.8	0.155	43.431397	0.315	0.646	
b7-157	c	246	810	6	30	20	3856	32.9	0.109	34.107884	0.316	0.645	Low T (150 C)
b7-157	d	246	860	6	30	20		58.9	0.215	61.109959	0.304	0.658	
b7-158	c	245	810	6	30	20	4435	62	0.138	55.912063	0.312	0.654	high power (120W)
b7-158	d	245	860	6	30	20		74	0.194	66.723788	0.3	0.664	
b7-159	c	245	810	6	30	20	2956	32.9	0.121	44.492558	0.292	0.657	low power (50W)
b7-159	d	245	860	6	30	20		44.2	0.167	59.786874	0.287	0.663	
b7-160	c	245	810	6	30	20	4264	56.9	0.154	53.334897	0.293	0.672	High T (300 C)
b7-160	d	245	860	6	30	20		61.7	0.16	57.833021	0.301	0.661	
b7-161	c	245	810	6	30	20	4125	47.6	0.113	46.164848	0.313	0.655	Low T (150 C)
b7-161	d	245	860	6	30	20		61	0.144	59.117576	0.298	0.665	
b7-162	c	245	810	6	30	20	4499	48.3	0.101	42.936208	0.317	0.646	low pressure (5 mTorr)
b7-162.	d	245	860	6	30	20		59.3	0.132	52.680596	0.309	0.655	
b7-163	c	245	**	6	30	20	4365			0			**air,700C,5hrs
b7-163	d	245	**	6	30	20				0			**810 RTA with SiON top

BIOGRAPHICAL SKETCH

John South Lewis III (Jay) was born in Huntsville, Alabama on July 1, 1973. He lived in Houston, Texas from 1974 until his family moved back to Huntsville in 1984. He graduated from Huntsville High School in 1991 as a National Merit Scholar.

He attended the Georgia Insitute of Technology beginning in September 1991 and graduated in June 1996 with a bachelors degree, highest honors, in Materials Science and Engineering. He was awarded his Master of Science degree from the Department of Materials Science and Engineering at the University of Florida in 1998.

From 1992-1995 he worked at the Georgia Tech Research Institute as a co-op student and from 1995-1996 as a part-time research assistant, primarily studying chemical vapor deposition of refractory thin films. He has worked as a summer intern for General Motors in Norcoross, GA in 1995, Planar Systems, Inc. in Beaverton, OR, in 1997, and for HP Labs in Palo Alto, CA in 1999.

He received his Ph.D. from the Department of Materials Science and Engineering at the University of Florida under the advisement of Dr. Paul H. Holloway. His areas of research included phosphors for electroluminescent and cathodoluminescent flat panel displays as well as luminescence of rare-earth and transition metal ions. His areas of interest also include photonics and MEMS.

Mr. Lewis was awarded the Chapman-Pentecost Scholarship in 1995, as well as the ASM Undergraduate Scholarship in both 1994 and 1995. In 1997 he was awarded a National Defense Science and Engineering Graduate Fellowship, and in 1998 he was awarded the Russell and Varian Sigurd Fellowship from the American Vacuum Society.

He has co-authored 8 refereed articles in the areas of luminescence, phosphors, chemical vapor deposition, and chemical vapor infiltration.

I certify that I have read this study and that in my opinion it conforms to acceptable standards of scholarly presentation and that it is fully adequate, in scope and quality, as a dissertation for the degree of Doctor of Philosophy.

Paul H. Holloway, Chairman
Ellis D. Verink Professor and
Distinguished Professor of Materials
Science and Engineering

I certify that I have read this study and that in my opinion it conforms to acceptable standards of scholarly presentation and that it is fully adequate, in scope and quality, as a dissertation for the degree of Doctor of Philosophy.

Cammy R. Abernathy
Professor of Materials Science and
Engineering

I certify that I have read this study and that in my opinion it conforms to acceptable standards of scholarly presentation and that it is fully adequate, in scope and quality, as a dissertation for the degree of Doctor of Philosophy.

Kevin S. Jones
Professor of Materials Science and
Engineering

I certify that I have read this study and that in my opinion it conforms to acceptable standards of scholarly presentation and that it is fully adequate, in scope and quality, as a dissertation for the degree of Doctor of Philosophy.

Rajiv K. Singh
Professor of Materials Science and
Engineering

I certify that I have read this study and that in my opinion it conforms to acceptable standards of scholarly presentation and that it is fully adequate, in scope and quality, as a dissertation for the degree of Doctor of Philosophy.

Fan Ren

Fan Ren
Professor of Chemical Engineering

This dissertation was submitted to the Graduate Faculty of the College of Engineering and to the Graduate School and was accepted as partial fulfillment of the requirements for the degree of Doctor of Philosophy.

December 2000

M. J. Ohanian
Dean, College of Engineering

Winfred M. Phillips
Dean, Graduate School